Daniel Adams
Terry L. Alford
James W. Mayer

Engineering Materials and Processes

Silver Metallization

Stability and Reliability

Springer

Engineering Materials and Processes

Series Editor

Professor Brian Derby, Professor of Materials Science
Manchester Materials Science Centre, Grosvenor Street, Manchester, M1 7HS, UK

Other titles published in this series

Fusion Bonding of Polymer Composites
C. Ageorges and L. Ye

Composite Materials
D.D.L. Chung

Titanium
G. Lütjering and J.C. Williams

Corrosion of Metals
H. Kaesche

Corrosion and Protection
E. Bardal

Intelligent Macromolecules for Smart Devices
L. Dai

Microstructure of Steels and Cast Irons
M. Durand-Charre

Phase Diagrams and Heterogeneous Equilibria
B. Predel, M. Hoch and M. Pool

Computational Mechanics of Composite Materials
M. Kamiński

Gallium Nitride Processing for Electronics, Sensors and Spintronics
S.J. Pearton, C.R. Abernathy and F. Ren

Materials for Information Technology
E. Zschech, C. Whelan and T. Mikolajick

Fuel Cell Technology
N. Sammes

Casting: An Analytical Approach
A. Reikher and M.R. Barkhudarov

Computational Quantum Mechanics for Materials Engineers
L. Vitos

Modelling of Powder Die Compaction
P.R. Brewin, O. Coube, P. Doremus and J.H. Tweed

Daniel Adams • Terry L. Alford
and James W. Mayer

Silver Metallization

Stability and Reliability

Springer

Daniel Adams, PhD
Department of Physics
University of the Western Cape
7535 Bellville
South Africa

Terry L. Alford, PhD
School of Materials Science
Arizona State University
Tempe, Arizona 85287-6006
USA

James W. Mayer, PhD
School of Materials Science
Arizona State University
Tempe, Arizona 85287-6006
USA

ISBN 978-1-84800-026-1 e-ISBN 978-1-84800-027-8

Engineering Materials and Processes ISSN 1619-0181

British Library Cataloguing in Publication Data
Adams, Daniel
Silver metallization : stability and reliability. -
(Engineering materials and processes)
1. Silver - Electrometallurgy 2. Electrochemical
metallizing 3. Integrated circuits - Materials
I. Title II. Alford, Terry L. III. Mayer, James W., 1930-
669.2'3
ISBN-13: 9781848000261

Library of Congress Control Number: 2007932625

Printed on acid-free paper

9 8 7 6 5 4 3 2 1

springer.com

Dedicated to our ever patient,
supportive and loving wives,

Madeline, Katherine and Betty

Preface

Silver (Ag) is considered as a future interconnect material for ultra large scale integrated (ULSI) circuit technology, because of its low resistivity (1.6 μΩ-cm), a value lower than that of aluminum (Al) or copper (Cu), the current choices for ULSI metallization. The drawbacks of Ag in terms of agglomeration, adhesion and corrosion are overcome by the use of encapsulation layers or addition of a few percent of alloying elements (such as Al and Ti). For example, silver with a 5% Al meets all the morphology and stability requirements for a fully processed interconnect. The advantage of silver metallization is that the complicated chemical mechanical polishing (CMP) process is not required whereas it is a crucial step in copper-based metallization.

The aim of this monograph is to provide current and up-to-date knowledge on silver metallization and its potential as a favorable candidate for implementation as a future interconnect material for integrated circuit technology. A special feature of the monograph is the presentation of novel approaches to overcome the thermal and electrical stability issues associated with silver metallization. Given the fact that silver is just now considered for manufacturing, the main benefit of the text is that it provides a valuable resource in this emerging field.

It introduces the academic community and industrial users to the subjects of preparation and characterization of elemental silver thin films and silver-metal alloys (Chapter 2); formation of diffusion barriers and adhesion promoters (Chapter 3); evaluation of the thermal stability of silver under different annealing conditions (Chapter 4); evaluation of the electrical properties of silver thin films under various processing conditions (Chapters 3 and 4); silver electromigration resistance (Chapter 5) and the integration of silver with low-k dielectric materials (Chapter 6). The monograph will be very useful to senior undergraduate and postgraduate students, scientists, engineers, and technologists in the field of integrated circuits and microelectronics research and development.

The content of the monograph is an indirect result of extensive and in-depth research and contributions by graduate students from both the Department of Physics, University of the Western Cape (UWC), Bellville, South Africa (Gerald Malgas and Basil Julies) and School of Materials Science, Arizona State University (ASU), Tempe, USA (Yu Wang, Peter Zeng, Hunckul Kim, Li Zhou,

Phucanh Nguyen, Esra Misra, Martin Mittan and Kastub Gadre). The authors acknowledge with gratitude the contributions by all these students. A special word of thanks and appreciation goes to Gerald Malgas (my first PhD student at UWC) for his assistance with the figures and drawings.

Daniel Adams
University of the Western Cape, Bellville, South Africa

Terry L. Alford
Arizona State University, Tempe, Arizona, USA

James W. Mayer
Arizona State University, Tempe, Arizona, USA

Contents

1

Introduction

1.1 Silver Metallization

As the complexity of multilayer metallization (MLM) increase, the performance limiting resistive and capacitive signal delays increase accordingly. The development of advanced ultra large scale integration (ULSI) and gigascale integration (GSI) technologies will place stringent demands on future interconnect and metallization schemes [1]. To decrease the resistance–capacitance (RC) signal delays, the circuit can be fabricated with a metal having resistivity lower than the currently used Al(Cu) alloy [2]. As a result, higher current densities can be imposed on the metal lines and faster switching speeds can be achieved, due to the lower RC time delay [3].

Silver has the lowest resistivity of all metals, and its high oxidation resistance differentiates it from aluminum and copper. On the issue of electromigration, silver promises to provide an electromigration resistance of at least one order of magnitude better than Al [4]. It has been shown that Cr and TiO_2 overcoatings of silver greatly enhance the electromigration resistance of Ag [4, 5]. These properties of Ag make it one of the promising high-conductivity candidates to be considered as possible interconnect material for ULSI technology. However, before it can be used for this purpose, there are several issues that need to be addressed in realizing Ag interconnects.

Silver does not reduce SiO_2 and is therefore expected not to adhere well to SiO_2 surfaces [6]. It suffers also from electrolytic migration along surfaces in wet atmospheric environments [4] and silver has a high diffusivity in SiO_2 [7].

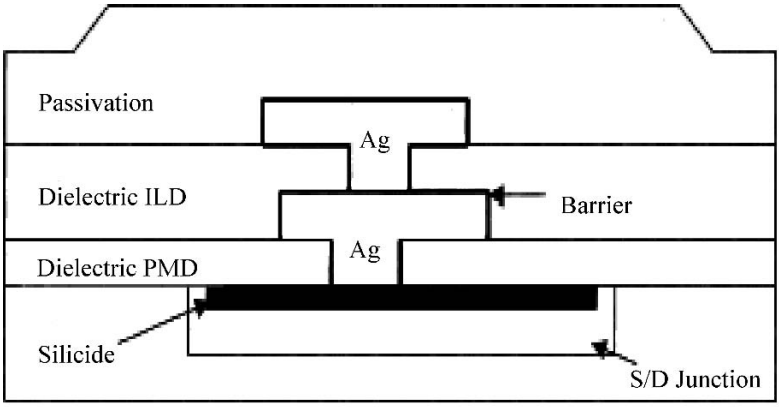

Figure 1.1. Cross-sectional diagram of a two metal level interconnect structure, using Ag as the conductor [4]

A major concern regarding Ag metallization is its susceptibility to corrosion in the presence of weak oxidizing agents such as sulfur [8]. The corrosion and agglomeration of Ag in high Cl ambients have also been reported [6, 8]. Therefore, implementation of silver as interconnect material will require adhesion promoters to improve the adhesion to dielectrics; passivation layers to protect it against corrosive environments, and the development of a process to define the interconnection wiring.

Figure 1.1 is a cross-section of a three metal level interconnect structure using Ag as the conductive material. The interlevel dielectrics (ILD) could be conventional SiO_2-based materials or more ideally, materials such as Pa-*n* (or polyimide). If conventional SiO_2 is used, then Ag plugs and interconnects have to be enclosed in diffusion/drift barriers so that Ag will not move into Si or SiO_2 under thermal stress or biased temperature stress (BTS).

As devices continue to shrink, both film thickness and widths of metal interconnects are also reduced; hence, the effect of thermal stability becomes more significant because it affects the device reliability.

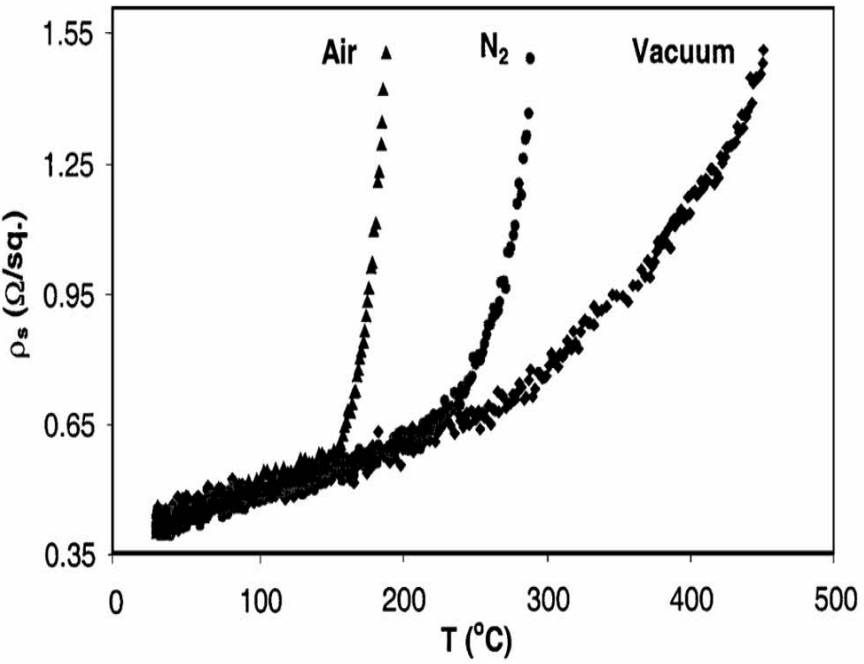

Figure 1.2. *In situ* sheet resistance as function of temperatures for Ag(60 nm)/SiO_2 annealed at 0.15 °C/s in air, N_2 and vacuum [13]

Ag films have been reported to agglomerate at moderate temperatures under oxygen containing ambient [9–12]. It has also been reported that the degree of agglomeration depends specifically on test conditions, for example, ambient and film thickness [9–12]. Agglomeration is the result of atoms and voids diffusion causing a surface restructuring during annealing. As the film morphology evolves voids and hillocks are formed. Changes in sheet resistance of the films can be used as a measure of formation and growth of voids and hillocks [13].

Figure 1.2 shows the *in situ* sheet resistance of Ag(60 nm)/SiO_2, annealed in air, N_2 and vacuum ambient at 0.15 °C/s ramp [13]. It is evident that the annealing ambient significantly affects film stability. The sample annealed in air seems to be more susceptible to thermal instability and hence a rapid change in sheet resistance occurs. Samples annealed in vacuum appear to be the most thermally stable and a more gradual change in sheet resistance occurs once it deviates from linearity. The scanning electron microscope (SEM) micrograph in Figure 1.3 depicts the surface morphology of a 75 nm thick Ag layer on SiO_2 annealed at a ramp rate of 0.6 °C/s at 450 °C in air [13]. As seen from the micrograph, the film consists of a uniformly distributed connected network of islands.

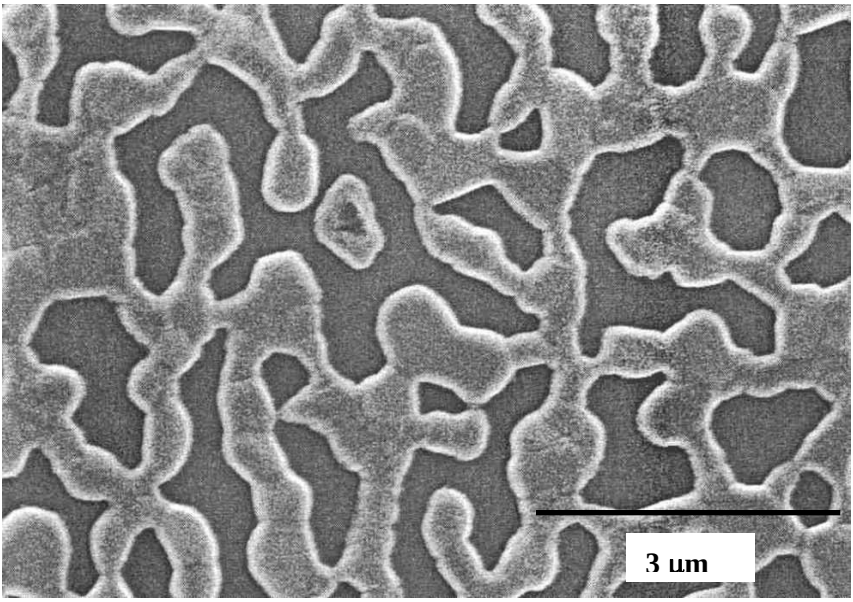

Figure 1.3. SEM micrograph of Ag/SiO_2 annealed at a ramp rate of 0.60°C/s at 450°C in air [13]

Apart from the thermal stability issues that dictate the potential application of silver metallization in future integrated circuits, a pattern transfer technology is needed to enable the integration of Ag into conventional semiconductor fabrication operations. This necessitates that the processes be compatible with the current equipment and processes in modern integrated circuit (IC) fabrication facilities. Halogen admixtures with oxygen, and oxygen glow discharges have shown potential as reactive species to pattern silver [2–4].

Unlike copper metallization, Ag thin films can be reactive ion etched at reasonable rates using a CF_4 plasma. This etch technology is an atypical 'dry-etch' process since the formation of volatile products is not the main removal mechanism. The primary film removal mechanism, however, is the subsequent resist strip process. The silver etch process using a CF_4 plasma depends strongly on the reactive neutrals and the removal rate is enhanced significantly by the presence of energetic ions as well. The CF_4-based patterning technique is unique because it utilizes a plasma process and a wet chemical clean to obtain anisotropically etched lines [14, 15]. With the ability to pattern silver using this technique, the post etch corrosion, removal rates, and resist erosion issues are improved. This is a very important step toward the integration of Ag metallization into interconnect technology.

1.2 Properties of Silver, Copper and Aluminum

A comparison of the electrical, physical, mechanical, and thermal properties of silver, copper, and aluminum is given in Table 1.1.

Table 1.1. Comparison of properties of Ag with Cu and Al

Properties	Ag	Cu	Al
Bulk resistivity (μΩ-cm) at 20°C	1.59	1.68	2.65
Thin film resistivity (μΩ-cm) at 20°C	2.0 (Ag/Ti)	2.0–2.5 (Cu/Cr) 2.8 (Cu/Ni)	3.3 (Al-Cu)
Diffusivity in Si (cm^2/sec)	$2.3\times10^{-3}\, e^{-1.6/kT}$	$4.2\times10^{-2}\, e^{-1.0/kT}$	–
Self-diffusivity (cm^2/sec)	$0.67e^{-1.97/kT}$	$0.78\, e^{-2.19/kT}$	$1.71\, e^{-1.48/kT}$
Electromigration activation energy (eV)	0.95 (225–285°C)	1.1 (250–395°C)	0.4–0.8
Young's modulus ($\times10^{11}$ dyn cm^{-2})	8.27	12.98	7.06
TCR$\times10^3$ (K^{-1})	4.1	4.3	4.0
Mean free path of e^- (nm)	52.0	39.0	15.0
Melting point (°C)	961	1083	917
Thermal conductivity ($Wcm^{-1}\, K^{-1}$)	4.25	3.98	2.38

1.3 References

[1] J. M. E. Harper, K. L. Holloway, T. Y. Kwok, US Patent No. 5,130,274 (1992).
[2] The National Technology Roadmap for Semiconductors, Semiconductor Industry Association, San Jose, CA, 1994.
[3] J. Li, J. W. Mayer, Y. Shacham-Diamand, E. G. Colgan, Appl. Phys. Lett. 60. 2983(1992).
[4] D. Adams, and T. L. Alford, Materials Science and Engineering: Reports 40, 207(2003).
[5] T. Iijima, H. Ono, N. Ninomiya, Y. Ushiku, T. Hatanaka, A. Nishiyama, H. Iwai, Extended Abstracts of the 1993 International Conference on Solid State Devices and Materials, Makuhari, 183(1993).
[6] S. P. Murarka, R. J. Guttman, A. E. Kaloyeros, W. A. Lanford, Thin Solid Films 236, 257(1993).
[7] J. D. McBrayer, R. M. Swanson, T. W. Sigmon, J. Electrochem. Soc. 133 1243(1986).
[8] T. E. Graedel, J. Electrochem. Soc. 139(7), 1963(1992).
[9] B. Chalmers, R. King, R. Shuttleworth, Proc. R. Soc. A 193, 465(1948).
[10] A. E. B. Presland, G. L. Price, D. L. Trimm, Prog. Surf. Sci. 3, 63(1973).
[11] S. K. Sharma, J. Spitz, Thin Solid Films 65, 339(1980).
[12] K. Sharma, J. Spitz, Thin Solid Films 66, 51(1980).
[13] P. N. Nguyen, Ph.D. thesis, Arizona State University, 2000.
[14] P. N. Nguyen, Y. Zeng, T. L. Alford, J. Vac. Sci. Technol. B 17(5), 2204(1999).
[15] T. L. Alford, P. N. Nguyen, Y. Zeng, J. W. Mayer, Microelectronics Engineering 55, 383(2001).

2

Silver Thin Film Characterization

2.1 Introduction

Thin films of Ag layered structures, typically less than a micron in thickness, are tailored to achieve desired functional properties. Typical characterization is the instrumentations that use X-ray and ion beams to probe the properties of the film. This work discusses two techniques in thin film analysis, Rutherford backscattering spectrometry (RBS) [1, 2] and X-ray diffractrometry (XRD) [3, 4] which emphasize composition and lattice measurements, respectively. Advancement in RBS and X-ray analyses are developed in response to the needs of the microelectronics and forensic disciplines.

Analysis of metallization on SiO_2 is typically done with Rutherford backscattering at 2.0 MeV energies and with semiconductor nuclear particle detectors. The resonance analysis of these species is done in the same experimental chamber as used in RBS, but the energy of the incident helium ions is increased to energies where there are resonances in the backscattering cross sections [5, 6]. These resonances increase the yield of the scattered particle by nearly two orders of magnitude and provide high sensitivity to the analysis of oxygen and carbon in silicon. The use of these high energies, 3.05 and 3.7 MeV for the helium-oxygen and helium-nitrogen resonances respectively is called resonance scattering or non-Rutherford scattering.

In a similar manner XRD is also considered as a nondestructive characterization technique. XRD is used to monitor the phases and structure present in the film. Also the lattice parameter, strain and texturing can be resolved using pole figure analysis [3, 4].

2.2 Rutherford Backscattering Spectrometry

In a typical scattering chamber, the sample is located such that the beam position does not shift across the sample as the sample is tilted with respect to the incident ion beam. The backscattering detector is mounted as close to the incident beam as possible such that the average backscattering angle, ϑ, is close to 180°, typically 170°, with a detector solid angle of 5 millisteradians (msr). The vacuum requirements in the target chamber are comparable to those in the accelerator beam lines. Enhanced vacuum levels reduce the probability that the ion beam will lose energy along its path to the sample and also minimizes deposition of contaminants and hydrocarbons on the surface during analysis.

In traditional backscattering spectrometry using helium ions, the energy resolution of the solid-state particle detector is typically >17 keV. The output signal, which is typically millivolts in pulse height is processed by silicon integrated circuit electronics and provides an energy spectrum in terms of number of particles versus energy. A multichannel analyzer records the number of backscattered particles versus a given energy in a specific channel.

2.2.1 Scattering Kinematics

During ion-beam analysis the incident particle penetrates into the target and undergoes inelastic collisions with the electrons in the samples and loses energy as it penetrates. During the penetration of the helium ions a small fraction undergo elastic collisions with the target atom, which defines the backscattering signal. Figure 2.1 shows a schematic representation of the geometry of an elastic collision between a projectile of mass M_1 and energy E_o with a target atom of mass M_2 initially at rest. After collision the incident ion is scattered back through an angle ϑ and emerges from the sample with an energy E_1. The target atom after collision has a recoil energy E_2. There is no change in target mass, because nuclear reactions are not involved and energies are non-relativistic. The ratio of the projectile energies for $M_1 < M_2$ is given by:

$$K = \frac{E_1}{E_o} = \left[\frac{(M_2^2 - M_1^2 \sin^2 \vartheta)^{\frac{1}{2}} + M_1 \cos \vartheta}{M_2 + M_1} \right]^2 \tag{2.1}$$

The energy ratio $K = E_1/E_o$, called the *kinematic factor*, shows how the energy of the backscattered particle is a function of the incident particle and target atoms masses, the scattering angle, and incident energy.

The ability to identify different mass species depends on the energy resolution of the detector which is typically 17 keV full width at half maximum (FWHM). For example, Ag has a mass M_2 = 108 and In has a mass M_2 = 115. The difference between K_{Ag} = 0.862 and K_{In} = 0.870 is 0.008. For 2.8 MeV helium ions, the difference in backscattering energy is 22 keV which is larger than the detector-system resolution, indicating that signals from Ag and In on the surface can be resolved.

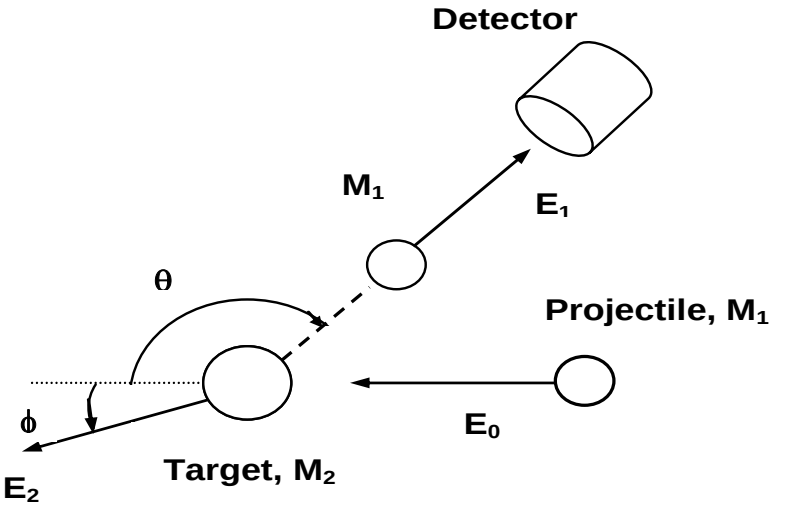

Figure 2.1. A schematic representation of an elastic collision between a particle of mass M_1 and initial energy E_0 and a target atom of mass M_2. After the collision the projectile and target atoms have energies of E_1 and E_2, respectively.

2.2.2 Scattering Cross Section

The identity of target elements is established by the energy of the scattered particles after an elastic collision. This is done by measuring the yield *Y*, the number of backscattered particles for a given value of incident particles *Q*. The detector's solid angle is given as Ω. The areal density, the number of atoms per unit area, N_S is determined from the scattering cross section σ (ϑ) by:

$$N_s = \frac{Y}{\sigma(\vartheta) Q d\Omega} \tag{2.2}$$

For a narrow beam of fast particles impinging upon a thin uniform target that is wider than the beam and at an tilt angle ϑ, the simplest approximation for the scattering cross section is given by:

$$\sigma(\vartheta) = \left(\frac{Z_1 Z_2 e^2}{4E} \right)^2 . \frac{1}{\sin^4 \frac{\vartheta}{2}} \tag{2.3}$$

which is the scattering cross section originally derived by Rutherford. For 2 MeV helium ions incident on silver, Z_2 = 47 at an angle of 180º, the cross section is 2.9×10^{-24} cm^2 or 2.9 barns (where the barn = 10^{-24}cm^2). The distance of closest

approach is about 7×10^{-3} nm which is smaller than the *K*-shell radius of silver (10^{-1} nm).

2.2.3 Depth Scale

Light ions such as helium lose energy through inelastic collision with atomic electrons. In backscattering spectrometry, where the elastic collision takes place at depth *t* below the surface, one considers the energy loss along the inward path and on the outward path as shown in Figure 2.2. The energy loss on the way in is weighted by the kinematic factor and the total is given by the relationship:

$$\Delta E = \Delta t\left(K\frac{dE}{dx}\bigg|_{in} + \frac{1}{|\cos\vartheta|}\cdot\frac{dE}{dx}\bigg|_{out}\right) = \Delta t[S] \tag{2.4}$$

where d*E*/dx is the rate of energy loss with distance and [*S*] is the energy loss factor. The particle loses energy ΔE_{in} via inelastic collisions with electrons along the inward path. There is energy loss ΔE_s in the elastic scattering process at depth *t*. There is energy loss due to inelastic collisions ΔE_{out} along the outward path.

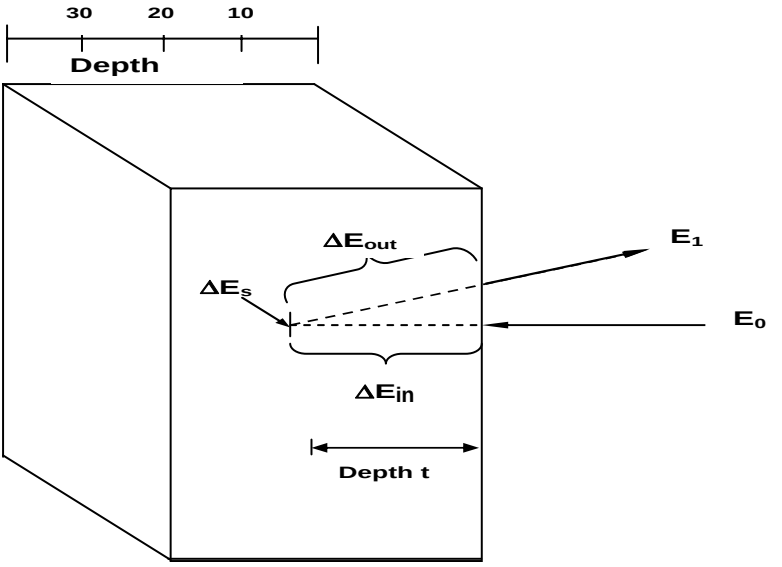

Figure 2.2. Energy loss components for a projectile that scatters from depth t. The particle loses energy ΔE_{in} via inelastic collisions with electrons along the inward path. There is energy loss ΔE_s in the elastic scattering process at depth *t*. There is energy lost to inelastic collisions ΔE_{out} along the outward path.

An example illustrating the influence of depth on analysis is given in Figure 2.3, which shows two thin silver layers on the front and back of a titanium film. The scattering from silver at the surface is clearly separated from Ag at the back layer. The energy width between the Ag signals is closely equal to that of the energy width of the Ti signal. The depth scales are determined from energy loss values.

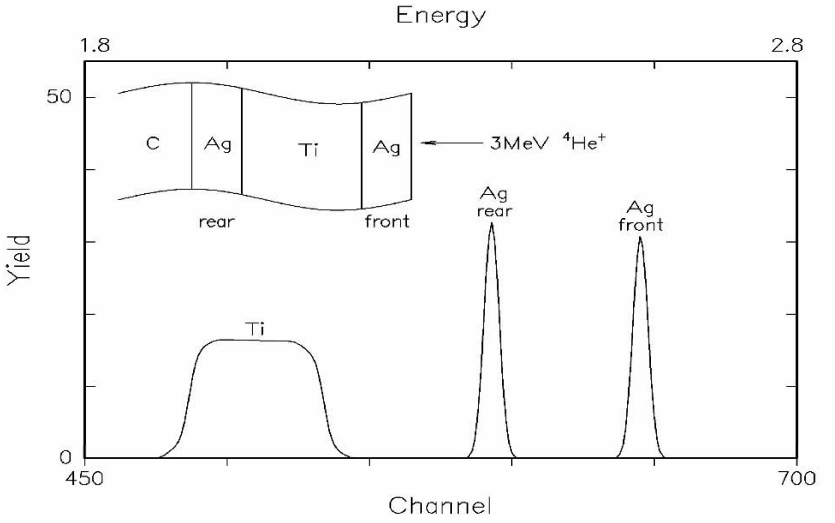

Figure 2.3. Backscattering spectrum of a Ti film (150 nm) with thin layers of Ag (3 nm) on the front and back surfaces of the titanium

2.2.4 Ion Resonances

At energies of a few MeV nuclear reactions and strong deviations from Rutherford scattering can result in a strong increase (resonance) in the scattering cross section (for example at 3.04 MeV for ^{4}He ions incident on ^{16}O). This reaction can be used to increase the sensitivity for the detection of oxygen as well as other light elements such as carbon and nitrogen. In order to evaluate the amount of oxygen in Ag diffusion barriers (*e.g.*, $TiAl_xN_yO_z$) on SiO_2/Si substrate, the oxygen resonance technique using 3.05 MeV $^{4}He^{+2}$ ion beam was employed (Figure 2.4). The RUMP simulation [7] overlaps the collected spectrum. The enhanced oxygen peak near channel 200 is a direct consequence of O resonance at 3.05 MeV and corresponds to oxygen atoms present in the thin film.

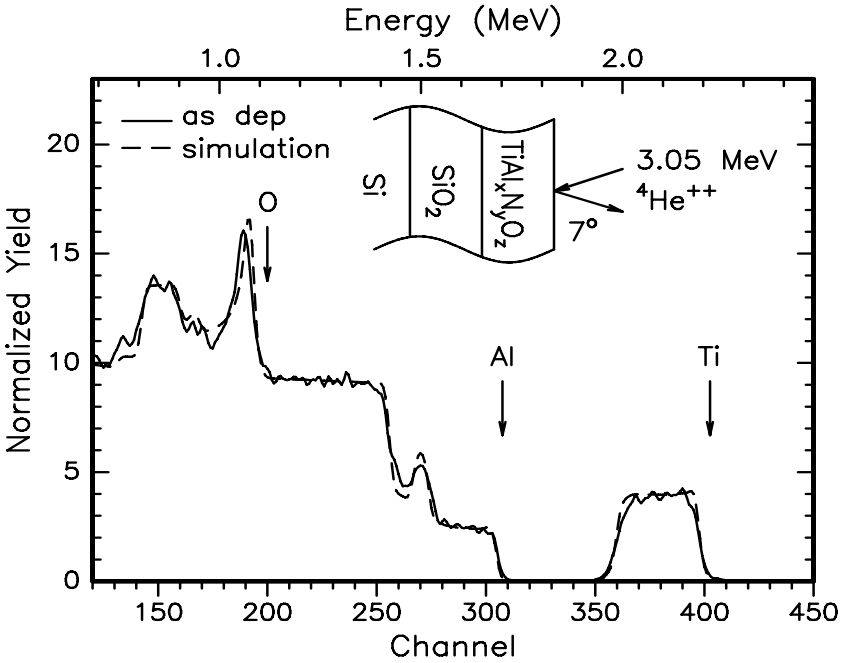

Figure 2.4. RBS spectrum (3.05 MeV He^{+2}, 7° tilt) and simulation of as-deposited $TiAl_xN_yO_z$ thin film on SiO_2/Si substrate

2.3 X-ray Diffractometry

W. L. Bragg derived a description of coherent scattering from an array of periodic scattering sites, *i.e.*, atoms in a crystalline solid. The scalar description of diffraction considers the case of monochromatic radiation impinging on two sheets of atoms in the crystal spaced d_{hkl} between reflecting planes. The wavelength λ of the radiation is smaller than the interatomic spacing d_{hkl} of the specific (*hkl*) planes.

Bragg invoked the Law of Reflectivity (or Reflections) that states that the scattering incident angle and exiting angle must be equal, $\vartheta_{in} = \vartheta_{out}$ under the condition of coherent scattering. The wavelets scattered by the atoms combine to produce constructive interference if the total path difference 2*ΔP for the reflected waves equals integer (*n*) multiples of λ:

$$n\lambda = 2\Delta P = 2d_{hkl} \sin\vartheta \tag{2.5}$$

Hence, Bragg's Law: $n\lambda = 2d_{hkl} \sin\vartheta$ defines the condition for diffraction. The simplest of all modern X-ray analyses is powder analysis using an X-ray diffractometer. The technique can be used to characterize polycrystalline thin films

as well. The sample under investigation is placed on the sample stage of the diffractometer. The key components of a typical diffractometer include a sample stage, monochromatic radiation source, and radiation electronic solid-state detection system. The scattered X-rays dissipate energy by generation of electron-hole pairs in the detector. The electronic system converts the collected charge into voltage pulses which are directly proportional to the intensity of the diffracted X-ray beam. The typical X-ray spectrum is a plot of intensity verses angle, *e.g.*, 2ϑ. The phase can be indentified by comparing the spectrum to Joint Committee on Powder Diffraction Standards (JCPDS) cards. Figure 2.5 shows an typically XRD spectrum from a 200 nm thick, polycrystalline Ag layer on a single crystalline Si substrate.

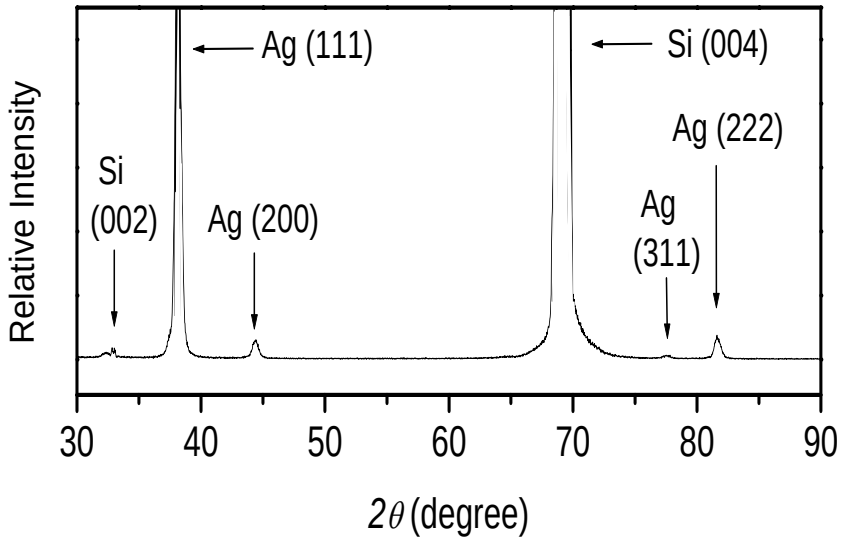

Figure 2.5. XRD spectrum of a 200 nm polycrystalline Ag layer on a single crystalline Si substrate. The indexed peaks correspond to specific reflections. The forbidden Si(002) reflection is due the double difraction of the strong (004) reflection.

2.4 References

[1] W. K. Chu, J. W. Mayer, and M. A. Nicolet, Backscattering Spectrometry, Academic Press, New York, 1978.

[2] J. W. Mayer, E. Rimini, Ion Handbook for Material Analysis, Academic Press, New York, 1977.

[3] B. D. Cullity and S. R. Stock, Elements of X-ray Diffraction, Prentice Hall, NJ, 2001.

[4] T. L. Alford, Feldman, L. C.; J. W. Mayer, Fundamentals of Nanoscale Analysis, Springer, New York, 2007.

[5] S. W. De Coster, B. Brijs, J. Goemans, and W. Vandervost, Nucl. Instr. Meth. B 66**,** 128318(1992).
[6] S. W. Russell, T. E. Levine, A. E. Bair, and T. L. Alford, Nucl. Instr. Meth. B 118**,** 118(1996).
[7] L. R. Doolittle, Nucl. Instr. Meth. B 15, 227(1986).

3

Diffusion Barriers and Self-encapsulation

3.1 Introduction

As feature sizes in multilevel metallization continue to shrink, the thermal stability of metallization and barrier layers become more critical for device reliability. The application of silver in multilevel metallization schemes require thermal stability when in contact with other metal layers and dielectrics. Therefore, developing a suitable diffusion barrier to retard the diffusion of Ag into adjacent materials and to prevent agglomeration is indispensable for the Ag metallization scheme. There have been extensive efforts to investigate qualified diffusion barrier layers interposed between Ag and SiO_2 [1]. The stability of silver thin films on various underlying layers at elevated temperatures has also been investigated [1]. Several authors have investigated the behavior of Ag on SiO_2/Si substrates [2, 3]. The addition of a thin Au layer between the Ag and Si was found to improve the stability of the interface by forming an intermixed region, resulting in a lowering of the interfacial energy of the Ag/Si system [3].

Refractory metal nitrides such as TiN, TaN, and WN are widely recognized as attractive materials for use as diffusion barriers in metal-semiconductor contacts due to their high stability and good conductivity [4]. TaN has been studied as a diffusion barrier for copper metallization since it is thermodynamically stable with Cu and due to the absence of any compound formation between Cu and Ta, and between Cu and N [5].

Diffusion barriers are used to prevent degradation of devices as a result of poor adhesion and interdiffusion. The objective is to find an intermediate layer between the interconnect Ag metal and the underlying dielectric that will act as both an

adhesion promoter and an effective diffusion barrier between interconnect metal and adjacent materials.

3.2 Titanium-Nitride Self-encapsulation of Silver Films

3.2.1 Introduction

The existing metallization schemes for ohmic contacts, gate metal and interconnections are found to be inadequate for the development of ultra large scale integration (ULSI) and gigascale integration (GSI). These inadequacies include the reliability of aluminum and its alloys as current carriers, susceptibility to electromigration and the relatively high resistivity of Al (~2.7 μΩ-cm). For the development of faster devices, the resistance-capacitance (RC) delay must be reduced. Advanced metallization schemes using so-called multilevel metallization (MLM) structures of a low resistivity metal such as Cu have been proposed to reduce the resistance component of the RC delays [6].

Currently copper and silver, noted for low resistivities and higher resistance to electromigration, are being investigated as future interconnect materials [7, 8]. Despite this they have not found extensive application in ICs because of their (a) high diffusivity and deep levels in silicon, (b) poor adhesion to SiO_2 and polyimide, and (c) reactivity with the environment. To make copper and silver metallization manufacturable, adhesion promoters, protection against corrosive environments and the development of a process to define interconnection wiring will be needed.

The three most commonly used techniques to enhance the adhesion between the dielectric and silver are: (i) the use of adhesion promoters; (ii) increased temperature of deposition or providing energy to ionize depositing species; (iii) surface pretreatment, especially plasma oxidation of polymers, sputter damage of metal surfaces or use of ion implantation near the polymer or metal surface. The use of adhesion promoters seems attractive since they can also act as diffusion barriers at higher process temperatures. Titanium, TiW and TiN have been most frequently used because of titanium's excellent chemical reactivity with oxygen, carbon, nitrogen, and fluorine.

3.2.2 Experimental Details

Alloy films consisting of ~200 nm Cu (27 at.% Ti), and Ag(6–26 at.% Ti) were co-deposited by electron-beam evaporation onto thermally grown SiO_2 (100–200 nm) on (100) Si substrates. The stoichiometry and thicknesses of all the as-deposited samples were determined by Rutherford backscattering spectrometry (RBS). Samples were annealed for 10–120 minutes at temperatures ranging from 300 to 700°C in a Lindberg single-zone quartz-tube furnace in a flowing electronic grade (99.99%, with $H_2O < 33$ and $O_2 + Ar < 10$ molar ppm) ammonia (NH_3) ambient at atmospheric pressure, to form the refractory metal nitrides. Before each anneal the annealing chamber was evacuated to about 10 mTorr followed by a 2.5 minute purge with NH_3. This sequence was repeated twice with a final 20 minute purge. To minimize the chances of oxidation, flow rates of ~2–8 l/min were maintained during the annealing. Free surface as well as interfacial reactions was analyzed by RBS and Auger electron spectroscopy (AES). The RBS analysis was performed using 1.7 MV Tandem Accelerator with He^{+2} beam energies between 2.0 and 4.3 MeV. The backscattering angle was 170° and the total accumulated charge was 10–20 μC. The samples were tilted at 7°. We utilized the computer simulation program RUMP for simulation and interpretation of RBS spectra.

After annealing, the sheet resistance of certain samples was measured by the four-point-probe method. The resistivity was determined from the sheet resistance and thickness of dealloyed Cu or Ag film only. Here, the measured resistivity was considered to be that of the metal layers. The contribution of the surface Ti-oxynitride layer resistivity to the total resistivity was less than 1%, because the ratio of the nitride thickness to Ag or Cu thickness was approximately 1:10.

3.2.3 Results

All anneals in this section were performed for 30 minutes in a flowing NH_3 ambient. Figure 3.1 compares the RBS spectrum of the as-deposited Ag(19 at.% Ti) alloy with that nitrided at 450°C and 600°C. After a 450°C anneal, the presence of a “Surface Ti” peak and a distinct “Interfacial Ti” peak indicates that Ti segregated to the free surface and also reacted with the SiO_2 substrate.

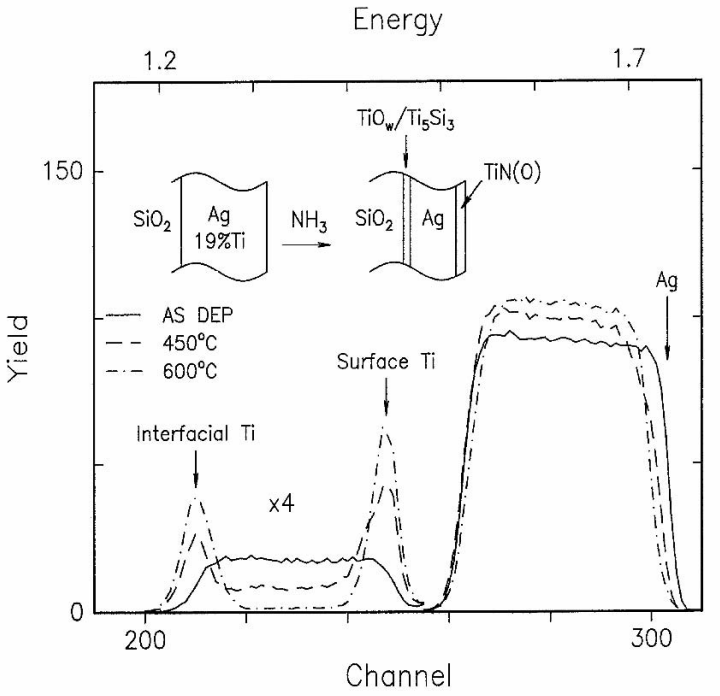

Figure 3.1. RBS spectra showing the depth distributions of Ag and Ti of a 210 nm-thick Ag(19 at.% Ti) alloy, before and after annealing at 450°C and 600°C for 30 minutes in NH_3. A 2.0 MeV He^{+2} beam energy was used [9].

The surface and interfacial reactions result in the formation of a TiN(O) layer and Ti-oxide/Ti-silicide bilayer structure, respectively. Computer RUMP simulation of the spectrum corresponding to the 450°C anneal, suggests that the dealloyed Ag layer contains a residual Ti concentration of ~10.8 at.%. The TiN(O) thickness is ~17 nm. Anneals at 600°C result in a more dealloyed Ag layer, with a residual Ti concentration as low as 0.9 at.%.

Figure 3.2 shows the residual Ti concentration as a function of annealing time for an Ag(26 at.% Ti) alloy. For all temperatures rapid dealloying occurs within the first 10 minutes; thereafter little or no further outdiffusion of Ti takes place. On the other hand, strong temperature dependence is evident. Ag(Ti) alloys with initial Ti concentrations of 6, 10 and 19 at.% showed similar dealloying behavior.

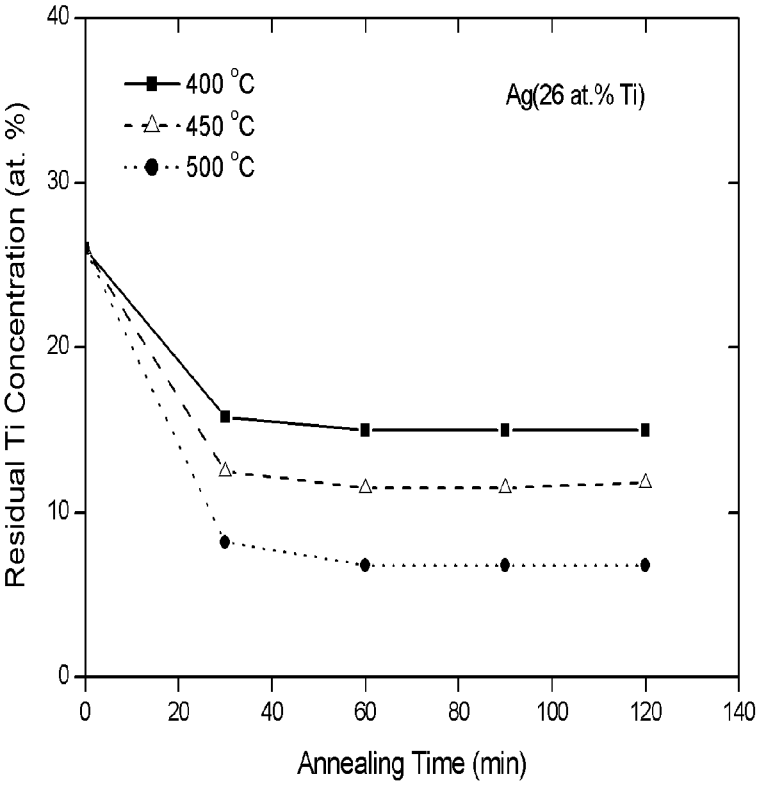

Figure 3.2. Dealloying kinetics obtained with Ag(26 at.% Ti) alloy films. The residual Ti concentration is shown as a function of annealing time for three different temperatures. The annealing took place in a NH_3 ambient and the data was obtained using 2.0 MeV He^{+2} RBS [9].

Resistivity versus annealing time for an Ag(19 at.% Ti) alloy, annealed at three different temperatures is shown in Figure 3.3. The resistivity drops rapidly within the first 10 minutes from the high value (~109.0 μΩ-cm) of the as-deposited sample to ~8 μΩ-cm at 500°C. The initial rapid drop is temperature dependent and the resistivity change is much slower for longer annealing times. This behavior is observed for alloy concentrations of 6–26 at.%.

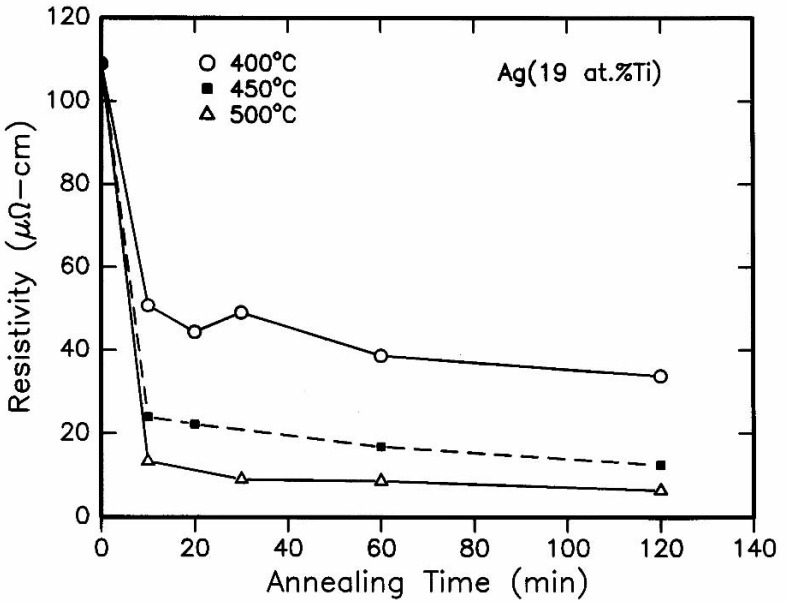

Figure 3.3. The resistivity as a function of annealing time is shown for an Ag(19 at.% Ti) alloy, nitrided at different temperatures in NH_3 [9]

3.2.4 Discussion

Nitridation annealing of Ag-Ti alloys above 300°C resulted in Ti segregating at the surface as well as at the interface. At the surface, Ti reacted with NH_3 and residual O_2 to form a TiN(O) layer, and at the interface with SiO_2 to form an oxide-silicide bilayer structure.

The Ti-nitride thickness obtained from nitridation of the Ag(Ti) alloys increases moderately with temperature in the range 300–600°C, but reaches a finite thickness (~20 nm) at higher temperatures. The amount of Ti available for reaction is controlled by the dealloying mechanism, as reflected by the relationship between the residual Ti concentration and annealing temperature [8].

In the case of Ag-Ti the Ti/SiO_2 reaction occurs at temperatures as low as 350°C. Earlier studies have indicated that significant reaction between pure Ti on SiO_2 only occurs at temperatures ≥600°C. AES depth profiling analysis has supported the RBS analysis that nitridation of the Ag-Ti alloys results in the formation of a Ti-oxide/Ti-silicide structure at the alloy and SiO_2 interface. RBS analysis indicated no segregation of Ag to the Ti-oxide/Ti-silicide interface for an Ag(19 at.% Ti) alloy nitrided in NH_3. Calculations based on the heats of reaction using the heats of formation of binary alloys, yielded positive values for the change in enthalpy in all cases. That is, there is no thermodynamic driving force to initiate the Ag-Ti_5Si_3 reaction (in contrast to the favorable Cu-Ti_5Si_3 reaction observed in

Cu(Ti) alloys). This explains the stability of the silver in contact with the interfacial layers.

Time-dependent dealloying curves for Ag(Ti) alloys are all characterized by an very rapid initial drop in the Ti concentration within the first 10 minutes followed by a plateau, which is associated with a small dealloying rate. The residual Ti showed a strong temperature dependence, namely, at higher temperatures lower Ti concentrations are obtained. A similar behavior is found in the formation and kinetics of titanium nitride in Ag/Ti bilayers.

Nitride growth is linear ($x \propto t$) in the range 0–15 minutes and parabolic ($x \propto t^{1/2}$) for 15–120 minutes. The latter kinetic model implies that a diffusion-controlled layer is likely to be the rate-limiting process governing the nitridation reaction. The nitride growth can be limited by diffusion of the reagents (NH_3 or Ti). For example, Ti diffuses faster through an Ag(100 nm)/Ti(50 nm) bilayer than Ag(200 nm)/Ti(50 nm).

The alloy results further suggest that the rate-limiting step in the encapsulation is not the mass transport and reactions within the encapsulating layers. Otherwise, substantially lower residual Ti concentrations would be obtained in Ag(6 at.% Ti) compared to Ag(26 at.% Ti) alloy. After being annealed at 500°C for 60 minutes, these alloys contained residual Ti concentrations of 3.2 and 6.8 at.%, respectively.

More dealloying in Ag(6 at.% Ti) alloy would have resulted if the rate-limiting step was in the TiN formation. The kinetics are instead likely to be controlled by the release and transport of the refractory metal in the Ag film.

The factor of 3 increase in grain size, observed after a 500°C anneal is not a significant enough change to consider Ti mass transport by grain-boundary diffusion as the limiting process. However, the effect of this increase in grain size has a significant effect on the grain boundary volume available to accommodate the Ti atoms upon annealing.

After being annealed above 450°C in NH_3, the Ag-Ti alloys consist of a TiN(O) passivation layer, a Ag layer and a Ti-oxide/Ti-silicide bilayer at the alloy/SiO_2 interface. It is assumed that this structure resembles a parallel-resistor configuration that the conductor (Ag) has the lowest resistance (R_{cond}) and it is also the thickest layer. Therefore, $1/R_{cond} \gg 1/R_{passivation}$ ($R_{passivation}$, resistance of encapsulation) and $1/R_{total} \sim 1/R_{cond}$ or $R_{total} \sim R_{cond}$ (after annealing). This assumption simplified the calculation of the resistivity and resulted in an error of less than 1%.

The resistivity of the nitrided samples is higher than the elemental values. The lowest resistivities obtained after nitridation for the Ag(Ti) alloy annealed at 500°C for 30 minutes is 7 μΩ-cm. The higher than elemental resistivity values observed are believed to be attributed to the following two factors.

Firstly, the presence of residual Ti in the encapsulated Ag films has a great effect on the resistivity. Time- and temperature-dependent studies of the dealloying process indicated incomplete dealloying. Even alloys with initial compositions as low as 4–6 at.% contained up to 1% residual Ti after nitridation at ~600°C. Lowering the initial Ti concentration would not necessarily lower the resistivity. Marecal *et al*. have demonstrated the effect of grain size on the resistivity of Ag films sputter-deposited on biased glass and silicon substrates [10]. A grain size change from 28 to 38 nm resulted in a resistivity change from 3.7 to 2.2 μΩ-cm for

Ag on glass and from 3.5 to 1.6 μΩ-cm for Ag/Si. It has also been shown that the resistivity of a TiO_2-passivated Ag layer decreased with annealing temperature due to increased grain size, from 50 nm for as-deposited sample to 300 nm after annealing at 600°C [11]. It is believed that annealing of the Cu(Ti) and Ag(Ti) alloys in NH_3 initiated microstructural changes and other competing reactions within the first 10 minutes, inhibiting the dealloying.

A second factor that may influence the resistivity is the formation of intermetallics as a result of the reaction between the Cu (or Ag) and Ti. However, glancing-angle X-ray diffraction analysis of the Ag-Ti and Cu-Ti alloys, could not verify intermetallic formation in either system. It has been shown that nitridation of Cu(Ti) alloys results in segregation of Cu to the Ti-oxide/Ti-silicide interface. Therefore, the effective thickness of the Cu layer is reduced and this also led to an increase in resistance of the encapsulated Cu films. Comparison of RBS data of the Ag and Cu systems indicated no such segregation of Ag to the Ti-oxide/Ti-silicide interface.

3.2.5 Conclusions

Nitridation of Ag-Ti alloys on SiO_2, in NH_3, resulted in a multilayer structure consisting of a TiN(O) surface layer, a dealloyed Ag layer, and an interfacial Ti oxide-silicide bilayer. The evolution of the final structure is therefore governed by a competition between the free surface nitridation/oxidation and the interfacial reaction. The dealloying behavior was characterized by a rapid decrease in residual Ti concentration within the first 10 minutes, followed by a much slower diffusion rate. The residual Ti showed a strong temperature dependence; at higher temperatures lower Ti concentrations are obtained. It is evident that the rate-limiting step in the encapsulation is not the mass transport and reactions within the encapsulating layers.

Resistivities >2 μΩ-cm have been obtained from the encapsulated Ag films. The main cause of the higher than elemental resistivities is due to the incomplete dealloying that occurs during the nitridation. The relationship between the residual Ti concentration and resistivity indicated that the former is controlled by the dealloying mechanism.

3.3 Corrosion of Encapsulated Silver Films Exposed to a Hydrogen-sulfide Ambient

3.3.1 Introduction

Silver, unlike a metal such as aluminum, lacks the property of self-passivation and this deficiency makes it susceptible to oxidation and corrosion during processing [12]. Dry silver does not form a significant surface oxide under atmospheric conditions. Czandema showed that at most one monolayer of oxygen atoms adhere to the silver surface [13].

However, when exposed to an atmospheric environment containing reduced sulfur gases and either particulate or gaseous chlorine, silver forms corrosion films consisting largely of Ag_2S, with some AgCl in high chloride environments. Alloys of silver behave as does the metal itself unless the alloying element is more reactive than silver. For example, in the case of "sterling silver" (90% Ag±10% Cu), the principle corrosion product in a reduced sulfur atmosphere is Cu_2S, reflecting the fact that the sulfidation rate of copper is an order of magnitude or much larger than that of silver [14]. Self-diffusion of unprotected silver surfaces induces agglomeration of the Ag when annealed at temperatures as low as 200°C in air. The significant self-diffusion of Ag films during annealing in air is caused by the absorption of Cl from the air and not by the involvement of oxygen from the ambient.

Design of back-end-of-line (BEOL) metallization structures for ultra large scale integrated (ULSI) circuit technology will require careful consideration of the following electrical and mechanical reliability concerns of the materials used: (1) resistivity below 3 μΩ-cm, (2) minimal electromigration, (3) metal line adhesion to dielectrics [15], (4) diffusion barriers to prevent interdiffusion between different metal levels [15], (5) minimize corrosion during processing and, (6) prevention of agglomeration upon heating. All these properties except for the low resistivity are expected to be improved from "encapsulation" of the metal line structures. This can be accomplished by element additions using Al, Mg, Ti, or Cr to form interfacial and surface reactions.

These reactions form layers that may provide adhesion, diffusion barriers, corrosion protection and structural reinforcement, which aid the resistance to electromigration and agglomeration. Ag films have been successfully passivated by annealing Ag/Ti bilayers in an oxidizing ambient. The Ti segregates to the free surface to form a TiO_2 film, which prevented agglomeration of Ag during subsequent annealing in air.

3.3.2 Experimental Details

Silver-titanium alloy films of approximately 200 nm thick were co-deposited by electron-beam evaporation with base pressure of $\sim 4\times10^{-8}$ Torr onto thermally oxidized Si(100) substrates with a SiO_2 thickness of ~200 nm. The pressure rose to $\sim 1\times10^{-7}$ Torr during deposition.

The initial alloy concentration was 19 at.% Ti. Deposited film composition and thickness were measured with Rutherford backscattering spectrometry (RBS). Anneals were performed in a Lindberg single-zone quartz-tube furnace in a flowing electronic grade (99.99%, with $H_2O<33$ and O_2+Ar <10 molar ppm) ammonia (NH_3) ambient. After loading the samples in the furnace, the tube was sequentially pumped and purged (with ammonia) a minimum of three times. The NH_3 flow rate was ~2 l/min, and the anneal temperatures ranged from 300±700°C for 30 minutes. The annealed samples were allowed to cool in the flowing NH_3 before removal from the furnace.

The free surface reaction of Ti with the NH_3 ambient, as well as the Ti-SiO_2 interfacial reactions was analyzed by RBS. RBS analysis was performed using

a 1.7 MV Tandem accelerator with a 2.0–2.3 MeV He^{+2} beam at 7° tilt and total accumulated charge of 20 μC.

To evaluate the effectiveness of the TiN encapsulation as passivation layers against corrosion of Ag, the nitrided structures were annealed in a static hydrogen sulfide (H_2S) ambient. Quartz test tubes were cleaned with an aqua regia (three parts concentrated HCl:one part concentrated HNO_3) acid solution, rinsed with de-ionized water and dried in an oven at 100°C. After the nitrided samples were placed in the test tubes, they were evacuated to ~5×10^{-5} Torr, and then backfilled with H_2S to a sub-atmospheric pressure of ~356 Torr. Anneals were performed with a wire furnace at temperatures ranging from 100–500°C for 30 minutes. The furnace was placed around each test tube with sample while connected to the gas handling manifold.

During anneals, the H_2S pressure remained essentially constant. For comparison purposes, as-deposited Ag(19 at.% Ti) alloys and elemental Ag on SiO_2 were also annealed under the same conditions. A Leica 440 scanning electron microscope (SEM) operated at voltages between 15 and 25 kV and in secondary mode was used to evaluate the morphology of the corroded surfaces.

3.3.3 Results

Figure 3.4 compares the RBS spectrum of the as-deposited Ag(19 at.% Ti) alloy with that nitrided at 600°C for 30 minutes in an NH_3 ambient. After a 600°C anneal, the presence of a Ti-surface peak and a distinct interfacial Ti peak indicate that Ti segregated to the free surface and also reacted with the SiO_2 substrate. The Ti segregating to the free surface reacted with the NH_3 ambient to form a Ti-nitride layer, labeled as "TiN(O)" in the schematic accompanying the spectrum. At the alloy/SiO_2 interface, the Ti dissociates the SiO_2 and subsequently reacts with the freed Si and O to form an interfacial Ti-oxide/Ti-silicide bilayer structure.

These layers are labeled as "TiO" and "Ti_5Si_3", respectively. Computer RUMP simulation of the spectrum corresponding to the 600°C anneal, suggests that the dealloyed Ag layer contains a residual Ti concentration of ~0.9 at.%. The TiN thickness is ~20 nm.

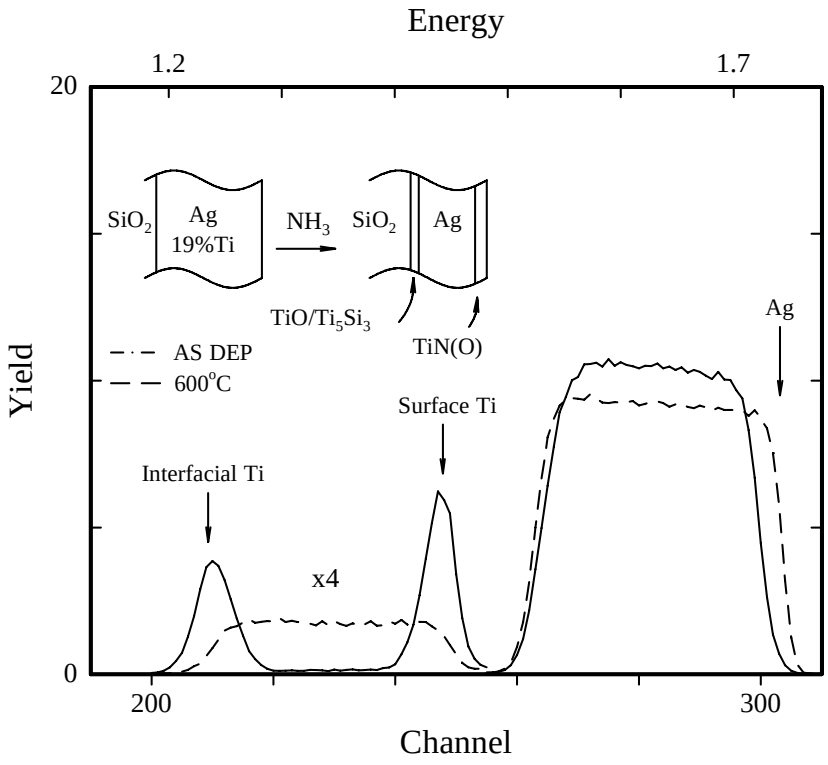

Figure 3.4. RBS spectra showing only the depth distributions of Ag and Ti of a 210-nm thick Ag(19 at.% Ti) alloy, before and after annealing at 600°C for 30 minutes in NH_3. A 2.0 MeV He^{+2} beam energy was used [12].

Figure 3.5a shows the RBS spectra of a 170 nm thick Ag film on SiO_2 before and after annealing in a H_2S ambient. Annealing the Ag/SiO_2 structure at 100°C for 30 minutes results in sulfidation of the Ag film, as can be seen by the presence of a small S peak near channel 240. The sulfur peak has been blown up 20 times to make it more visible. Silver reacts with the H_2S ambient to form a silver-sulfide layer of ~11 nm. The slope on the left of the Ag signal is indicative of some surface roughness induced by the corrosion. The presence of the small sulfur peak (blown up 20 times) on the RBS spectrum of the as-deposited Ag(19 at.% Ti) alloy after annealing in H_2S at 100°C for 30 minutes indicates that corrosion of the alloy has occurred (Figure 3.5b). The silver sulfide layer is also 11 nm thick. The RBS data suggest that only corrosion of the silver occurs, since the spectrum shows depletion of Ag in the surface region, and a slight decrease in the layer thickness. The Ti peak does not show any changes.

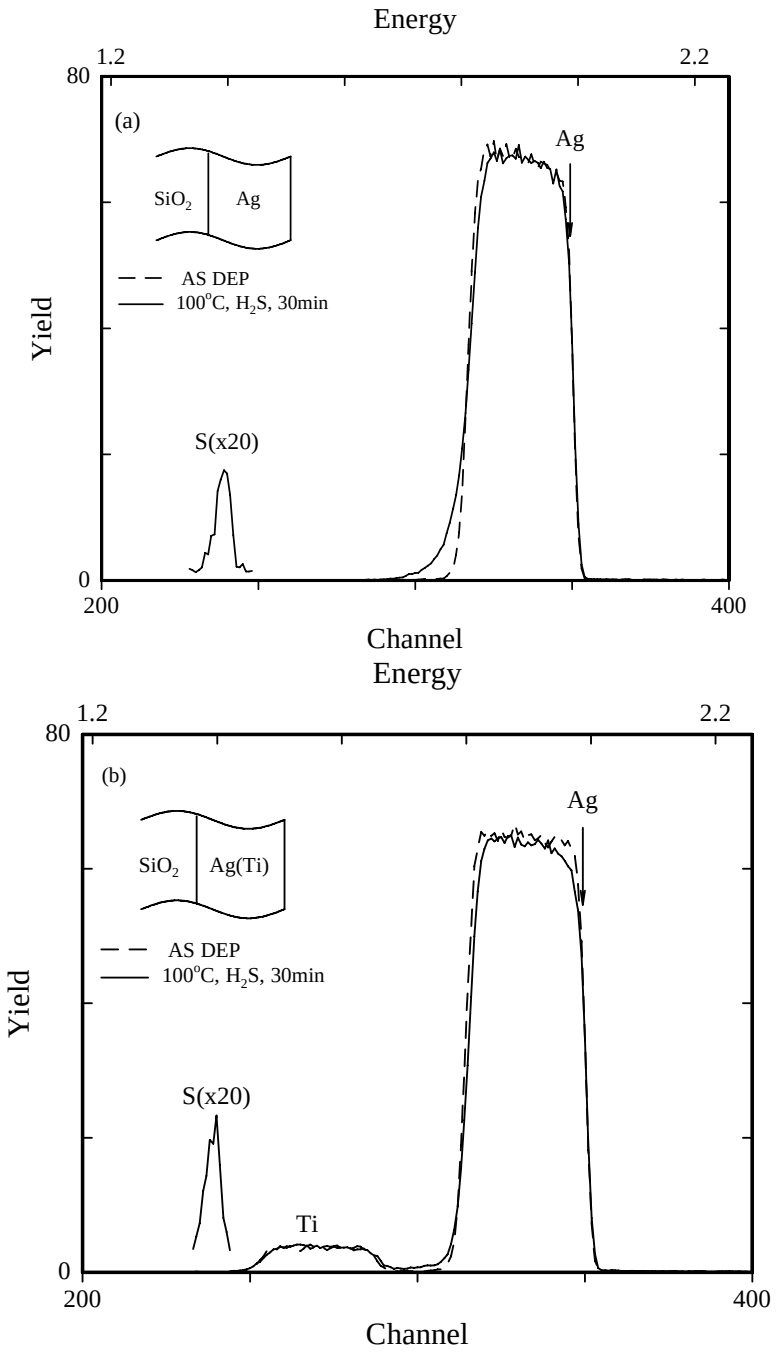

Figure 3.5. RBS spectra of a (a) 170-nm thick sputter-deposited Ag film on SiO_2 and (b) Ag(19 at.% Ti) alloy film, before and after annealing at 100°C for 30 minutes in H_2S. A 2.3 MeV He^{+2} beam energy was used [12].

However, RBS analysis suggest that annealing a TiN(O) encapsulated Ag fillm in H_2S at various temperatures for 30 minutes indicates that no corrosion occurs up to 300°C (Figure 3.6). The sample surfaces retained their smoothness, and golden color, and no difference between the sample at 300°C (in H_2S) and the nitrided (no sulfur anneal) one could be detected. After a 400°C anneal, the RBS spectrum displays the following features: (1) a reduction in the height and thickness of the Ag signal, (2) a weak S peak near channel 240, (3) shift of the interfacial Ti signal to higher energies, and (4) a broad tail. The first three features point to the formation of a silver-sulfide compound as a result of Ag migration through the Ti-nitride to react with the H_2S at the free surface. However, the broad tail on the spectrum indicates the presence of a discontinuous Ag surface layer.

Annealing the nitrided sample at 500°C for 30 minutes in H_2S results in an almost complete diffusion of Ag to the surface. The two Ti signals (interfacial Ti and surface Ti) merge as a result of this outdiffusion. A much larger S peak is also present.

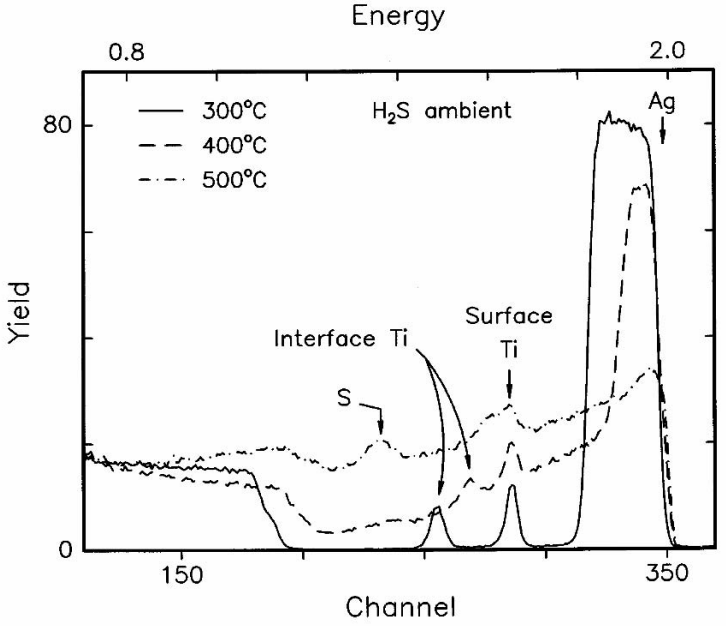

Figure 3.6. Ag(19 at.% Ti) alloy was nitrided at 600°C for 30 minutes in NH_3. The RBS spectra show depth distributions of the nitrided alloy, after annealing at 300, 400 and 500°C for 30 minutes in H_2S [12].

The RBS analysis was supplemented by scanning electron microscopy (SEM). SEM analysis of the 500°C annealed sample shows the presence of a discontinuous layer of faceted crystallites. The sample annealed at 500°C has a much higher density of crystallites than 300°C, and some crystals coalesced to form clusters. At temperatures ≥300°C the majority of the crystallites display a rhombic shape, although a few cubic crystals are also visible.

3.3.4 Discussion

Nitridation anneals of Ag(19 at.% Ti) alloy at 600°C resulted in Ti segregating at the surface as well as at the interface. The dealloying process appears to take place by Ti out-diffusion presumably grain-boundary diffusion in Ag with a diffusion coefficient, which is estimated to be larger than 10^{-12} cm^2/s. At the surface, Ti reacted with NH_3 and residual O_2 to form a TiN(O) layer of about 20 nm thick; and at the interface, Ti reacted with SiO_2 to form an oxide-silicide bilayer structure. The large negative heat of formation of TiO_2 (222–365 kJ/mol) compared to that of TiN (169 kJ/mol) is compensated by the high partial pressure of NH_3 relative to that of O_2, leading to nitride rather than oxide formation. The smaller thermal decomposition energy of NH_3 (432 kJ/mol) compared to N_2 (942 kJ/mol), makes it possible to form Ti-nitride at relatively lower temperatures. It has been observed that at a given temperature (>300°C) similar amounts of Ti diffuse to both the surface and interface, which implies that the two reactions are in competition for the finite amount of Ti atoms available. The amount of Ti available for reaction is controlled by the dealloying mechanism.

Earlier studies also suggest that the reaction between Ti and SiO_2 already occurs at temperatures as low as 350°C. The interfacial reaction starts with the dissociation of SiO_2, the released oxygen and silicon react with Ti to form the interfacial layers. The layers were identified as TiO and Ti_3Si_5 [15].

Silver-sulfide films have been recognized as the major corrosion products on silver and silver-alloys. Both atmospheric corrosion and laboratory experiments involving mixed corrosive gases reveal that acanthite (Ag_2S) is a dominant phase. Hydrogen sulfide (H_2S) was identified as one of the primary atmospheric constituents responsible for the degradation of silver, therefore, it “accelerates” the corrosion of the Ag(Ti) alloys. Alloys of silver produce corrosion products that reflect the most reactive of the alloyed metals. For the Ag(Ti) alloys, it seems that Ag is the reactive component, when annealed in H_2S ambients. SEM studies showed that the majority of crystallites after corrosion display a rhombic shape, although a few cubic crystals are also present. These observations suggest that the corrosion product is Ag_2S, since acanthite is rhombic and argentite is cubic. This is in agreement with quantitative energy dispersive spectroscopy (EDS) analysis in which a Ag/S ratio of, 2.15 was found. It has been shown that Ti is resistant to H_2S corrosion [16]. Therefore, it is believed that Ag_2S (acanthite) is the major corrosion product formed during the sulfidation of the Ag(Ti) alloys. However, the role (if any) of Ti during the corrosion process is not clear. The results indicate that as-deposited elemental Ag and Ag(Ti) alloys, both corroded after being annealed at 100°C for 30 minutes in H_2S.

The evolution of the corrosion of encapsulated Ag films is depicted schematically in Figure 3.7. After a 400°C anneal, Ag diffuses through the Ti-nitride layer to form Ag_2S crystallites, on the surface. The well-defined sulfur peak on the spectrum of the sample annealed at 500°C, suggest that the crystallites are Ag covered with a 133 nm thick layer of Ag_2S. If the crystallites consisted only of Ag_2S non-uniformly distributed over the surface, then the sulfur peak would have been smeared out. At 500°C, nearly all the Ag had migrated to the surface to react with H_2S. It seems that the Ti-nitride barrier fails by allowing diffusion of Ag

through it, without itself being dissolved. It is believed that the diffusion occurs along grain boundaries and possibly microvoids, pinholes, cracks and weak spots in the barrier layer. The fact that the TiN passivation layer essentially remains intact upon failure is also an indication that neither Ti (nor N) reacts with Ag or the H_2S ambient at this temperature. Therefore, the migration of Ag to the surface is driven by the thermodynamically favorable reaction between Ag and H_2S.

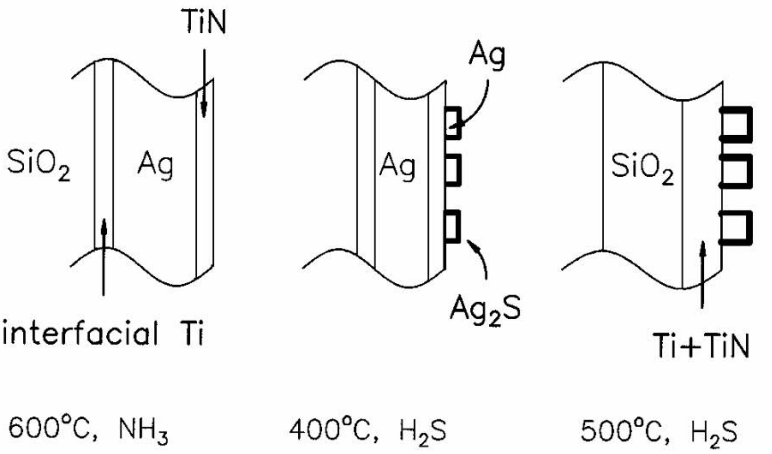

Figure 3.7. Schematic showing the nitridation and evolution of the corrosion process of a Ag(19 at.% Ti) alloy. At 600°C, in NH_3, the Ti forms TiN at surface and interfacial TiO/Ti_5Si_3 bilayer structure to encapsulate the Ag. At 400°C, in H_2S, some Ag diffuses through TiN to form faceted crystallites; at 500°C most of the Ag has moved to the surface to react with the H_2S ambient [12].

3.3.5 Conclusions

Nitridation of Ag-Ti alloys/bilayers on SiO_2, in NH_3, resulted in a multilayer structure consisting of: a TiN(O) surface layer, a dealloyed Ag layer, and an interfacial Ti oxide-silicide bilayer. Ti-nitride layers of thicknesses of ~20 nm are formed at 600°C [12]. Corrosion of TiN-encapsulated silver thin films in the presence of a severe hydrogen-sulfide ambient produces a non-uniform surface layer of rhombic and cubic Ag_2S crystallites.

Evaluation of the Ti-nitride encapsulation as protection for Ag against corrosion in H_2S, showed stability up to 300°C. The unprotected Ag(Ti) alloys and pure Ag on SiO_2 corroded at 100°C, when annealed under the same conditions. Numerous studies have shown that tarnishing of Ag occurs at room temperature and with diluted H_2S concentration levels of <300 ppb. Therefore, the Ti-nitride will be an excellent passivation for silver under atmospheric conditions with degradation occurring only above 300°C [12].

3.4 Tantalum-Nitride Films as Diffusion Barriers

3.4.1 Introduction

The properties of TaN films are extremely sensitive to film microstructure and morphology. The chemical composition, microstructure, and properties of TaN films depend strongly on the deposition parameters, pre-treatment, substrate type, and film thickness. Diffusion barriers are used to prevent degradation of devices as a result of poor adhesion and interdiffusion. The objective of research efforts to date was to find an intermediate layer between the interconnect Ag metal and the underlying dielectric that will act as both an adhesion promoter and an effective diffusion barrier between interconnect metal and adjacent materials.

3.4.2 Experimental Details

Tantalum nitride films with nominal thicknesses of about 100 nm were deposited onto Si (100) substrates by DC magnetron reactive sputtering using various N_2/Ar gas flow ratios (15–40% N_2). A power of 3 kW and a pressure of 8 mTorr were used. The total flow rate was 100 sccm.

Single-crystal silicon substrates were used, without any specific pre-deposition clean to remove native oxide. The Ta sputter target was bigger (~ 300–325 mm) than the substrate wafer (~200 mm) in order to enhance uniformity of the deposited film. The target-to-substrate separation distance was ~10 cm. During deposition, the substrate was electrically floating and was held stationary at a temperature of 250–260°C. Rutherford backscattering spectrometry (RBS) using energies of 2–4.3 MeV and total accumulated charge of 10–20 μC were used to analyze the nitrogen content, oxygen content and composition of the TaN films. The 3.0 MeV and 3.7 MeV beam energies correspond to oxygen (O) and nitrogen (N) resonances, respectively, and were used to detect O and N. The 3.0 MeV analyses were carried out at a tilt angle of 65° to increase the relative depth. The RUMP computer simulation program was used to analyze the RBS spectra. The phases of the as-deposited TaN films were investigated by glancing angle as well as theta-2 theta X-ray diffraction analysis (XRD) using a Philips X'pert MPD diffractometer with a Cu K_α radiation source. A working voltage of 45 kV was employed and filament current was 40 mA. Joint Committee for Powder Diffraction Standard (JCPDS) cards was used for phase identification [17]. To investigate the properties of TaN film as a diffusion barrier for Ag metallization, a 100 nm–thick Ag layer was electron-beam deposited on top of the barrier. The samples were annealed at temperatures ranging from 450°C to 700°C for 30 minutes in a vacuum furnace. The annealing chamber was pumped down to about $1x10^{-10}$ Torr. During annealing the vacuum in the furnace was about $1 x10^{-8}$ Torr. Sheet resistances of the TaN/Si and Ag/TaN/Si structures were measured, both before and after annealing, using four-point-probe analysis. The resistivity of the TaN/Si samples was calculated from the sheet resistance obtained from the four-point-probe measurements and the film thickness measured by a Tencor α-step profilometer.

XRD and RBS analysis using the same parameters and conditions as for the TaN/Si were also carried out on the Ag/TaN/Si structures before and after the vacuum anneals.

3.4.3 Results

Figure 3.8 shows the 3.0 MeV RBS spectra of the TaN films, prepared using different nitrogen flow ratios, on Si. When the nitrogen flow ratio increases to 30% and higher, the thickness of the film decreases. The decrease in thickness with increasing N_2 partial flow rate is attributed to a decrease in sputtering yield originating from nitridation of the metal target and/or low ionization efficiency of the nitrogen gas atoms. The height of the Ta signal decreases with increasing nitrogen partial flow. This lower Ta yield in the film is due to incorporation of the lighter element (nitrogen) into the film. At the energy of 3.0 MeV that corresponds to O resonance no oxygen could be detected in the films within the detection limits of RBS. To show the presence of nitrogen in the surface layer and to determine the amount of nitrogen, RBS data were collected at 3.7 MeV (the resonance energy of N) with a 7°tilt. At the energy of 3.0 MeV, no O and N could be detected.

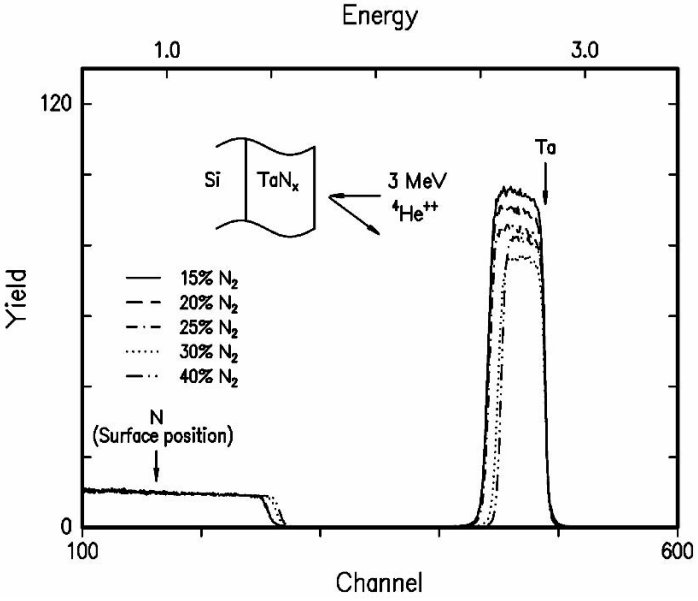

Figure 3.8. 3.0 MeV RBS spectra from TaN films sputter-deposited on Si, using different N_2/Ar flow ratios [5]

Figure 3.9 shows 3.7 MeV RBS spectra obtained from the tantalum nitride films prepared using different N_2 flow ratios. At this energy, which corresponds to N-resonance, large N peaks are visible. This data was used to quantify the nitrogen content and hence the composition of the samples. The results of these quantifications are given in Table 3.1.

Table 3.1. Compositions of the TaN films, based on RUMP simulation [5]

Nitrogen flow ratio (%)	Tantalum nitride composition
15	$Ta_{0.78}N_{0.22}$
20	$Ta_{0.64}N_{0.36}$
25	$Ta_{0.55}N_{0.45}$
30	$Ta_{0.51}N_{0.49}$
40	$Ta_{0.45}N_{0.55}$

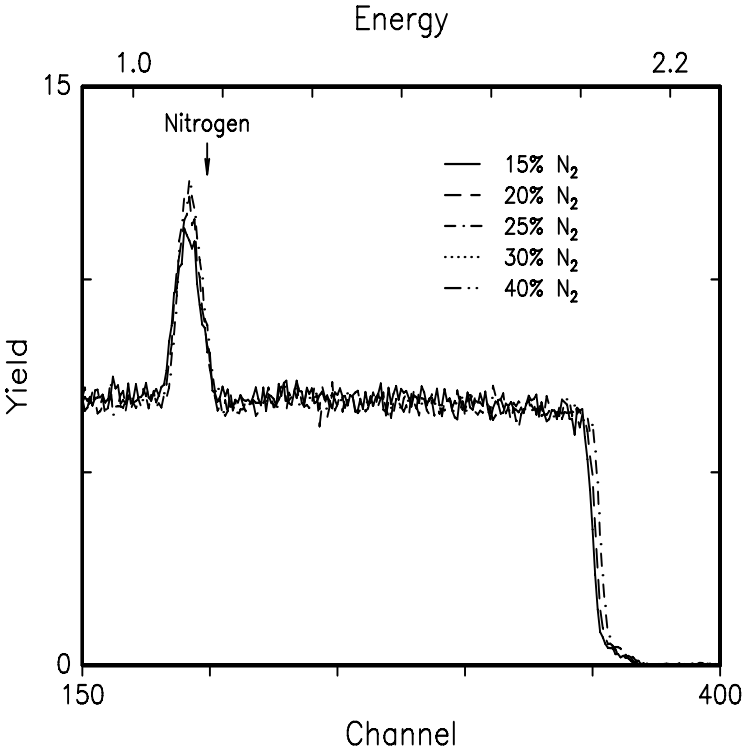

Figure 3.9. 3.7 MeV RBS spectra from TaN films sputter-deposited on Si using different N_2/Ar flow ratios. N-resonance peaks are clearly visible at this energy [5].

The XRD spectra obtained from the TaN films, deposited on Si using different nitrogen flow ratios, are shown in Figure 3.10. The variations in position, intensity and shape of the peaks indicate changes in the phase of the TaN films. From Figure 3.10, the phases present in the films were identified by comparing the observed peak positions (2θ) in the XRD spectra with data from JCPDS cards. The diffraction peaks of the films deposited with 15% nitrogen flow (Figure 3.10a) can be indexed as belonging to a mixture of β-Ta and Ta-rich nitride (Ta_2N). When the nitrogen partial flow rate is increased to 25% (Figure 3.10b), a small fraction of the phases observed at 15% are still present, but the dominant phase is stoichiometric TaN. Upon increasing the flow rate from 30–40%, only peaks at 2θ = 35°, 41, 60, and 72°, which correspond to TaN, are observed (Figure 3.10c–d). As the nitrogen flow ratio is increased to 30%, the diffraction peak at 2θ ≈ 35° shifts to a lower angle, and the shift becomes even more evident for the 40% spectrum. The shift of the peaks to lower angles confirmed that a new phase is formed with increasing nitrogen. In the range of 30–40% N_2 flow rate, the diffraction peaks become increasingly broader and peak intensities drop.

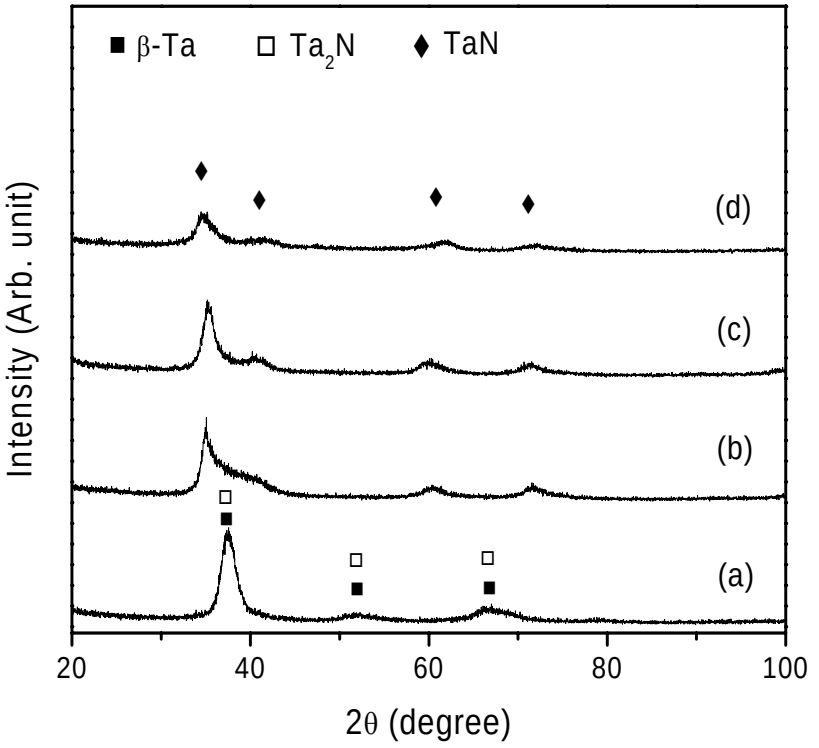

Figure 3.10. XRD spectra obtained from TaN films as-deposited using various N_2/Ar flow ratios, (a) 15% N_2, (b) 25% N_2, (c) 30% N_2 and (d) 40% N_2 [5]

Figure 3.11 shows the resistivity of the reactively sputtered TaN films as a function of nitrogen flow ratio. For reference purposes, the resistivity of β-Ta [18] is indicated on Figure 3.11. A noticeable increase in resistivity is observed when the nitrogen flow rate is changed from 15 to 20%. As flow rate is increased from 20 to 30% the resistivity of the TaN film increases slightly, from 155 to 169 μΩ-cm. When flow rate is further increased, the resistivity of the film increases drastically to a value of 532 μΩ-cm at 40%. The change in film resistivity will be discussed in terms of the TaN material characteristics later.

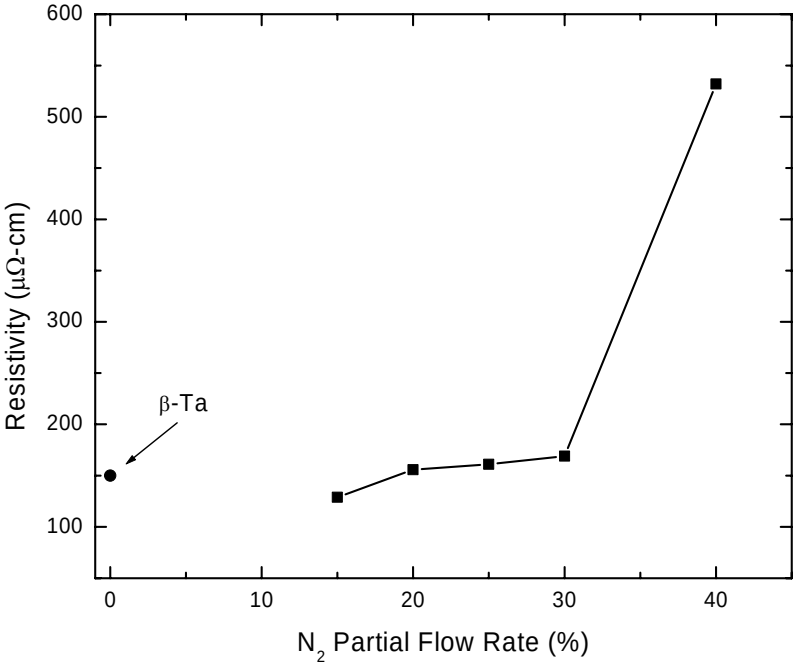

Figure 3.11. Resistivity of the TaN films as a function of nitrogen partial flow rate. For reference purposes, the resistivity of β-Ta is indicated [5].

To evaluate the effectiveness of the TaN films as diffusion barriers, a silver film about 100 nm in thickness was deposited on the TaN of different phases. Thermal stability of the diffusion barrier was evaluated by annealing the samples at temperatures of 450–700°C for 30 minutes in a vacuum of about 10^{-8} Torr. The samples still showed the original shiny silver color. The data revealed that no interdiffusion occurred between Ag and TaN for temperatures up to 650°C for 30 minutes. The as-deposited spectrum overlaps with the annealed spectra for annealing up to 650°C. Similar results were obtained for nitrogen flow ratios of 20–40%.

In order to resolve the Ta and Ag peaks, RBS data were collected at 4.3 MeV (the resonance energy of carbon). Figure 3.12a presents RBS spectra showing the

Ag and Ta peaks for the Ag/TaN films prepared using different N_2 flow rates, as-deposited, and after annealing at 700°C for 30 minutes in vacuum. With the peaks well separated at the higher analysis energy, the presence of Ta at the surface is more clearly evident.

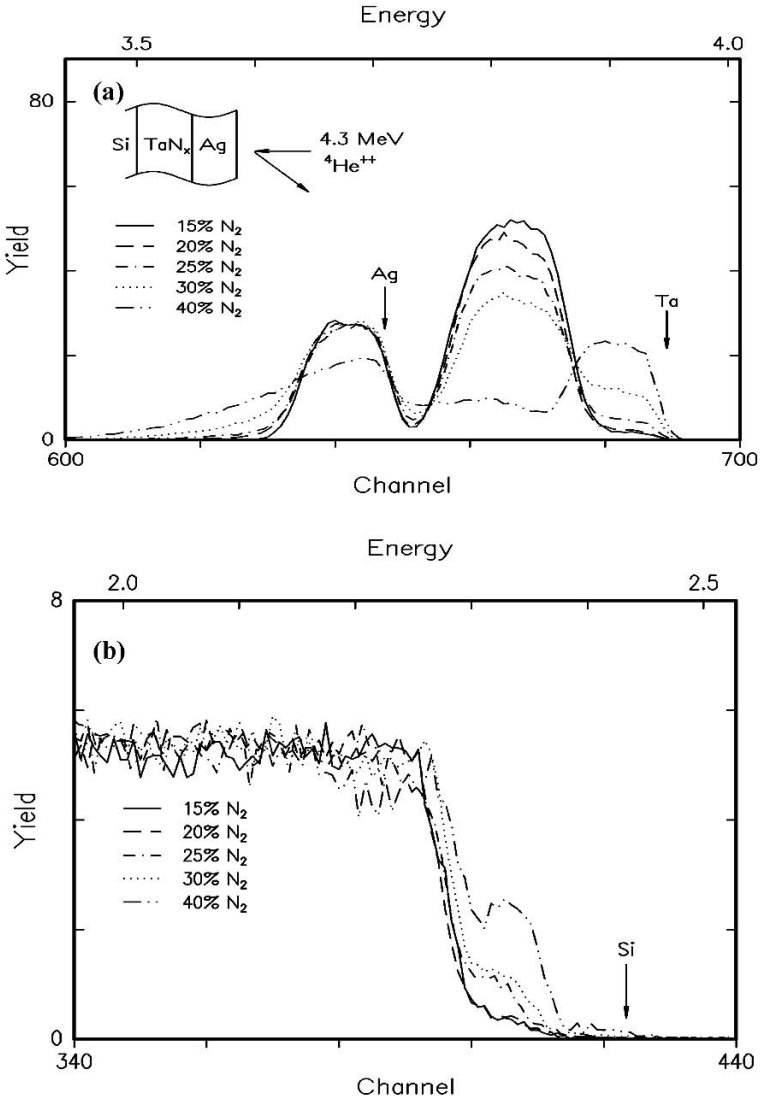

Figure 3.12. RBS spectra obtained from Ag/TaN prepared using different N_2 flow rates and annealed at 700°C for 30 minutes in vacuum. Figure 6a shows the Ta and Ag signals, whereas the Si signals are shown in Figure 6b [5].

The spectra showed that after the 700°C anneal, the amount of tantalum at the surface increases with increasing N_2 flow rate (Figure 3.12a). It is also noticeable from Figure 3.12a that as the N_2 flow rate increases the trailing edge of the Ag peak broadens. This broad tail indicates the presence of a discontinuous Ag layer or extensive de-wetting of the Ag. In Figure 3.12b only the Si signal is shown in order to facilitate the evaluation of any reactions between Ta and Si as well as to evaluate the possible presence of silicon at the wafer surface. It can be seen from Figure 3.12b that Si is indeed present at the surface. An interesting feature, however, is the large step(s) at the leading edge of the Si signal. These step(s) are believed to be due to Ta-silicide formation at 700°C.

The variation of Ag sheet resistance as a function of annealing temperature is commonly used to examine the capability of diffusion barriers against metal diffusion. The difference in sheet resistance between annealed and as-deposited samples, divided by the sheet resistance of the as-deposited samples, is called the variation percentage of sheet resistance ($\Delta R_s/R_s$ %) and is defined as follows:

$$\frac{\Delta R_S}{R_S}\% = \frac{R_{S,annealed} - R_{S,asdeposied}}{R_{S,asdeposited}} \times 100\% \tag{3.1}$$

Figure 3.13 presents the variation percentage of sheet resistance of the Ag/TaN/Si samples. According to the data in Figure 3.13, the variation percentage is almost the same for all samples in the temperature interval 450–650°C, for 30 minute anneals. However, after annealing at temperatures > 650°C a change in the sheet resistance is observed for all of the Ag/TaN/Si structures. The smallest change is for the 15% flow rate and the largest change is for the 40% flow rate. The data show that the extent of change in sheet resistance, for annealing temperatures > 650°C, varies with the nitrogen flow rate.

In terms of electrical properties, it appears that barrier stability decreases with increasing N_2 flow rate with 15% N_2 resulting in the most stable barrier structure. The change in variation of sheet resistance for the higher temperature anneals (> 650°C) is due to a combination of failure of the diffusion barrier and de-wetting of the Ag on the TaN. The failure of the diffusion barrier, expressed in terms of the variation of percentage of sheet resistance, is in agreement with the RBS data presented earlier.

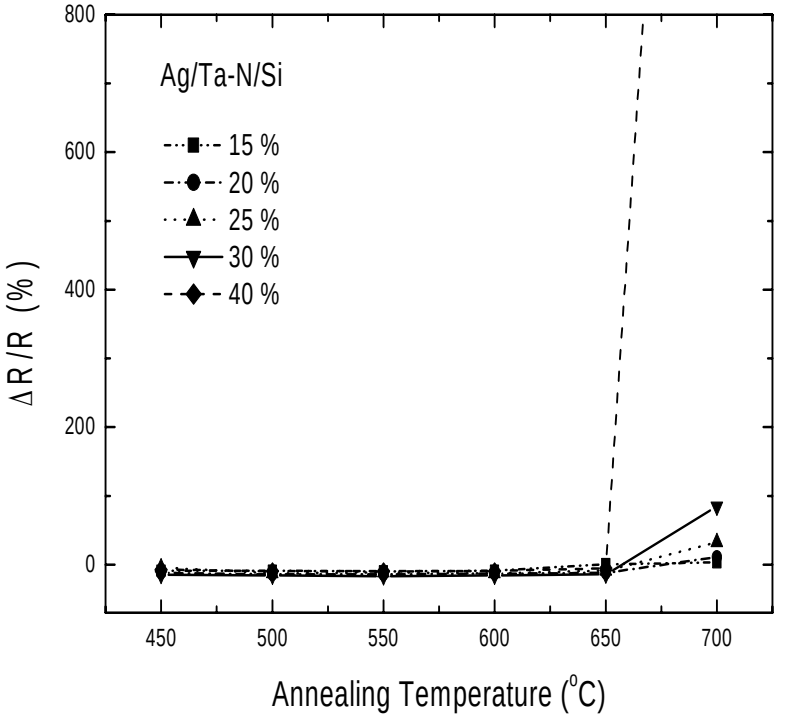

Figure 3.13. Variation percentage of sheet resistance versus annealing temperature for the Ag/TaN samples. The TaN films were reactive sputter-deposited using N_2 partial flow rates of 15–40% [5].

Therefore, based on the RBS data and electrical measurements, the TaN barriers formed with the 15–40% N_2 flow rate showed thermal stability up to 650°C. The behavior of sheet resistance of the Ag on the TaN diffusion barrier with different N_2 flow ratios can best be explained with XRD analysis. Figures 3.14a and b show X-ray diffraction patterns obtained from Ag on TaN diffusion barrier layers prepared using 20% and 25% N_2 flow ratios. The XRD results do not show any new phases in the Ag/TaN/Si films annealed at 600°C, when compared with the as-prepared Ag/TaN/Si structure. The XRD spectra show prominent Ag {111} and the TaN peaks identified in Figure 3.10. The intensity of the Ag {111} peak increases for the 600°C anneal. This implies that <111> texture in the Ag films is enhanced upon annealing. The TaN films remained stable and no reaction with Ag was observed.

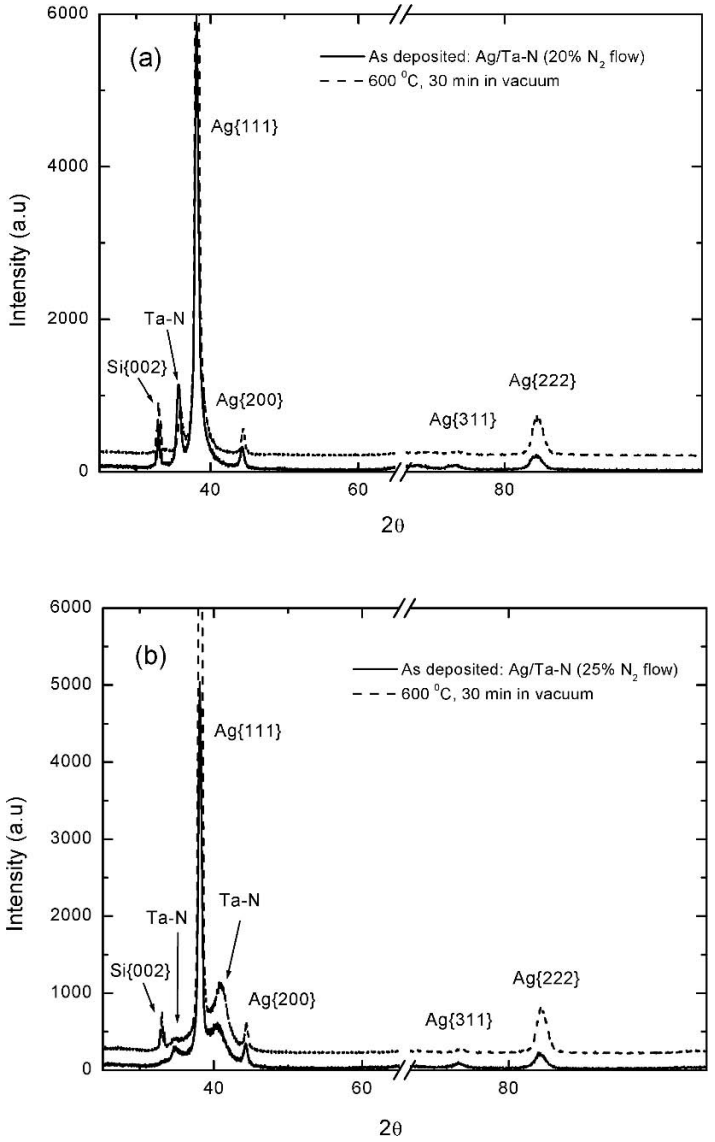

Figure 3.14. θ-2θ XRD patterns obtained from Ag film deposited on TaN that was reactive-sputter deposited using (a) 20% N_2 flow and (b) 25% N_2 flow, and then annealed at 600°C for 30 minutes in vacuum [5].

3.4.4 Discussion

The RBS data showed that the N_2 flow ratio influences the composition, phases, and thicknesses of the TaN thin films. From Table 3.1 it can be seen that the tantalum-to-nitrogen ratio resulting from the 25–40% N_2 flow rates is approximately 1:1. Within the detection limits of RBS, no oxygen was detected in the films using the resonance technique.

The XRD data enabled identification of the phases of the TaN films for the different N_2 flow rates. Increasing the nitrogen flow rate from 15 to 40%, results in the film material transforming from a metal-rich phase to a stoichiometric Ta-nitride phase. For the 15% N_2 partial flow rate, it follows from the XRD data that β-Ta and hexagonal Ta_2N coexist in the film. When the flow rate is increased to 25% N_2, an almost complete transformation to stoichiometric face-centered cubic TaN has occurred, with a small amount of the phases observed at 15% also being present. When the partial flow rate is increased from 30–40%, fcc-TaN is the primary phase observed. The results therefore indicate that increasing the amount of nitrogen in the sputtering gas induces a phase transformation from a mixture of β-Ta and Ta_2N to fcc-TaN. The broadening of the X-ray peaks and the decrease in intensity for partial flow rates >40% suggest that the higher nitrogen concentrations led to much smaller grains with random orientations or to the formation of an amorphous-like film. The shift in peak position towards smaller 2θ angles reveals the formation of a new phase. Such changes could be due to nitrogen incorporation. The broadening of the peaks in the XRD pattern is mainly due to smaller crystallite size. Stavrev *et al*. [19] showed that during deposition, the nitrogen is interstitially incorporated into the Ta-lattice and this leads to the formation of a metastable amorphous TaN material.

The electrical measurements in this study show that TaN film resistivity increases with increasing nitrogen content in the films. It has also been shown that with increasing nitrogen flow rate, the resulting phase of the TaN films changes from Ta-rich to stoichiometric tantalum nitride. The resistivity increase is therefore associated with a combination of increasing nitrogen content and change in phase of the films. Moderate changes in resistivity occur with the transition from a mixture of β-Ta and Ta_2N to the stoichiometric to fcc-TaN phase. The transition to fine-grained stoichiometric fcc-TaN or TaN with high disorder for partial flow rates > 30%, on the other hand, resulted in highly resistive films. In the Ta_2N structure, tantalum atoms are located at lattice sites of a hexagonal unit cell and nitrogen atoms occupy interstitial sites, which imply that the Ta_2N films contain a finite nitrogen concentration. It is believed that the high resistivity of the films at 40% N_2 partial flow rate is due to a combination of oversaturated TaN, amorphous-like structure of the TaN and the intrinsic high resistivity (~200–300 μΩ-cm) of stoichiometric tantalum nitride itself [20].

For flow ratios between 15–30%, resistivity values of ~129–170 μΩ-cm were obtained compared to 150–300 μΩ-cm reported for similar experiments. It is believed that this lower resistivity is due to minimal (<1 at.%) residual oxygen incorporated during sputtering, and hence the absence of any Ta-oxide compounds. Any residual oxygen present in the films will occupy interstitial sites and therefore

induce a significant amount of residual impurity resistivity. It has been shown that if the interstitial incorporation of nitrogen (at room temperature) into TaN exceeds thermal equilibrium levels, films with smaller grain sizes and subsequently with higher resistivity are formed. Grain growth of the fcc-TaN phase (observed in the flow range of 25–40%) may be inhibited because of the excess nitrogen atoms or because of nucleation of nitrogen-rich compounds, for example, Ta_3N_5. As a result, the grain size is smaller for increasing N_2 flow. It is generally known that the resistivity of materials depends on their purity and microstructure. Impurities and structural imperfections such as grain boundaries, dislocations and vacancies contribute to electron scattering and hence to increasing resistivity.

With regards to the TaN phases formed as a function of N_2 flow rate and the resulting resistivity, the results of the present work confirmed the successive appearance of Ta-rich and N-rich phases and an increase in resistivity with increasing nitrogen partial flow [5]. The broadening of the XRD peaks for flow rates above 30% N_2 is indicative of the near-amorphous nature of the films, which, in turn is mainly due to smaller crystallite size and decreasing long-range order in the films.

The RBS spectra from the as-deposited and vacuum annealed Ag/TaN on Si (450–650°C, 30 minutes) were found to be identical for the different nitrogen flow ratios [5]. No interfacial reaction between Ta and Si or interdiffusion of Ag was observed even after annealing at 650°C. No Ta was present at the surface at 650°C. However, after a 700°C anneal, the RBS spectra show Ta at the surface. The broad tails on the spectra indicate the presence of a discontinuous Ag surface layer. The broadening of the tail and the presence of Ta on the surface seem to increase with increasing N_2 flow rate. It appears that the barrier fails as a result of interfacial reaction between the TaN barrier layer and the underlying silicon substrate to form a Ta-silicide. The barrier failure was accompanied by de-wetting of Ag over the Ta-nitride resulting in a discontinuous Ag layer. These conclusions are supported by the broad tails on the trailing edges of the Ag, the steps at the leading edge of the silicon (Figure 3.12a and b), and the presence of Ta, Ag and Si at the surface.

The failure of the TaN barrier in contact with Ag and Si is driven predominantly by the large negative heat of formation, – 0.78 eV/atom, for reaction between Ta and Si to form a stable silicide. Reaction between Ag and substrate Si is not a significant concern because Ag does not form a stable silicide with silicon. RUMP simulation (of the RBS data) indicates the formation of $TaSi_2$. In the case of elemental Ta on Si, Ta-silicide ($TaSi_2$) is known to form by reaction of Ta with Si at temperatures between 550 and 650°C. Silicon is the moving species during such reaction between Ta and Si. Data from the present study indicates that in the Ag/TaN/Si system, formation Ta-silicide occurred at 700°C. This formation temperature is higher than in the case of elemental Ta on Si. The higher formation temperature, or delayed silicide formation, is due to the fact that TaN compound must first decompose to release the Ta necessary for the silicidation process.

In the investigation of amorphous-Ta_2N as a diffusion barrier against Cu inter-diffusion, it was shown that barrier failure is due to amorphous-to-crystalline transition and subsequent grain-boundary diffusion of copper to react with silicon.

It was also reported that the incorporation of excess interstitial nitrogen into the stoichiometric amorphous matrix could dramatically strengthen the structural stability of the barrier as well as increase the crystallization temperature from 450 to 600°C. This temperature increase resulted in retardation of the inward diffusion of Cu, resulting in delayed formation of copper- and tantalum-silicide. Amorphous-like phases were observed mainly for the high nitrogen flow rates (>30% N_2). For the temperature range of 450–650°C, no barrier failure occurred irrespective of the nitrogen flow rate. However, at 700°C, barrier failure occurred, and the extent of failure increased with increasing nitrogen flow rate. Annealing the Ag/TaN/Si samples at 700°C resulted in de-wetting of the silver on the surface of the tantalum nitride. Randomly distributed de-wetted holes instead of isolated islands as observed for Ag on Si or SiO_2 were present. Agglomeration of polycrystalline films is a result of minimization of the overall surface energy, interface energy, and grain boundary energy.

For the case of Ag metallization, Misra *et al*. [17] observed elemental Ta at the surface of Ag/TaON/Si samples after 400°C and 600°C anneals, indicating failure of the diffusion barrier and/or metal agglomeration or void formation. The authors reported that formation of voids in the Ag leads to exposure of the underlying TaON barrier layer and that this exposure explains the observation of surface Ta peaks on RBS spectra from the annealed samples. Agglomeration resulted in a discontinuous Ag layer and hence an increase in resistivity of the Ag films.

3.4.5 Conclusions

Tantalum nitride films were deposited on silicon substrates using different nitrogen flow rates. Increasing the partial nitrogen flow rate from 20 to 40% resulted in increasing nitrogen content in the films. Analysis of the films reveals that nitrogen flow rates of 15–20% result in TaN barrier layers with a mixture of different phases, with metal-rich Ta being the dominant phase. As nitrogen flow rate is increased further, the tantalum-nitride becomes disordered. Sheet resistance measurements, XRD, and RBS indicate that the TaN diffusion barriers are thermally stable up to 650°C for 30 minutes vacuum annealing, for all of the TaN film compositions [5]. No barrier failures such as could arise by Ta-silicide formation (by reaction of TaN with the underlying Si substrate) or by Ag interdiffusion, were detected at temperatures up to 650°C. Such high stability of the TaN barrier layer is desirable for potential application of Ag metallization for ULSI technology. In summary, increasing nitrogen flow ratios resulted in increasing electrical resistivity, changing of phase from Ta-rich to nitrogen-rich and crystalline to amorphous, decrease in grain size of the TaN films, and decrease in deposition rate. Barrier failure and de-wetting of Ag on TaN were observed after 700°C annealing.

3.5 References

[1] T. L. Alford, L. Chen and K. S. Gadre, Thin Solid Films 429, 248(2003).
[2] Y. C. Peng, C. R. Chen and L. J. Chen, J. Mater. Res. 13, 90(1998).
[3] C. Y. Hong, Y. C. Peng, L. J. Chen, W. Y. Hsieh and Y. F. Hsieh, J. Vac. Sci. Technol. A17, 1911(1999).
[4] M. A. Nicolet, Thin Solid Films 52, 415(1978).
[5] D. Adams, G. F. Malgas, N. D. Theodore, R. Gregory, H. C. Kim, E. Misra, T. L. Alford, J. W. Mayer. J. Vac. Sci. Technol. B 22(5), 2345(2004).
[6] S. P. Murarka, R. J. Gutman, A. E. Kaloyeros and W. A. Lanford, Thin Solid Films, 236, 257(1993).
[7] H. Miyazaki, K. Hinode, Y. Homma and K. Mukai, Jpn. J. Appl. Phys., 48, 329(1987).
[8] T. L. Alford, D. Adams, T. Laursen and B. M. Ullrich, Appl. Phys. Lett., 68, 3251(1996).
[9] D. Adams, T. Laursen, T. L. Alford, and J. W. Mayer. Thin Solid Films 308–309, 448(1997).
[10] N. Marecal, E. Quesnel, and Y. Pauleau, J. Electrochem. Soc., 141 (6), 1693(1994).
[11] T. Iijima, H. Ono, N. Ninomiya, Y. Ushiku, T. Hatanaka, A. Nishiyama and H. Iwai, Extended Abstracts Conf. On Solid State Devices and Materials, Makuhari, 1993.
[12] D. Adams, B. A. Julies, J. W. Mayer and T. L. Alford. Thin Solid Films 332, 235(1998).
[13] A. W. Czandema, J. Phys. Chem. 68, 2765(1964).
[14] T. E. Graedel, J. P. Franey, G. J. Gualltieri, G. W. Kammlott, D. L. Malm, Corros. Sci. 25, 1163(1985).
[15] T. L. Alford, J. Li, S. Q. Wang, J. W. Mayer (Eds.), Thin Solid Films 262, (1995).
[16] D. Jones, Principles, Prevention of Corrosion, Macmillan, New York, 523(1991).
[17] Joint Committee for Powder Diffraction Standard (JCPDS ICDD cards #: 25-1280, 26-0985, 32-1282, 25-1278, 14-0471, 31-1370, & 32-1283), PDF Database, 1994.
[18] G. S. Chen, and T. S. Chen, J. Appl. Phys. 87, 8473(2000).
[19] M. Stavrev, D. Fischer, C. Wenzel, K. Drescher and N. Mattern, Thin Solid Films 307, 79(1997).
[20] C. Chang, J. S. Jeng, and J. S. Chen, Thin Solid Films 413, 46(2002).
[21] E. Misra, Y. Wang, N. D. Theodore and T. L. Alford. Thin Solid Films 474, 235(2005).

4

Thermal Stability

4.1 Introduction

Silver has been investigated as a potential interconnection material for ultra large scale integration (ULSI) technology due to its lower bulk electrical resistivity (1.57 μΩ-cm at room temperature) when compared with other interconnection materials (Al 2.7 μΩ-cm and Cu 1.7 μΩ-cm)[1, 2] The lower resistivity can reduce the *RC* delays and high power consumption. Also, silver has higher electromigration resistance than aluminum and the same or even higher electromigration resistance than copper. However, Ag thin film agglomeration has been observed on many substrates at high temperatures and considered as a drawback of silver metallization.

Agglomeration results in the increase of electrical sheet resistance of thin films and eventually failure of films [3]. Hence, the thermal stability of Ag interconnects has been thought up to now as an issue of reliability of Ag metallization.

Agglomeration of thin films is a mass transport process that occurs at high temperatures. This process begins with grain boundary grooving and is followed by void, hillock, and island formation; all of which reduce the total energy of the system [3, 4]. Changes in surface morphology of thin films affect the electrical resistivity of thin films. Rough surfaces occurring at the initial stage of the agglomeration process provide more sources of scattering of conduction electrons through thin films and results in the increase of electrical resistivity [3]. Void and island formation occurs in the final stage of agglomeration and these formations cause the reduction of conduction area, which causes the abrupt increase of sheet resistance of silver thin films as the temperature increases. Also, Sieradzki *et al*. [5]

showed that the resistance changes of silver thin films on SiO_2 in the isothermal condition followed standard percolative disorder as a function of annealing time.

Currently, Cu is being used as the interconnect material in the Si-based system due to its low electrical resistivity. However, a diffusion barrier is needed because Cu diffuses easily into SiO_2 and Si even at low temperature (~200°C). Although silver thin film has poor thermal stability on the SiO_2 layer due to agglomeration, Ag is an ideal candidate for future interconnects if agglomeration and diffusion are avoided during processing and operation. Ag acceptance would also be enhanced if it did not require the use of any diffusion barrier and its resistivity value could remain lower than that of Cu.

4.2 Silver-Aluminum Films

4.2.1 Introduction

The use of Ag(Al) thin films is a method to prevent agglomeration of Ag on SiO_2 at high temperatures. Pure Ag and Ag(Al) thin films were deposited on thermally grown SiO_2 using electron-beam evaporation. Typical base pressure and operation pressure were 5×10^{-7} and 4×10^{-6} Torr, respectively. To obtain the Ag(Al) thin film, which is a Ag thin film containing a small amount of Al, a Ag–Al alloy for electron-beam evaporation was prepared by mixing pure Ag slug with pure Al slug targets [Ag(Al)-I: 90 at.% Ag–10 at.% Al, Ag(Al)-II: 95 at.% Ag–5 at.% Al]. After completely melting of the Ag–Al target by electron-beam heating in the evaporator, Ag(Al) thin films were deposited onto substrates. Due to the thickness dependence on agglomeration of silver thin films, both Ag and Ag(Al) thin films were deposited with the same thickness. Thermal anneals in vacuum ($\sim5\times10^{-8}$ Torr) were performed for 1 hour in order to investigate the thermal stability of Ag and Ag(Al) thin films on SiO_2 substrates.

The thermal stability of these thin films was characterized by Rutherford backscattering spectrometry (RBS), X-ray diffractometry (XRD), and in-line four-point-probe analysis. In addition, optical microscopy was used to observe the evolutions of void and island formations caused by the agglomeration process of Ag and Ag(Al) thin films.

4.2.2 Results

Figure 4.1 shows the typical RBS spectra for as-deposited Ag, as-deposited Ag(Al)-I, annealed Ag at 600°C for 1 hour in vacuum, and annealed Ag(Al)-I at 600°C for 1 hour in vacuum on oxidized silicon. The thickness of these films is approximately 95 nm. In the Ag peak indicated in Figure 4.1, the intensity of the Ag peak in pure as deposited Ag thin film is slightly higher than that of as-deposited and annealed Ag(Al)-I thin film. This is because the density of the Ag(Al)-I thin film is reduced by adding Al. The result of RUMP simulation reveals

that the Ag(Al)-I thin films contain 5.4 at.% of Al and Ag(Al)-II thin films contain 3.1 at.% of Al. Approximately 3 at.% of oxygen is incorporated in all samples during the evaporation process. The RBS spectrum of the Ag thin film annealed at 600°C shows agglomeration on the SiO_2 substrate. Alford *et al.* [4] showed the typical shape of the RBS spectrum for agglomeration of thin films; the intensity of the Ag peak is reduced and the sloping back edge of the Ag peak is produced. The number of counts for backscattered ions from the agglomerated Ag thin film is decreased as a result of the reduction of area of Ag on the substrate.

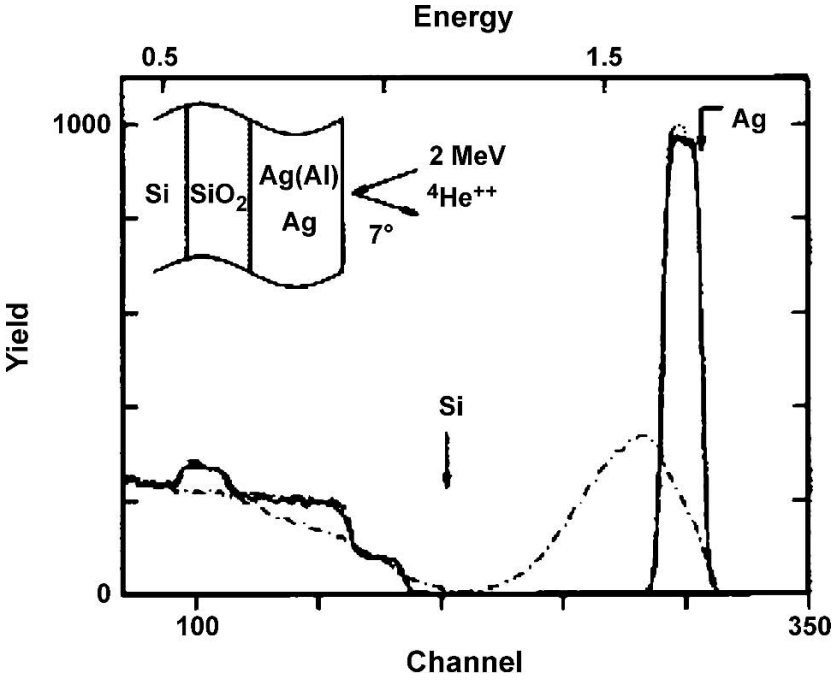

Figure 4.1. RBS spectra of Ag(Al)-I and Ag thin films on SiO_2 substrate: as-deposited Ag(·····), as-deposited Ag(Al)-I(——), Ag annealed at 600°C for 1 hour in vacuum (— · — · -), and Ag(Al)-I annealed at 600°C for 1 hour in vacuum (— — —) [6].

In addition, the Si peak is detected at the surface of the sample due to the exposure of the SiO_2 substrate caused by the formation of voids. In contrast to the thermal stability of the Ag thin films on SiO_2, the Ag(Al) thin film has good thermal stability at 600°C for 1 hour in vacuum. No interdiffusion between Ag(Al) and SiO_2 exists. No agglomeration of Ag(Al) thin films occurs up to 600°C. X-ray diffraction spectra of Ag(Al)-II thin films annealed at different temperatures are shown in Figure 4.2. The peaks present in Figure 4.2 are all identified as Ag and are stable up to 600°C for 1 hour in vacuum. There is no indication of the formation of a Ag–Al compound and no change of lattice parameter of Ag as anneal temperature is increased. Compared to the as-deposited Ag(Al) thin film, the annealed Ag(Al) thin film has higher intensity and sharper peaks.

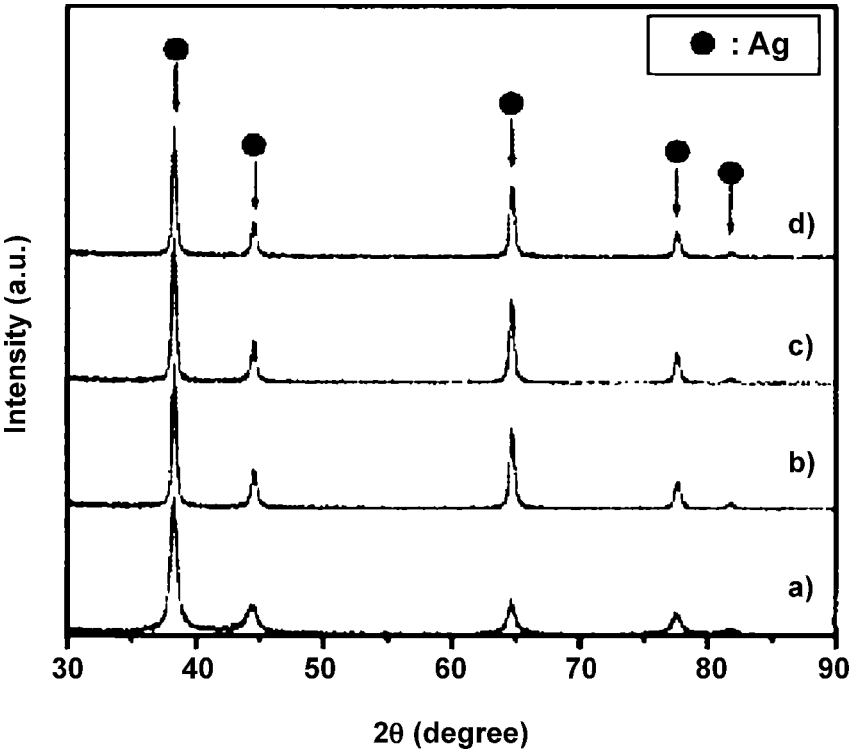

Figure 4.2. XRD patterns of Ag(Al)-I thin films on SiO_2 substrates: (a) as-deposited and annealed in vacuum for 1 hour at (b) 400°C, (c) 500°C, and (d) 600°C. Glancing angle geometry (1° tilting) was used [6].

It is suggested that the crystallization of films is enhanced and grain size is increased when Ag(Al) thin film is annealed. For pure Ag thin films, it is found that agglomeration begins from the sample annealed at 400°C in vacuum for 1 hour although the fraction of voids is small. The Ag thin film annealed at 600°C for 1 hour in vacuum, agglomerates completely resulting in Ag islands. However, Ag(Al) thin films do not have any surface changes in morphology at various anneal temperatures.

4.2.3 Discussion and Conclusions

The resistivity changes of pure Ag, Ag(Al)-I, and Ag(Al)-II as a function of different anneal temperatures are shown in Figure 4.3. For as-deposited thin films, the resistivity of pure Ag thin film is the lowest. Resistivity of thin films is increased as the amount of Al is increased because Al atoms enhance the impurity scattering factor of conduction electrons.

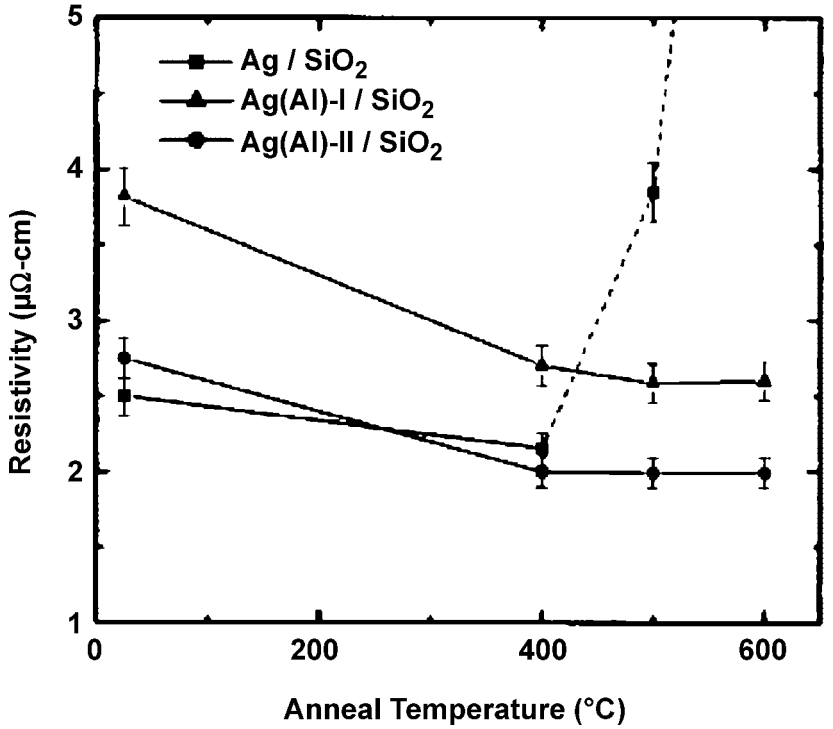

Figure 4.3. Electrical resistivity of Ag, Ag(Al)-I, and Ag(Al)-II thin films on SiO_2 substrates annealed at various temperatures in vacuum for 1 hour [6]

The relatively higher resistivity value of Ag thin film made in this study when compared to bulk silver resulted from more surface scattering due to its thickness and the incorporation of a small amount of oxygen during the thin film process. For the Ag(Al) thin films, the resistivity of samples annealed at 400°C for 1 hour in vacuum is decreased from the value of as-deposited samples. It is thought that the enhancement of crystallization and grain growth of thin film obtained by the X-ray diffraction analysis shown in Figure 4.2 contribute to the decrease of resistivity. The resistivity of both Ag(Al)-I and Ag(Al)-II thin films is constant after annealing at 400°C. The difference of absolute value of resistivity between two different Ag(Al) thin films has also remained constant. This means that the Ag(Al) on SiO_2 is a thermally stable solid solution as confirmed by RBS, XRD, and optical microscopy. For pure Ag thin films, the resistivity of the sample annealed at 400°C for 1 hour in vacuum is decreased slightly due to the crystallization and grain growth although agglomeration is started.

However, resistivity is increased abruptly from 500°C. The Ag thin film on SiO_2 annealed at 600°C for 1 hour in vacuum has infinite resistivity since the scattering effect of conduction electrons is increased. The conduction path is reduced and lost eventually. This fact is consistent with RBS, microstructure analysis explained above. The interesting fact is that the resistivity of Ag(Al)-II thin films annealed at 400°C is lower than that of pure Ag thin film annealed at the

same temperature. The finding is a direct result of the good thermal stability of Ag(Al) thin films on the SiO_2 layer. The thermal stability of Ag thin films on SiO_2 substrates is enhanced by the addition of aluminum atoms to pure silver [6]. Though the bulk resistivity of Ag is the lowest at room temperature, agglomeration of silver thin films at higher temperatures has been considered as one of the obstacles for its use as the interconnect material of electronic devices. The Ag(Al)-II thin films investigated in this study have comparable resistivity value with pure Ag thin film at room temperature and maintained lower resistivity than Ag thin film from 400°C without any diffusion barrier on SiO_2.

Also, agglomeration does not occur in Ag(Al) thin film up to 600°C on SiO_2 . Compared with Cu thin film used as interconnect material, Ag(Al) thin film does not need diffusion barriers to prevent any diffusion through the SiO_2 layer and agglomeration. It also has a lower resistivity value, which can reduce RC delay, faster than Cu thin film. These findings can impact metallization of thin film transistors using low temperature processes, flexible electronics using polymers, as well as the development of high speed electronic devices.

4.3 Silver Deposited on Paralene-*n* by Oxygen Plasma Treatment

4.3.1 Introduction

As the features size in modern high density multilevel metallization shrinks, concerns such as RC delays, high power consumption, and cross talk noise have to be addressed. One of the solutions for this is to integrate less resistive metal with low dielectric constant materials. Besides having low dielectric constant, the materials must have a good adhesion to silicon and to interconnect materials and thermal stability.

Thermal stability is important to device characteristics and reliability. The maximum temperature is not set by dielectric deposition process but by other process requirements such as soldering or annealing. The material is expected to withstand thermal cycling during annealing as well as occasional temperature shocks.

Polyimides as low dielectric constant material (dielectric constant 3.5–4) have been studied. Another class of polymers, parylenes, with even lower dielectric constant has been proposed for this work. For low resistivity interconnect materials, copper is being considered as a good candidate. However, copper diffuses very fast in different materials. Hence, the lower resistivity and relatively noble metal, silver, is considered here. Gadre and Alford [7] investigated Parylene-*n* (Pa-*n*) and silver for ultra large scale integrated circuits because of their favorable properties. These include low dielectric constant (2.65), negligible water take-up, chemical inertness, low temperature deposition, as well as compatibility with current integrated circuit manufacturing and low resistivity (1.6 μΩ-cm), high electromigration resistance for silver.

To meet the integration requirements, Pa-*n* and Ag are studied for critical reliability issues. Diffusion of Ag in Pa-*n* was investigated by a series of

experiments using Rutherford backscattering spectrometry (RBS), secondary ion mass spectroscopy (SIMS), and X-ray diffraction (XRD) analysis. Variation of resistivity of silver with temperature was measured using four-point-probe analysis. Also, adhesion issues of Ag with Pa-*n* were studied using scratch and tape test methods. Oxygen plasma induced surface modification shows drastic improvements in adhesion of Ag with Pa-*n* without sacrificing any electrical or diffusion properties [7].

4.3.2 Experimental Details

Parylene-*n* (Pa-*n*) films were deposited on Si substrate by chemical vapor deposition technique. The films were deposited at Paratech Inc. The measured thickness of the films by optical technique was about 1 mm. All the samples selected for the experiment were deposited at one time with the same deposition parameters. Before processing, the above obtained films were cleaned with acetone, de-ionized water, and dried in dry nitrogen gas.

Silver was deposited on Pa-*n* by electron beam evaporation technique. Operating pressure during evaporation was maintained at 3×10^{-6} Torr. The actual pressure during evaporation was 4.5×10^{-6} Torr. The expected thickness of Ag was 200 nm.

All of the samples were annealed in a tube furnace at different temperatures ranging from 100 to 375°C. All anneals were done for 30 minutes under vacuum in a carrousel furnace. The base pressure was 5×10^{-8} Torr and actual pressure during annealing was approximately 4×10^{-7} Torr. After the anneal was completed the samples were cooled in a load chamber for 15 minutes before being removed completely from the furnace to avoid sudden decrease in temperature. X-ray diffraction analysis was performed for structural characterization of Ag films in a Philips X'Pert multipurpose diffractometer (MPD) diffractometer using conventional $\theta/2\theta$ geometry. Cu*K*-α radiation source with an operational voltage of 45 kV and a filament current of 40 mA was used.

X-ray diffraction of Pa-*n* samples in as-deposited and annealed conditions was also performed to determine the crystallinity and any phase change.

Conventional RBS measurements with a 3.7 MeV He^{+2} ion beam, 7° incident angle, and 172° scattering angle were primarily used for analyzing silver and dielectric interaction and thickness measurements. The beam energy of 3.7 MeV was selected for enhancing the carbon signal [8] from Pa-*n*.

SIMS was performed for as deposited and annealed samples of Ag/Pa-*n* system. Camera IMS3*f* SIMS was used to perform depth profiling. The crater depth was measured on a DekTek profilometer. Ag was removed from the Pa-*n* using nitric acid. The samples were immersed in 50% nitric acid (50%HNO_3+50%H_2O by volume) for 30 s to remove silver film completely. The silver stripped Pa-*n* samples were coated with gold to avoid strong charging.

Four-point-probe technique was used for sheet resistance measurements. The sheet resistance was measured on both Ag/Pa-*n* as deposited as well as annealed samples. *In situ* resistivity measurements were done for the Ag/Pa-*n* sample during thermal annealing. The continuous sheet resistance and temperature measurements were recorded using a computer program. The ramp rate was 20°C/min and

samples were heated in a vacuum. The samples were cooled from 375 to 200°C in the same furnace and resistivity measurements were again recorded.

Adhesion analysis Ag/Pa-*n* and Pa-*n*/Si was done using scratch [9] and tape tests. It consisted of a fixed load applied per test run. The load was increased in 1.1 g increments until the film completely detached from the surface. The stylus made of 20-mm-diameter diamond tip was drawn over the surface.

The scratches were analyzed using optical and scanning electron microscopes. Tape test was used as a preliminary adhesion test to screen out poorly adhering films before proceeding with system optimization. The 180° tape test prescribed by the American Society for Testing and Material's designation D3359-95a [10] was performed with Ag/Pa-*n* films. A pressure sensitive tape (Permecel 99) with minimum adhesional strength of 45 g/mm was applied over a grid of lines manually made by a diamond tip scriber. To enhance adhesion between Ag and Pa-*n*, surface modification of Pa-*n* was performed using an oxygen plasma. Parylene-*n* was exposed to an oxygen plasma of 50 W plasma for 60 seconds. The exposed surfaces were analyzed using atomic force microscopy (AFM) and compared to the as-deposited sample. Ag is then deposited on Pa-*n* in a similar way explained above. Some samples were also annealed. RBS and four-point-probe analysis of the plasma treated surface were performed to check any diffusion or change in electrical properties of silver due to plasma exposure.

4.3.3 Results

4.3.3.1 Phase Change in Pa-n upon Annealing

Figure 4.4 shows the XRD data of Pa-*n* film deposited on Si substrate. It was clearly observed that the as-deposited sample shows a peak at 2θ equal to 16.6°. This peak corresponds to α phase of Pa-*n*. The peak completely vanishes at and above 250°C and a new peak at 20° is formed. This peak corresponds to β phase of Pa-*n*. This is confirmed with other researchers showing the phase transition of Parylene-*n*. Literature reveals the phase transformation temperature of Pa-*n* as 230°C. The α-Pa-*n* is a stable phase below 230°C and completely transformed to β-Pa-*n*, which is irreversible and stable after cooling down to room temperature Increase in intensity of the β-Pa-*n* indicates an increase in the crystallinity of the Pa-*n* as it is annealed at higher temperatures.

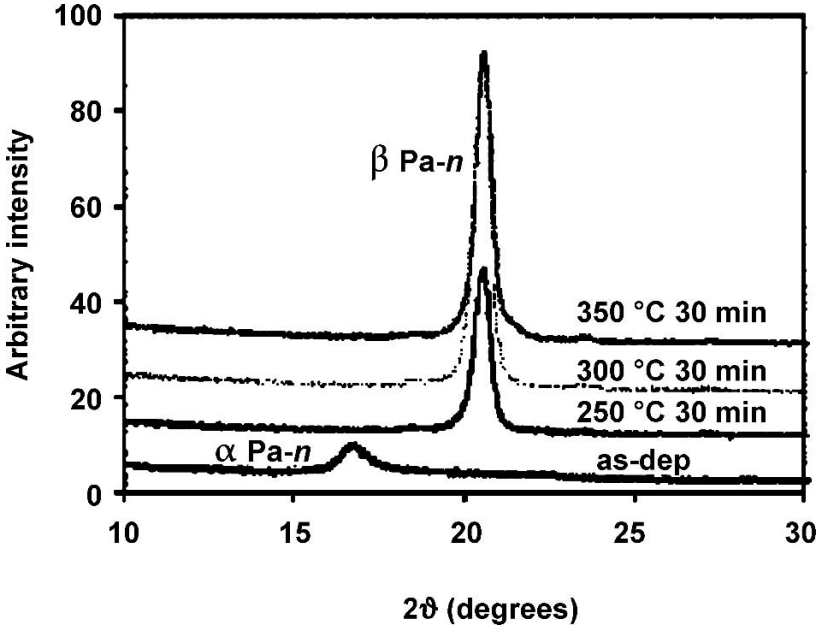

Figure 4.4. X-ray diffraction patterns (under θ/2θ scan geometry) of Pa-*n* at different anneal temperatures. The figure clearly shows phase change in Pa-*n*. The peak corresponding to α Pa-*n* vanishes at 250°C and the new peak of β Pa-*n* is observed [7].

4.3.3.2 Compositional Changes of Ag on Pa-n upon Annealing

The silver film thickness obtained from RBS was approximately180 nm and for Pa-*n* it was 0.8 mm. Experiments showed no significant changes in Ag films upon annealing. Figure 4.5 shows a comparison of the as-deposited and annealed Ag films on Pa-*n*. Energy of 3.7 MeV was used for RBS analysis and corresponds to the resonance energy for nitrogen [8]. It also enhances carbon and oxygen signals in the spectra and hence was used to clearly distinguish carbon signal from Pa-*n*. Literature shows that silver diffuses in Pa-*n* above 350°C for 30 minute anneals. Our data suggest no RBS detectable diffusion of Ag in Pa-*n* even at 375°C and 1 hour anneals.

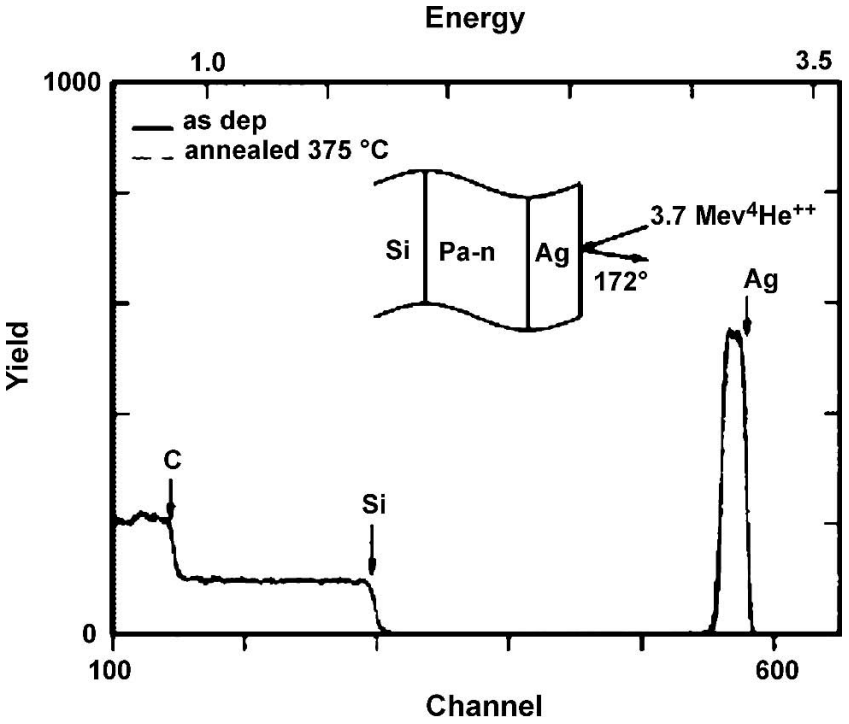

Figure 4.5. Typical RBS spectra of as-deposited and 375°C annealed Ag/Pa-*n* films. Both spectra show no diffusion of Ag when deposited on Pa-*n* [7].

4.3.3.3 Sheet Resistance Variation upon Annealing

In situ four-point-probe measurements of Ag on Pa-*n* were performed as explained in the previous section. The obtained sheet resistance, values of Ag was converted to resistivity by using thickness values obtained from RBS. The plot of resistivity as a function of temperature is shown in Figure 4.6. Also, ramp up and cool down data are plotted in the same graph. As both cool down and ramp up observations follow the same line, it can be said that there is no drastic change in the silver film deposited on the Pa-*n*. This analysis shows resistivity changes linearly with temperature. The *ex situ* analysis of resistivity of Ag on Pa-*n* is shown in Table 4.1. The variation of resistivity can be best explained with XRD analysis mentioned below.

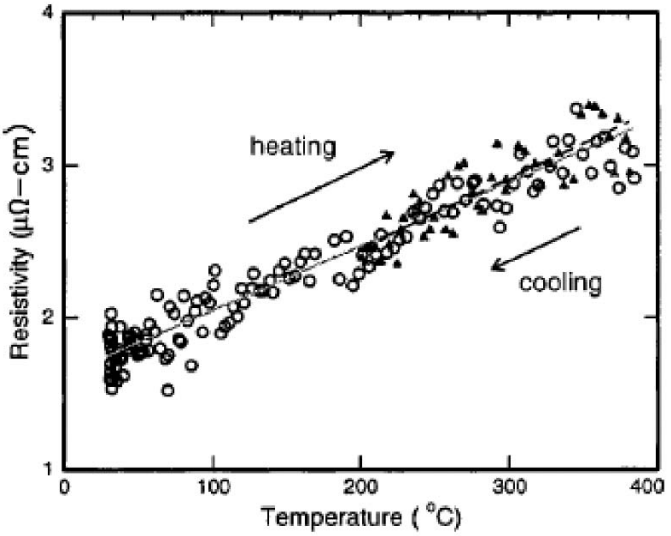

Figure 4.6. *In situ* analysis of resistivity variation of Ag on Pa-*n* with temperature by four-point-probe measurements. The resistivity follows linear relationship with temperature. (o-heating, Δ-cooling, — represents linear fit while heating and - - - - - represents linear fit while cooling down) [7].

Table 4.1. Resistivity of Ag/Pa-*n* with annealing temperature [7]

Sample	As-deposited	100°C	250°C	300°C	350°C
R μΩ-cm	2.73	2.55	1.95	1.87	3.48

Figure 4.7 shows X-ray diffraction pattern of Ag on Pa-*n*. Ag film shows prominent (111) peak. The intensity of (111) peak increases up to 300°C and then suddenly decreases for 350°C. X-ray diffraction does not reveal any phase formation of Ag with Pa-*n* even at elevated temperatures. Annealing above 400°C decomposes Pa-*n* films.

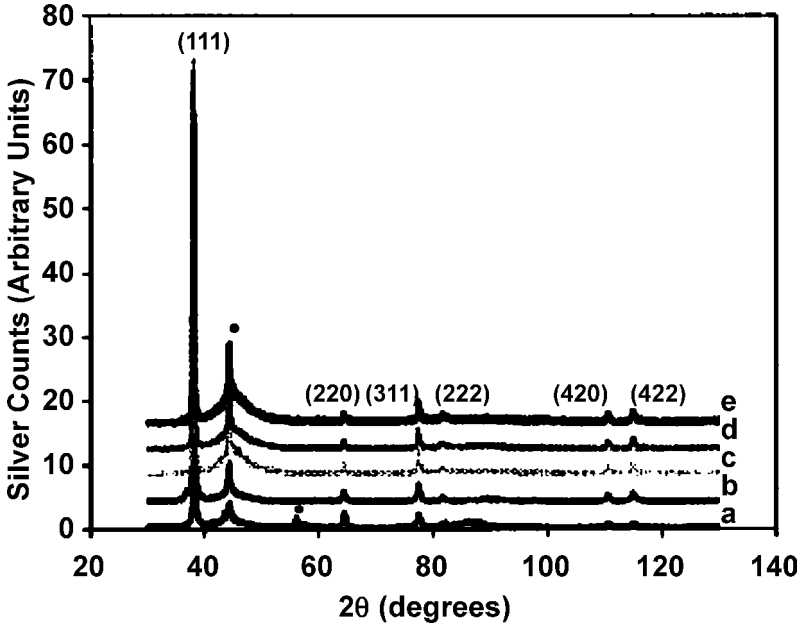

Figure 4.7. XRD diffraction patterns (under θ/2θ scan geometry) of Ag/Pa-*n* at different anneal temperatures [7]

4.3.3.4 Adhesion Analysis

Table 4.2 shows total load in grams required to remove film of Pa-*n* from the Si substrate completely after performing the scratch test. It was observed that load decreases with increasing annealing temperature suggesting deterioration of adhesion of Pa-*n* with Si substrate. Table 4.2 also shows that the load required for removing Ag film completely from Pa-*n* increases with increasing annealing temperature. This indicates stronger adherence of Ag with Pa-*n* at elevated temperatures. To support the results from the scratch test, results from the adhesion tape test were examined. If more than 25% of the total tested film was removed, then the sample was considered to be ''failed'' in the adhesion test.

Table 4.2. Scratch test results of failure load in grams [7]

Sample	As-deposited	250°C	300°C	350°C
Pa-*n*/Si	8.0	6.9	5.5	4.5
Ag/Pa-*n*/Si	4.4	4.4	5.5	5.5

Table 4.3 shows the results of the tape test for different conditions. The as-deposited Ag film on Pa-*n* shows the removal of more than 90% of the film, indicating very poor adhesion. The annealing above 250°C improves the test results significantly. Though annealing increases the adhesion of silver to parylene to some extent, surface modification of parylene even shows better results. AFM was used to compare the as-deposited and plasma-treated parylene surfaces at an atomic scale. Oxygen plasma induces damage to the parylene surface and hence increases its roughness. The rough films are believed to increase mechanical interlocking between top silver and bottom parylene film, thereby increasing the adhesion significantly. Tape test after surface modification shows that adhesion between Ag and Pa-*n* is even stronger than Pa-*n* and Si substrate. Four-point-probe and RBS analysis performed on the above samples show no drastic difference as compared to untreated samples.

Table 4.3. Tape test results for Ag/Pa-*n*. If more than 25% of total film was removed, then the sample considered to be failed [7]

Sample	Treatment	Tape test criteria	Remarks
Ag/Pa-*n*	As-deposited	Fail	90% silver film removed
Ag/Pa-*n*	250°C	Pass	20% silver film removed
Ag/Pa-*n*	300°C	Pass	10% silver film removed
Ag/Pa-*n*	350°C	Pass	<2% silver film removed
Ag/Pa-*n*	375°C	Pass	<2% silver film removed

4.3.4 Discussion

Results of the above experiments indicate very little tendency of silver to diffuse in parylene. Secondary ion mass spectroscopy reveals an insignificant amount of silver in parylene at 375°C. It was assumed here that diffusion takes place according to Fick's law. The plot of natural log of concentration of silver against square of depth was used to find the diffusion coefficient of silver. The slope of the graph was equated to $1/4Dt$, where D is diffusion coefficient and t is time in seconds. For silver sample annealed at 375°C for 30 minutes, calculated diffusion coefficient was $1.47\times10^{-14}\pm3\%$ cm^2/s. This calculated diffusion coefficient is smaller than previously recorded values. The value is also approximately equal to the as-deposited silver on parylene, suggesting that silver concentration in the

parylene remains constant during annealing. This insignificant silver diffusion in parylene can be explained as follows.

During annealing, Pa-*n* changes from α Pa-*n*, which has monoclinic crystal structure to β Pa-*n*, which is trigonal. During this transformation, crystallinity of parylene increases. This was shown by XRD in Figure 4.4. Typical parylene is only 57% crystalline and the remainder is amorphous. Though its crystallinity increases with annealing it never reaches 100% crystallization. The amorphous region in parylene may be present between the crystalline structure. The whole surface can be considered as long crystalline chains linked together with amorphous regions forming a closed structure. This closed structure is believed to prohibit diffusion of silver in Pa-*n*. Some researchers have shown a web-like structure at the interface of Pa-*n* and Cu, increasing Cu diffusion drastically. No such web structure was observed at the Pa-*n* and Ag interface when examined at high magnification using scanning electron microscopy. An experiment was conducted to examine the effect of phase change of Pa-*n* on silver diffusion. Pa-*n* was preheated to 250°C for 30 minutes to allow complete phase transformation from α-phase to β-phase and then cooled down. The α to β transformation is irreversible. β Pa-*n* is more crystalline as compared to α Pa-*n* and hence it was more open. Ag is deposited at room temperature on the pre-annealed sample and then the system is again annealed at 375°C for 30 minutes in vacuum. SIMS analysis on annealed sample does not reveal any diffusion of silver in Pa-*n*. This shows that phase change of Pa-*n* does enhance diffusion of silver. The atomic size is another effective factor for silver atom. Diffusion is recorded for copper and aluminum before in Pa-*n*. Copper and aluminum atom sizes are 0.135 and 0.126 nm, respectively. These are smaller as compared to silver atom, which has a covalent radius of 0.152 nm. Thus it requires more space to pass through Pa-*n* structure underneath it. Silver has a melting point of 962°C, which is not enough to thermally excite silver atoms at 375°C to go under diffusion.

Thermal stability of silver is explained using the four-point-probe technique. It was observed during *in situ* resistivity variation with temperature that the cool down curve exactly follows the ramp up curve. This rules out any formation of voids in silver film while annealing. This suggests that silver film maintained its continuity up to 375°C during annealing. Also, the mechanical and thermal strains produced during deposition and annealing are not significant enough to cause any discontinuity in silver or parylene films. Adhesion is very important in determining durability of thin film devices. Here qualitative study of adhesion of Pa-*n* with silicon substrate as well as top silver layer was presented. Si wafers were cleaned in HF solution before depositing Pa-*n* on it by vapor deposition at Paratech Inc.

The adhesion was examined using the scratch test. It was observed that adhesion between Pa-*n* and Si substrate deteriorates with annealing. Pa-*n* is a chemically inert polymer and it does not form any chemical bond with Si substrate. This indicates inherent adhesion of Pa-*n* with Si is poor. In the absence of any adhesion promoter and surface treatment, two smooth surfaces result in weak adhesion. The possibility of small silicon dioxide at the interface between Pa-*n* and Si and defects may cause a reduction in adhesion. Formation of chemical bonds is an important way to achieve interfacial adhesion. For silver and the Pa-*n* system there does not exist any chemical interactions, such as second phase formation or

intermixing with each other, resulting in weak adhesion. This was confirmed by X-ray diffraction and SIMS results. Small dipole–dipole interaction between the two though cannot be neglected. However, the tape test shows improved adhesion between silver and parylene with annealing. The reason for this is not fully understood at this time. Future study will be required to understand this behavior. Although annealing increases the adhesion, it is not enough for reliable device operation. One way to improve the adhesion is by surface treatment of Pa-*n*. Oxygen plasma was used to treat the Pa-*n* surface. Plasma treated Pa-*n* showed evidence of increased roughness. The plasma treated samples were analyzed using the tape test for adhesion. It was observed that adhesion between Ag and Pa-*n* is stronger than even Pa-*n* and Si substrate. The tape test shows complete removal of Ag/Pa-*n* together from Si substrate. Due to increased roughness, contact area between Ag and Pa-*n* was increased, improving adhesion tremendously. Care should be taken while doing plasma treatment, as excess power or long time exposure can etch Pa-*n* completely. Formation of single and double bonds between carbon and oxygen [11] during plasma treatment may have helped increase adhesion between Ag and Pa-*n*.

4.3.5 Conclusions

The thermal stability of Pa-*n* as interlayer low dielectric material and silver as low resistivity metal was studied. No interaction or phase formation between Ag and Pa-*n* was observed. Resistivity analysis by four-point-probe shows the structure to be electrically stable even at high annealing temperatures (~375°C). Phase change of Pa-*n* while annealing does not affect diffusion properties of Ag in Pa-*n*. SIMS gave a diffusion coefficient of $1.47\times10^{-14}\pm3\%$ cm^2/s for as-deposited as well as annealed samples, indicating negligible diffusion of silver in Pa-*n*. Although adhesion between Ag and Pa-*n* is poor, it is shown that drastic improvement can be obtained by surface treatment of Pa-*n* with oxygen plasma without sacrificing thermal and electrical stability of the system [7].

4.4 Effects of Different Annealing Ambients on Silver-Aluminum Bilayers

4.4.1 Introduction

In a study of the formation of a surface protection layer for Ag from a Ag/Al bilayer structure, Wang *et al.* [12] reported that high temperatures increased the transport of Al through the Ag layer and the reaction of Al with NH_3 or O_2 on the surface. That work centers on the mechanism governing the outdiffusion of Al through the Ag. Many researchers have investigated the phenomenon of hillock growth during annealing. Similarly, the phenomena of hole growth and agglomeration have been observed by several workers for thin films annealed under varying conditions of treatment.

In a study of the dependence of silver agglomeration on ambient annealing conditions, it was found that no agglomeration occurred in samples annealed in an ambient containing oxygen or water. However, significant agglomeration of silver films on SiO_2 occurred when annealed in air. It has been concluded from this study that the agglomeration is caused by the absorption of Cl from the air, and that this absorption can be prevented by passivating the surface with a Ti-oxide layer. This was accomplished by annealing a $Ag/Ti/SiO_2$ structure in an oxygen ambient. Upon annealing, Ti segregates to the surface to form a thin Ti-oxide surface layer and some of the Ti reacts with the underlying SiO_2 substrate to improve the adhesion of Ag to the dielectric.

4.4.2 Experimental Details

Aluminum (Al) and silver (Ag) films were sequentially deposited on thermally oxidized silicon (Si) wafers by electron-beam evaporation to form Ag(200 nm)/Al(8 nm) bilayer structures. The base pressure of the chamber before deposition was $\sim 10^{-7}$ Torr. During deposition, the operating pressure was $\sim 10^{-6}$ Torr. Samples were then annealed in a Lindberg single-zone quartz-tube furnace for 30 minutes at temperatures ranging from 300°C–700°C in three different ambients. The ambients were argon (Ar), helium–hydrogen (He–H), and electronic grade (99.99%, with $H_2O<33$ and $O_2+Ar<10$ molar ppm) ammonia (NH_3). Prior to annealing the samples, the furnace was pumped down and purged at least three times with the respective gases. A gas flow rate of ~2 1/min was maintained during anneals.

Rutherford backscattering spectrometry (RBS) using a 3.0 or 3.7 MeV He^{+2} beam at 7° tilt and total accumulated charge of 10 μC was used to determine the composition and thickness of the samples. Auger electron spectroscopy (AES) analyses of the Ag/Al structures were carried out by using a Perkin–Elmer PHI 600 scanning Auger system using a primary beam energy of 5 keV and current of 50 nA. The depth profiles were acquired by sputtering with 3.5 keV Ar ions. The ion beam was rastered over a 2 mm^2 area. A JEOL-JSM 840 scanning electron microscope operated at 5–15 kV and in secondary mode was used to evaluate the surface morphology of the samples. The RUMP computer simulation program was used to analyze the RBS spectra. Sheet resistance was obtained with the van der Pauw four-point-probe and the resistivity was determined from the sheet resistance and the film thickness.

4.4.3 Results

4.4.3.1 Aluminum Transport in Silver Films

1. Argon Ambient

Figure 4.8 compares the 3.0 MeV RBS spectrum of the as-deposited Ag(200 nm)/Al(8 nm) bilayer with that annealed at three different temperatures for 30 minutes in a flowing Ar ambient.

When the samples are annealed at 400°C and higher temperatures, Al segregates to the free surface and reacts with residual oxygen to form a thin aluminum-oxide layer, as indicated by the presence of the surface Al peak (labeled ''surface Al'') and surface O peak (labeled ''surface O''). The shift in the Ag signal to lower energies is due to this surface layer. Due to the small mass separation, the Al and Si signals overlap. However, the peak labeled ''interfacial Al'' indicates the presence of Al at the interface. The RUMP simulation was used to simulate the RBS spectra. The simulation shows that the surface aluminum oxide layer is

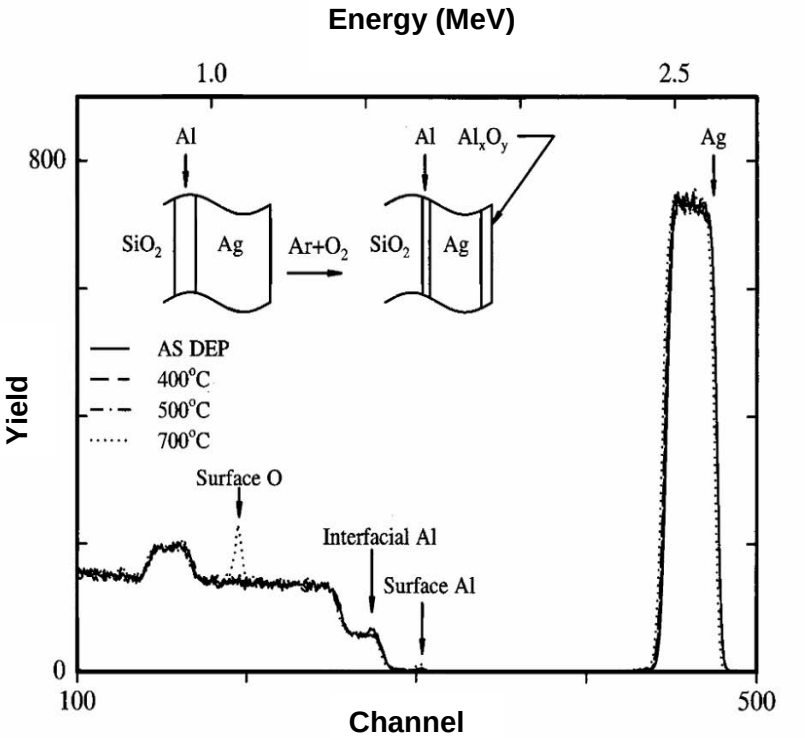

Figure 4.8. RBS spectra (3 MeV He^{+2}, 7° tilt) obtained from a Ag(200 nm)/Al(8 nm) bilayer on a SiO_2 structure annealed in Ar at three different temperatures for 30 minutes [16]

about 13 nm thick for the sample annealed at 700°C and that the thickness of the Ag layer is ~180 nm thick. Figure 4.9 gives the RBS spectra of the surface Al peaks only. It is evident that the amount of Al at the surface increases with annealing temperature, with the largest amount corresponding to the 700°C anneal. The spectra further show that the background yields for the annealed samples is higher than the backscattered yield of the as-deposited sample. This higher yield (channel 295–298) is due to the residual Al in the Ag film. According to the RUMP simulation, the residual Al concentration is ~1 at.% at 700°C.

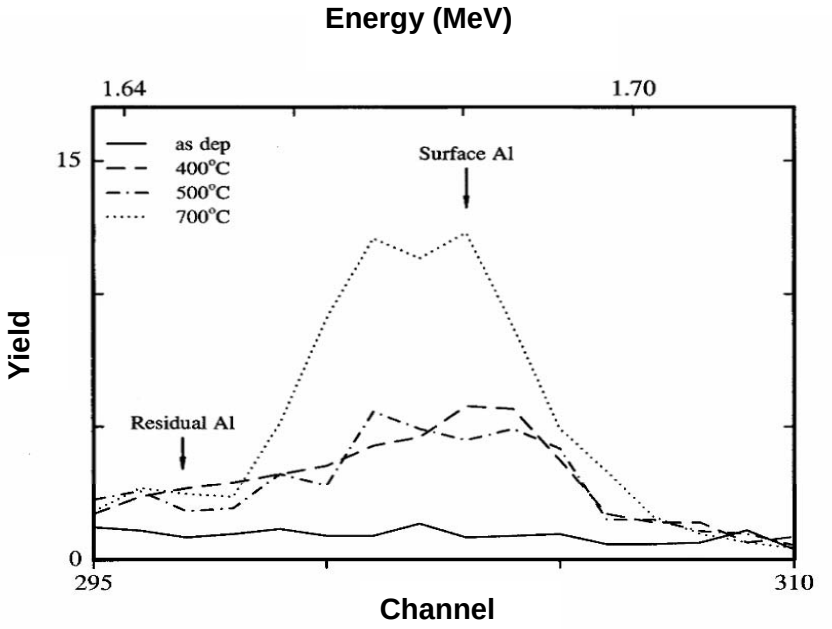

Figure 4.9. RBS spectra (3 MeV He^{+2}, 7° tilt) of the diffusion barriers before and after being annealed in flowing Ar for 30 minutes at three different temperatures [16]

Elemental distribution and depth profiling were obtained from AES analyses, Figure 4.10. Figure 4.10(a) shows the depth profile of the as-deposited sample for the interfacial region only. It clearly shows the Al at the interface. The presence of the oxygen and aluminum signals near the surface region for temperatures greater than 400°C confirms the outdiffusion of Al to the surface and the subsequent formation of a thin aluminum oxide (Figures 6.10(b) and 6.10(c)). Within the detection limits of AES, no accumulation of Al in the Ag or unreacted interfacial aluminum could be detected for temperatures ≥400°C.

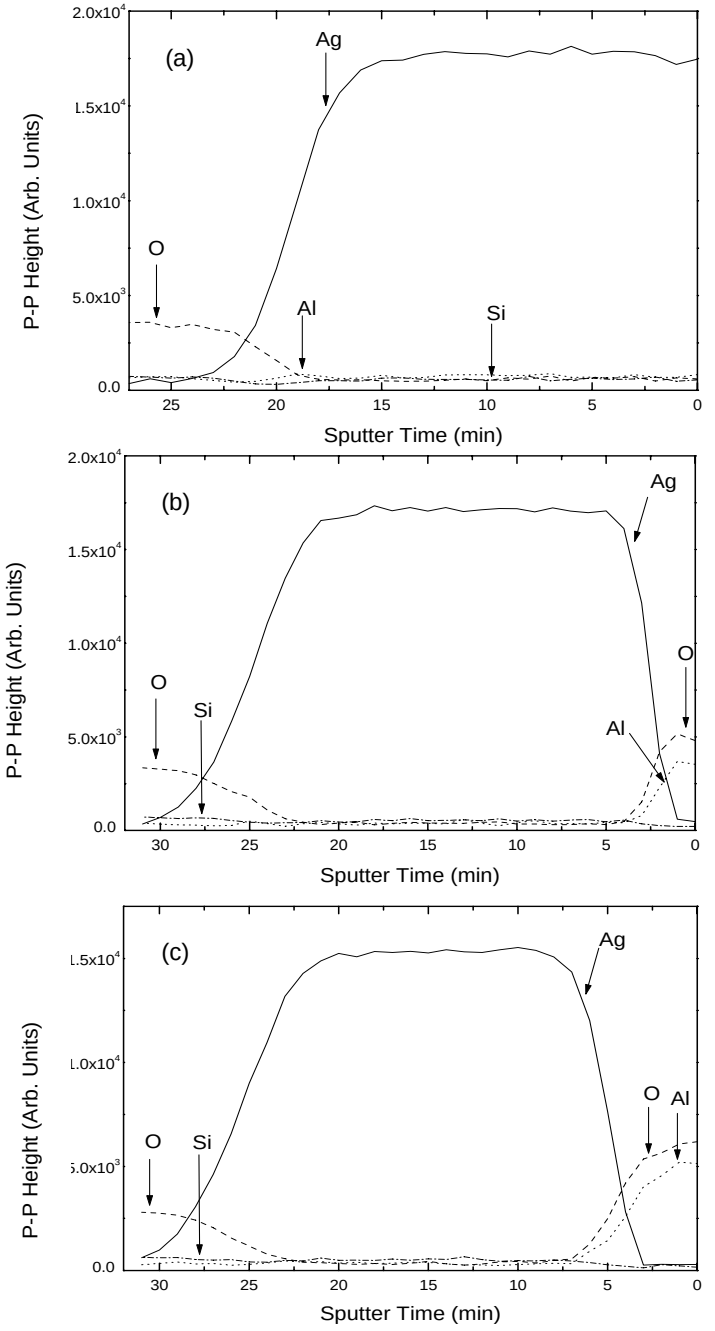

Figure 4.10. Auger depth profiles of a Ag (200 nm)/Al (8 nm) bilayer on SiO_2 (a) as-deposited, (b) 400°C, (c) 700°C for 30 minutes, annealed in Ar [16]

2. Helium-Hydrogen Ambient

Annealing the Ag/Al structure in a flowing He–H ambient at temperatures between 400°C–700°C also resulted in the segregation of Al to the surface and the subsequent formation of a thin aluminum oxide at the surface (Figure 4.11).

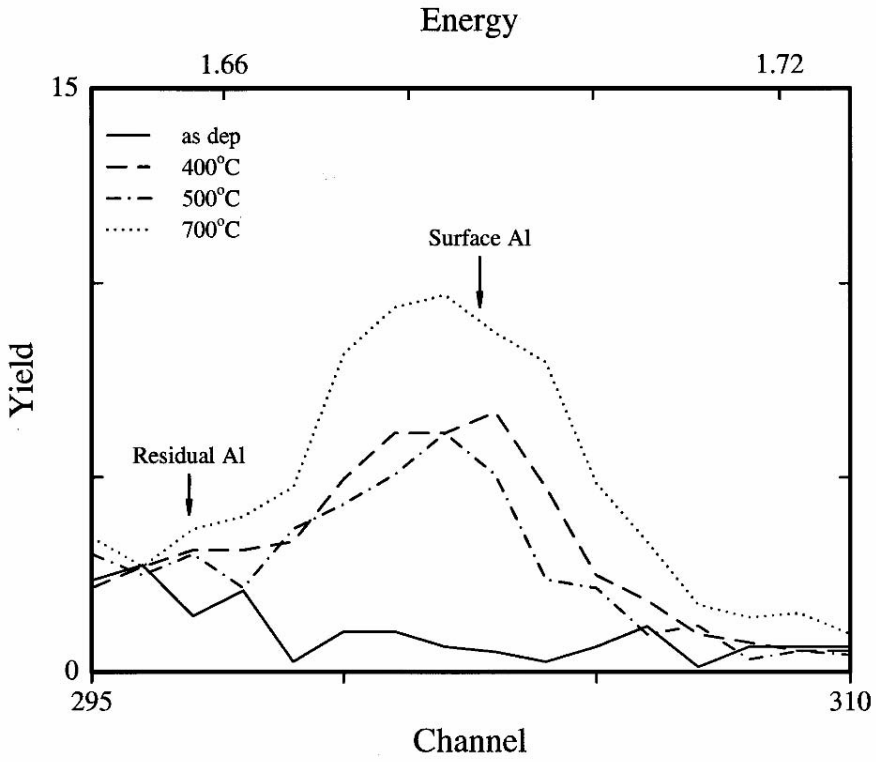

Figure 4.11. RBS spectra (3.0 MeV He^{+2}, 7° tilt) of the diffusion barriers before and after being annealed in flowing He-H for 30 minutes at three different temperatures [16]

The outdiffusion of Al increases with temperature. Although most of the Al segregates to the surface at 700 °C, the higher-than background signals of the trailing edges are indicative of the accumulation of Al in the Ag films at all temperatures. AES depth profiling of the Ag (200 nm)/Al (8 nm) bilayer annealed at 700°C, 30 minutes in a He–H ambient confirms the formation of an aluminum oxide surface layer (Figure 4.12). However, at this high temperature, a small amount of Al is still present at the Ag/SiO_2 interface.

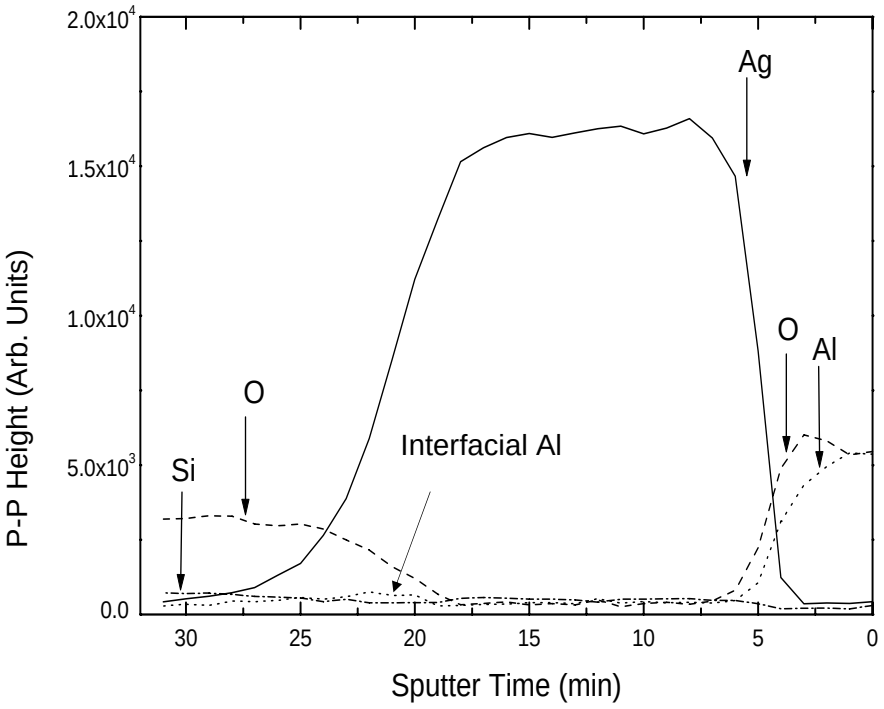

Figure 4.12. Auger depth profiles of a Ag/Al bilayer on SiO_2 annealed in He-H at 700°C for 30 minutes [16]

3. Ammonia Ambient

RBS spectra showing only the depth distributions of Al for the Ag/Al bilayer annealed in ammonia for temperature 400°C–700°C, 30 minutes are depicted in Figure 4.13. For the temperature range 400°C to 500°C, almost the same amount of Al diffuses to the surface. However, a much larger amount of Al is present at the surface for the sample annealed at 700°C. The residual Al in the Ag varies from 7 at.% (at 500°C) to less than 1 at.% (at 700°C).

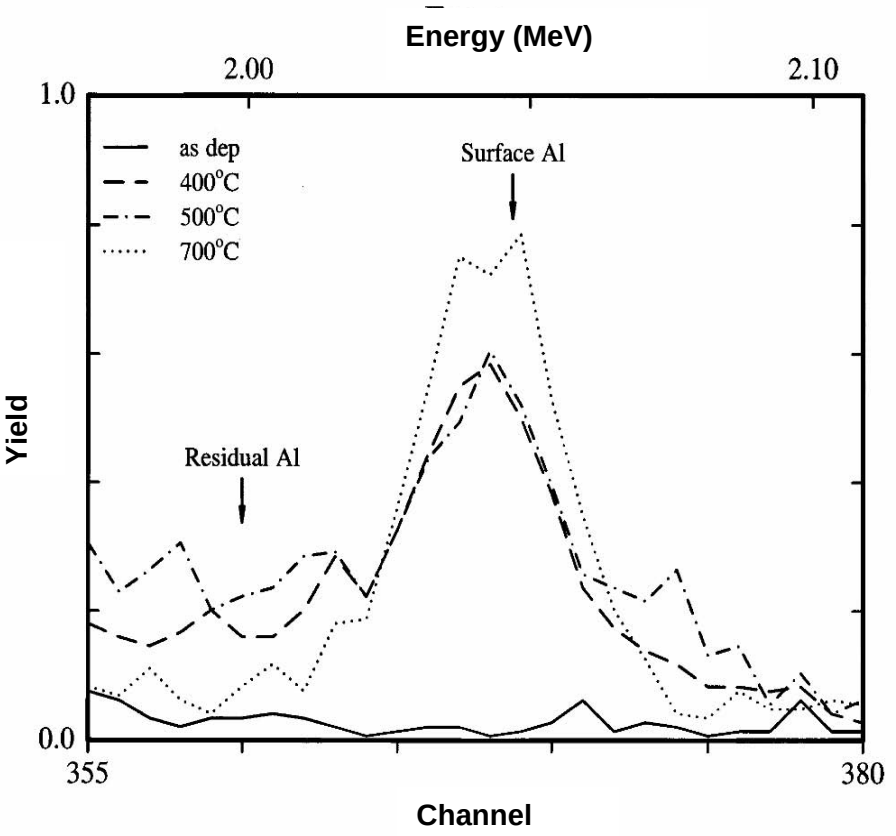

Figure 4.13. RBS spectra (3.7 MeV He^{+2}, 7° tilt) of the diffusion barriers before and after being annealed in flowing NH_3 for 30 minutes at three different temperatures [16]

Both RBS and AES analyses of the Ag/Al bilayer indicate that Al segregates to the free surface when annealed at various temperatures in Ar, He–H, and NH_3, respectively. For the three ambients, Al accumulates in the Ag during annealing (Figure 4.14). The accumulated Al versus annealing temperature profiles are very similar for the three ambients.

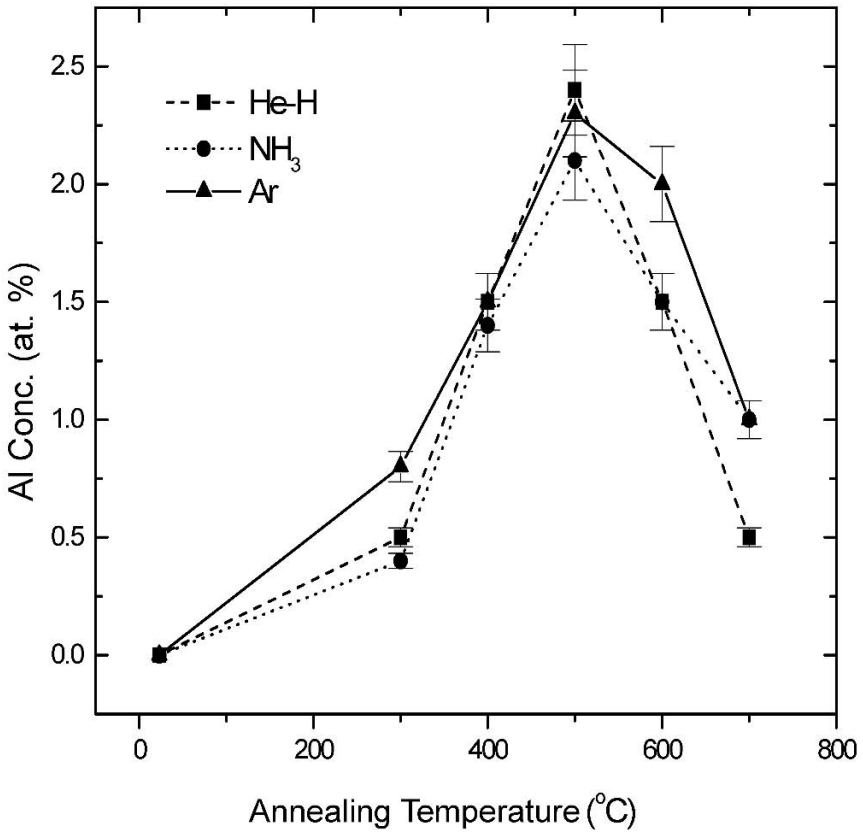

Figure 4.14. Plot of Al concentration versus annealing temperature for three different ambients [16]

4.4.3.2 Electrical Properties of Silver Films

Figure 4.15 shows the resistivity as a function of annealing temperature for the Ag(200 nm)/Al (8 nm) bilayer annealed in three different ambients (Ar, He–H, and NH_3). Annealing the samples in Ar at temperatures ranging from 300°C–700°C shows that the resistivity is higher than that annealed in He–H and ammonia, respectively.

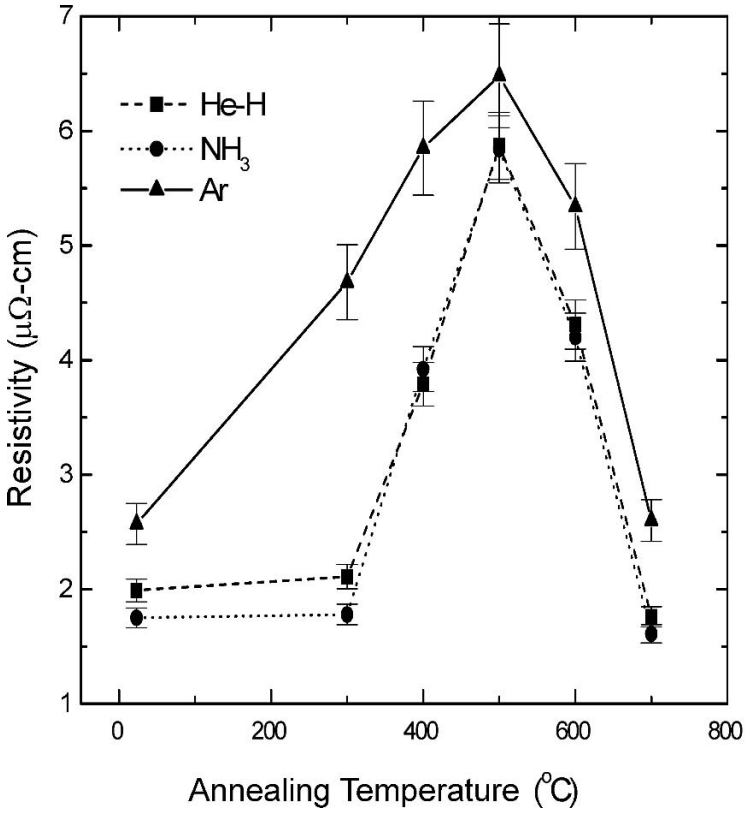

Figure 4.15. The Ag resistivity of Ag(200 nm)/Al(8 nm) bilayer on SiO_2 versus annealing temperature for three different ambients [16]

The higher resistivity in this case is due to the higher residual amount of Al in the Ag layer. For the samples annealed in He–H and NH_3 the resistivity remains almost constant for temperatures up to 300°C; whereafter, it increases linearly to a maximum value of about 6 μΩ-cm at 500°C. The resistivity then decreases to the value of the as-deposited samples at 700°C. It is evident that annealing the Ag/Al bilayers in these ambients gives rise to silver films with almost the same resistivity. The resistivity of the samples annealed in Ar does not show the plateau for temperatures, <300°C, but rather a linear increase from room temperature.

The behavior of the resistivity with an annealing temperature which resembles that observed for the variation of the accumulated Al in the Ag layer as shown in Figure 4.14. Therefore, it seems that the accumulated Al concentrations dictate the resistivity values. It is clear that the resistivity of the Ag films increases with the amount of Al that remains in the Ag film after annealing.

4.4.4 Discussion

4.4.4.1 Aluminum Transport in Silver Films

RBS and AES analyses reveal that annealing a Ag (200 nm)/Al(8 nm) bilayer in an inert gas (such as He–H or Ar) or corrosive gas like NH_3 results in the diffusion of Al through the Ag layer to the surface. For the inert gases, the segregated Al reacts with residual oxygen at the free surface to form an aluminum oxide. In the case of a Ag/Al bilayer annealed in an ammonia ambient, the Al segregates to the surface to react with residual O and N to form an Al-oxynitride.

The AES line-shapes (not shown) suggested that the oxide is Al_2O_3. It was difficult to detect the presence of the N with a nuclear resonance signal. The data clearly indicates that the amount of Al that segregates to the surface is almost independent of the ambient, but dependent on the annealing temperature. At higher temperatures, more Al moves to the free surface. The formation of an aluminum oxide for all ambients suggests that the outdiffusion of Al is not reaction limited but governed by temperature enhanced factors. Wang *et al*. reported that the segregation of Al in the Ag/Al system annealed in ammonia is governed by a competition between the movement through the Ag and the trapping of Al in the Ag film [12]. The retardation is influenced by both chemical affinity between Al and Ag and the interfacial barrier at the Ag/Al-oxynitride interface in the case of the NH_3 anneals. This model further explains that at higher temperatures, the Al atoms acquire enough thermal energy to overcome the interfacial barrier.

It is known that materials with higher surface energies than that of the substrate tend to form clusters since they cannot wet the substrate [13]. If this is the case for a given metal/SiO_2 system, the as-deposited metal layers do not adhere well to the oxidized substrate. It has been reported that the incorporation of a very small amount of O into Al during deposition may result in the development of internal compressive stress in the film. Figure 4.16 shows a plot of the theoretical values for the thermal stress as a function of annealing temperatures for three different systems.

The difference in thermal expansion coefficients between the metal and the substrate results in a huge compressive stress field. Zeng *et al*. [14] reported that for a Ag/Ti bilayer structure, a low tensile stress is present in the Ag film from the nonequilibrium growth during the film deposition. When encapsulating the bilayer at 600°C, a thermal mismatch stress is produced.

This stress caused by heating the Ag/Al sample must be a contributing factor for the Al diffusion to the surface. It is believed that the sum of compressive stresses in the surface oxide layer, and that in the underlying silver layer, give rise to a stress field across the entire Ag/Al bilayer which significantly contributes to Al outdiffusion. Therefore, in addition to the driving force caused by the concentration gradient, the thermal expansion mismatch between the films and the substrate the high stress field caused by heating the sample must be considered as an important factor for Al outdiffusion.

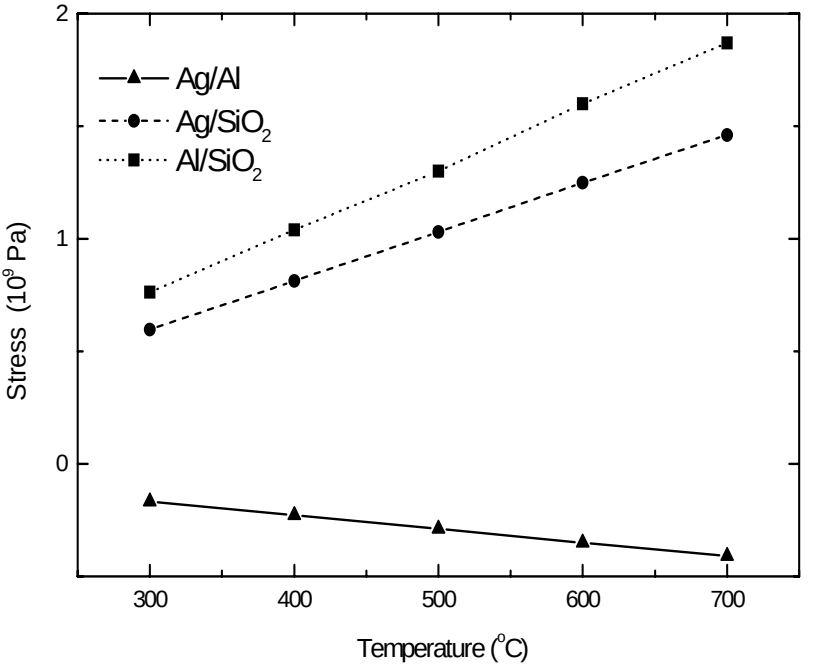

Figure 4.16. Plot of theoretical stress values versus annealing temperature for three different systems [16]

4.4.4.2 Electrical Properties of Silver Films

In this study, it was also found that at higher temperatures more Al segregates to the surface. The trapping of Al in the Ag is responsible for the high electrical resistivities observed for the low temperature anneals. However, heat treatment at higher temperature reduces the residual Al and hence gives rise to lower resistivities.

X-ray diffraction spectra (not shown) showed no formation of any intermetallic compounds (*e.g.*, Ag_3Al and Ag_2Al). This means that the Al appears in the Ag film in elemental form. As demonstrated by Figure 4.15, the ambient does not play a significant role in the resistivity of thin films. Among the three ambients employed, the lowest resistivities are obtained for the He–H or NH_3 anneals and the highest for the Ar. The higher resistivity is due to a slightly thicker Ag layer. The high resistivities at 500°C suggest that some Al is still present in the Ag film in elemental form. Thus, the outdiffusion of Al is not ambient limited but governed by temperature enhanced factors. According to the dilute Ag–Al alloy theory [15] the resistivity of the Ag layer is very sensitive to the change of the Al concentration within it.

4.4.5 Conclusions

The results obtained from annealing Ag (200 nm)/Al(8 nm) bilayer structures in different ambients at different temperatures and times indicated that Al diffuses through the Ag to the free surface [16]. An Al_xO_y surface layer is formed at the free surface due to the reaction between Al with the residual oxygen in the ambient. The data indicate that the Al_xO_y thickness obtained from annealing the bilayer increases with temperature with a thickness of ~13 nm at a temperature of 700°C. Less than 1 at.% Al accumulates in the Ag film during annealing at these high temperatures. For the Ag (200 nm)/Al(8 nm) bilayer system, the resistivity of the samples annealed in these ambients are almost the same as the as-deposited value. The much lower resistivity of the Ag films compared to that of alloys might be due to the absence of any Ag–Al intermetallic compounds formed and the lower Al accumulation in the Ag. The residual Al dictates the resistivity. The highest resistivities are obtained for the samples annealed at 500°C.

The data also indicated that the surfaces of the samples are smooth up to 400°C. Above this temperature, hillock and hole formation occurs and hence extensive surface roughness as well. A combination of chemical temperature-enhanced effects such as chemical affinity, interfacial energy, and internal compressive stresses are believed to be responsible for the increased Al segregation and the rough surfaces formed at high temperatures. It is believed that hillock formation takes place as a result of thermal stress relaxation. Therefore, it is likely that the relaxation of thermal stress in an inert atmosphere occurs simultaneously by surface self-diffusion of silver atoms once the relaxation centers are formed.

Compared to Ag/SiO_2, agglomeration was suppressed in the $Ag/Al/SiO_2$ system by the formation of an Al oxide surface layer and the limited reaction between Al and the underlying SiO_2 substrate. Therefore, annealing a Ag/Al bilayer on SiO_2 in ambients such as Ar, He–H, and NH_3, not only prevented the agglomeration of the Ag films but also improved the adhesion of Ag on the dielectric [16].

4.5 Thickness Dependence on the Thermal Stability of Silver Thin Films

4.5.1 Introduction

Silver has been studied as a potential interconnection material for ultra large-scale integration technology because its bulk electrical resistivity (1.57 μΩ-cm at room temperature) is lower than other interconnection materials (Al—2.7 μΩ-cm and Cu—1.7 μΩ-cm) [1, 3, 14, 17]. In addition, silver has a higher electromigration resistance than aluminum. However, agglomeration of silver thin films at high temperatures has been considered as one of the disadvantages of silver thin films since it influences the thermal stability and is a major concern for the reliability of

thin-film interconnects. Agglomeration is a transport process that occurs during thermal annealing. Changes in the morphology of thin films also influence variations of the electrical resistivity (*i.e.*, increase in resistivity due to increased surface scattering of conduction electrons). Here, *in situ* van der Pauw four-point-probe analysis is used to elucidate the thermal stability of silver thin films having different thicknesses on SiO_2. The onset temperature (T_0) is a means to quantify the thermal stability of silver thin films when using the *in situ* four-point-probe technique.

The onset temperature is defined as the temperature at which the electrical resistivity deviates from linearity when increasing the substrate temperature. The electrical resistivity increases linearly as the temperature increases due to the phonon scattering when the void density remains constant in the film. Deviations in the electrical resistivity from linearity during ramping relate to the increase of surface roughness due to the initiation of agglomeration in the silver thin films.

4.5.2 Experimental Details

Silver thin films of various thicknesses were deposited on thermally grown SiO_2 using electron-beam evaporation. Typical base pressures and operation pressures were 5×10^{-8} and 5×10^{-7} Torr, respectively. Sheet resistances of the Ag thin films were obtained with an *in situ* van der Pauw four-point-probe. The thermal ramps were performed in a vacuum ($<2\times10^{-7}$ Torr) at 0.1°C/s from room temperature until a temperature where the value of sheet resistance cannot be obtained due to agglomeration and island formation. The electrical resistivity of the films was calculated from the sheet resistance data and film thickness values measured by Rutherford backscattering spectrometry.

4.5.3 Results

The electrical resistivity changes and the thickness dependence of thermal stability of Ag on the SiO_2 structure during continuous temperature ramping are presented in Figure 4.17. The curve of the 35 nm Ag on SiO_2 is divided into two distinct regions, region 1 and region 2. In region 1, the resistivity increases linearly with temperature from room temperature to the onset temperature of approximately 102°C.

The onset temperature is denoted at the end of region 1 as shown in Figure 4.17. The linear increase of resistivity is a result of electron scattering by lattice vibration. Agglomeration and void formation are not detectable in this temperature range (region 1) and the silver thin film is thermally stable. Once the onset temperature is exceeded, the resistivity increases rapidly and becomes infinite at the end of region 2. The abrupt change in resistivity is a consequence of the increase of surface scattering due to agglomeration of silver thin films and the formation of an island resulted in the infinite value of electrical resistivity.

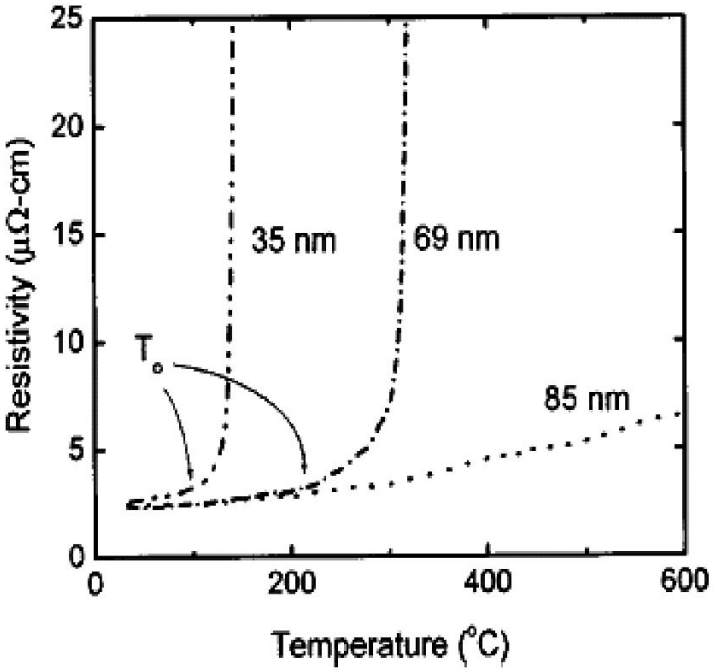

Figure 4.17. Resistivity as a function of temperature for various film thicknesses of Ag on SiO_2 annealed in a vacuum at 0.1°C/s [3]

These findings correlate well with those based on percolation theory that shows that the area fraction of the surface uncovered by agglomeration scales linearly in time [5]. It is also of great interest to investigate this in more detail to determine if agglomeration produces uncorrelated percolation-like disorder. Note that the resistivity of thinner films at room temperature is higher than that of thicker films at same temperature. The variation of resistivity at different thicknesses at temperatures <100°C occurs due to the increased surface scattering of electrons. This effect impacts the resistivity greatly as the thickness of film approach the mean-free path (Ag: 40.5 nm at 100°C) of the conduction electron. Also, the onset temperature of thicker films is higher than those of thinner films (see Table 4.4), and the onset temperature is not found over the temperature range for thin films having thicknesses over 85 nm.

Table 4.4. Onset temperature for silver thin films on SiO_2 for various thicknesses when annealed in a vacuum. The ramp rate was 0.1°C/s [3]

Silver thin-film thickness (nm)	Onset temperature (°C)
35	102
53	153
62	174
69	203

The increased resistivity for the thinner films correlates with the increase in surface area, *i.e.*, an increase in surface scattering of electrons. In addition, the smaller cross-sectional area increases the resistivity as a consequence of the void formation and agglomeration. As a result, less thermal energy is needed for voids to grow throughout the film thickness in thinner films [3]. The film thickness versus T_0 can be modeled by an Arrhenius relationship. The film thickness is empirically related to the onset temperature as:

$$\lambda^3 = C \exp(-\frac{E_a}{kT_0}) \tag{4.1}$$

where C is a pre-exponent constant and T_0 is the onset temperature. Equation 4.1 is employed to calculate the activation energy for onset of agglomeration (E_a) for a silver thin film annealed in a vacuum at a 0.1°C/s ramp rate.

The activation energies for the onset of agglomeration based on Equation 4.1 in terms of film thickness and onset temperature are calculated, and the Arrhenius relation is shown in Figure 4.18. The results fit well to Arrhenius relation and the activation energy of Ag/SiO_2 annealed in a vacuum (E_a=0.32±0.02 eV) is comparable to that reported in literature for surface diffusion activation energy of silver thin films in a vacuum (0.3–0.44 eV) [18, 19]. Hence, it is believed that surface diffusion is the driving force for onset.

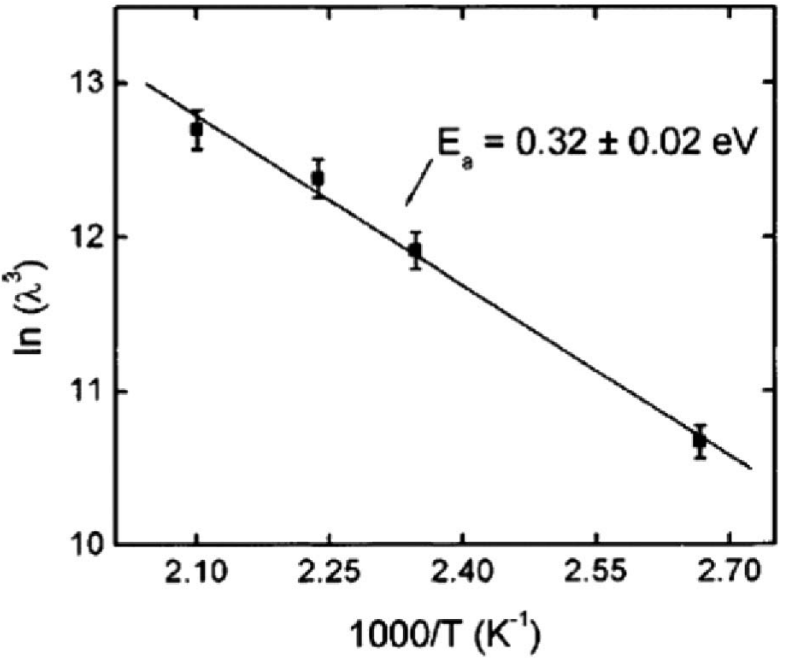

Figure 4.18. Arrhenius plots calculated using Equation 4.1 for a Ag on SiO_2 structure annealed in a vacuum for a 0.1°C/s ramp rate [3]

4.5.4 Conclusions

Previously, Sieradzki *et al*. [5] used the ramping technique to show that the time evolution of Ag agglomeration is essentially described by uncorrelated percolation-like disorder. They also anticipated that the ramping technique in combination with percolation theory would seem to be a new and valuable approach for the examination and prediction of Ag de-wetting phenomena in metallic thin films. These results confirm that the ramping technique in combination with a relationship based on Ag surface diffusion adequately describes the Ag thickness dependence of the onset temperature.

The combination of the two approaches will provide insight into the description of failures in future high temperature electronics. In conclusion, thermal stability of silver thin films was studied using an *in situ* four-point-probe technique. During the temperature ramp, the concept of onset temperature, which defines two distinct regions, was introduced as a technique measuring the thickness dependence of the thermal stability. It was observed that film thickness plays an important role in the thermal stability, which increased as the film thickness increased. The thermal stability of silver thin films was enhanced by an increase in the film thickness or by a reduction of the anneal temperature to below the onset temperature [3].

4.6 References

[1] T. L. Alford, D. Adams, T. Laursen, and B. M. Ullrich, Appl. Phys. Lett. 68, 3251(1996).
[2] K. S. Gadre and T. L. Alford, J. Vac. Sci. Technol. B 18, 2814(2000).
[3] H. C. Kim, T. L. Alford, and D. R. Allee, Appl. Phys. Lett. 81, 4287(2002).
[4] T. L. Alford, Lingui Chen, and K. S. Gadre, Thin Solid Films 429, 248(2003).
[5] K. Sieradzki, K. Baily, and T. L. Alford, Appl. Phys. Lett. 79, 3401(2001).
[6] H. C. Kim, and T. L. Alford. J. Appl. Phys. 94(8), 5393(2003).
[7] K. S. Gadre and T. L. Alford, J. Vac. Sci. Technol. B 18(6), 2814(2000).
[8] L. C. Feldman and J. W. Mayer, Fundamentals of Surface and Thin Film Analysis (North-Holland), New York, 307(1986).
[9] S. W. Russell, S. A. Rafalski, R. L. Spreitzer, J. Li, M. Moinpour, F. Moghadam, and T. L. Alford, Thin Solid Films 262, 154(1995).
[10] 1998 Annual Book of ASTM Standards, edited by R. A. Storer (ASTM, Philadelphia), Vol. 6.01, 356(1998).
[11] G. R. Moore, and D. E. Kline, Properties and Processing of Polymers for Engineers (Prentice-Hall), New York, 9(1984).
[12] Y. Wang, T. L. Alford, and J. W. Mayer, J. Appl. Phys. 86, 5407(1999).
[13] K. N. Tu, J. W. Mayer, and L. C. Feldman, Electronic Thin Film Science for Electrical Engineers and Materials Scientists - Macmillan, New York, (1992).
[14] Y. Zeng, Y. L. Zou, T. L. Alford, F. Deng, S. S. Lau, T. Laursen, and B. Manfred Ullrich, J. Appl. Phys. 81, 7773(1997).
[15] CRC Handbook of Electrical Resistivities of Binary Metallic Alloys, edited by Klaus Schroder (CRC, Boca Raton), Florida, 44(1983).
[16] Gerald F. Malgas, Daniel Adams, Phucanh Nguyen, Yu Wang, T. L. Alford, and J. W. Mayer, J. Appl. Phys. 90(11), 5591(2001).
[15] T. L. Alford, D. Adams, T. Laursen, and B. M. Ullrich, Appl. Phys. Lett. 68, 3251(1996).
[16] Y. Zeng, Y. L. Zou, T. L. Alford, S. S. Lau, F. Deng, T. Laursen, and B. M. Ullrich, J. Appl. Phys. 81, 7773(1997).
[17] Y. Zeng, T. L. Alford, Y. L. Zou, A. Amali, B. M. Ullrich, F. Deng, and S.S. Lau, J. Appl. Phys. 83, 779(1998).
[18] R. E. Hummel and H. J. Geier, Thin Solid Films 25, 335(1975).
[19] G. Neumann and G. M. Neumann, in Diffusion Monograph Series: Surface Self-Diffusion of Metals, edited by F. H. Wohlbier (Diffusion Information Center, Bay Village), Ohio, 57(1972).

5

Silver Electromigration Resistance

5.1 Introduction

Electromigration has been identified as a primary failure mode of interconnect lines used in semiconductor-integrated circuits. It is a high-current density induced mass transport phenomenon manifesting itself as voids, hillocks, or open circuits, due to a momentum exchange between conduction electrons and host metal atoms. The electromigration failure of Al(Cu) interconnects has been extensively investigated because of the dominant use of Al(Cu) as conductors in microelectronics devices for decades. Recently, the electromigration study of Cu has been conducted considerably as well, since the trend to replace Al(Cu) with Cu is becoming apparent for ultra large scale integration (ULSI) applications. Ag, as the most conductive metal, has also drawn attention as an interconnect material for some potential applications in ULSI [1, 2]. Ag has some advantage over Cu in terms of the conductivity.

Since the wide application of Cu metallization will be facing some difficulties [3], Ag may find its applications if the electromigration resistance can be further improved and some other issues [2] can be addressed. Compared to Al, Ag is expected to have better electromigration resistance. However, the electromigration resistance of Ag needs to be further improved in order to be comparable to Cu.

A novel encapsulation process is described for patterned Ag lines and the effect of this process on the Ag electromigration is evaluated.

5.2 Experimental Details

Ti film (50 nm) and Ag film (100 nm) were sequentially deposited on a thermally oxidized (100) Si wafer without breaking vacuum in an electron beam evaporator. The base pressure before Ti deposition was approximately 1.2×10^{-7} Torr. The Ti film was mainly used to form an encapsulation layer on the Ag line surface, as will be shown later. A conventional optical lithography process was used to transfer the designed mask pattern onto the deposited $Ag/Ti/SiO_2/Si$ films. The pattern configuration consists of one test line (600 μm in length and 10 μm in width) and two pads (200×200 μm^2) located at the ends of the line. A reactive ion etch (RIE) process in an O_2 plasma was employed to etch away the Ag unprotected by photoresist. During the etch process, the underlying Ti acted as an etch stop.

The encapsulation process of the Ag patterns was carried out in a quartz-tube furnace with a flowing high purity NH_3 gas and a flow rate of approximately 2 l/min. The tube was evacuated and then NH_3-purged alternately for three cycles before loading the pattern samples into the hot zone. The encapsulation annealing took place at 550°C for 30 minutes. Auger electron spectroscopy (AES) and cross-section transmission electron microscopy (XTEM) were employed to characterize the Ag line patterns.

The AES was performed in a scanning Auger microscope surface analysis system with an incident energy of 3 keV at 0.2 μA. The Auger electron signal was collected from the surface of one pad in the Ag test pattern, since the Ag test line was too narrow.

The XTEM observation was carried out in a JEM 2000FX electron microscope at an operating voltage of 200 kV. The electromigration test of both bare Ag lines and NH_3-annealed Ag lines was carried out in a Tektronics electrical testing system. The current density was approximately 4×10^7 A/cm^2 and an external heating (200°C) was provided. During the tests, the surface of the test Ag lines was inspected periodically by an optical microscope, and the time when significant number of voids and hillocks can be observed on the test line was defined as the primary criterion for the electromigration failure. Further examination of the surface morphology was conducted by using plane-view scanning electron microscopy (SEM). Four samples were tested for both test configurations (samples A, B, C, and D for bare Ag patterns, and samples A′, B′, C′, and D′ for and NH_3-annealed Ag patterns). The average of four failure times was used to evaluate the electromigration resistance.

5.3 Results and Discussion

The AES spectrum as acquired from the NH_3-annealed Ag pad is shown in Figure 5.1. In standard AES spectrum for pure Ti, there are two Ti peaks, one is Ti(*LMM*) at 387 eV, the other is Ti(*LMV*) at 418 eV.

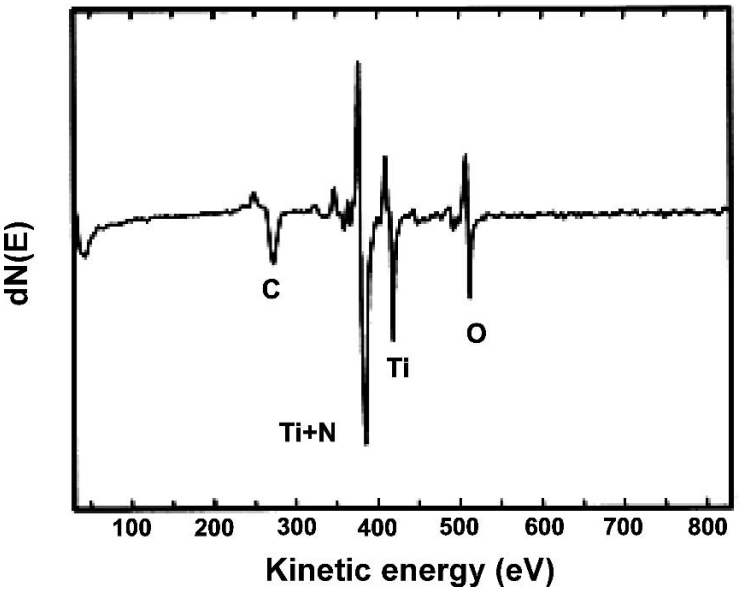

Figure 5.1. AES spectrum as acquired from the surface of one pad in the Ag test pattern after annealing in NH_3 at 550°C, 30 minutes [4]

The N(*KLL*) Auger peak is at 379 eV, which usually coincides with lower-energy Ti peak. The intensity ratio *R* of the two Ti peaks, defined as $I_{(418\ eV)}/I_{(387\ eV)}$, can be used to characterize various Ti compounds. The value of *R* has been determined to be 1.3 in pure Ti, 0.6 in TiO_2, and 0.4 in TiN. In the present case, the *R* value is approximately 0.5. It is in between 0.6 for TiO_2 and 0.4 for TiN, suggesting that the compound is most likely to be TiN(O). The appearance of O peak in AES spectrum also confirms the incorporation of O. The oxygen is believed to come from the furnace ambient. Even though the furnace tube was purged for three cycles, there might still be some residual O remaining in the tube. By vision, the surface color of the Ag lines changes into golden-yellow after NH_3 annealing, which is the typical color for the TiN based compound.

The electromigration test results for the bare Ag lines show that at the early stage of the test, a partial depletion region first appears at the line segment, which is immediately near the cathode pad, and afterwards, this region starts to extend progressively towards the anode side. This partial depletion region is virtually comprised of a large number of voids and hillocks located side by side. During the drift of this partial depletion region, significant voids and hillocks also form side by side at other areas of the line. A typical example is given in Figure 5.2, which shows the scanning electron microscope (SEM) image of the morphology of the center area of the bare line sample D after 3 hours testing. A cluster of hillocks is located immediately on the right side of the voiding area. This confirms that mass transport is directed towards the node (the right-hand direction) and the formation of hillocks is the consequence of mass depletion from voiding areas.

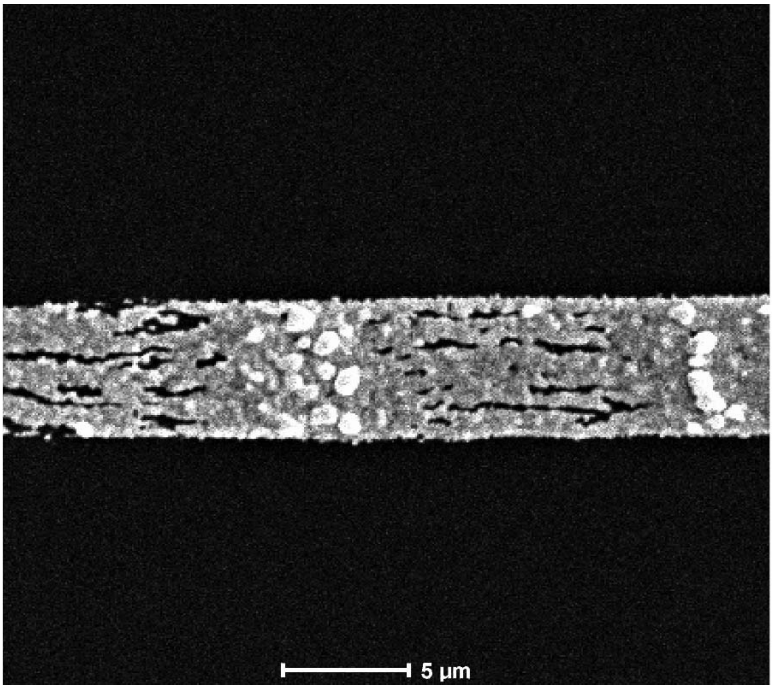

Figure 5.2. Plane-view SEM micrograph indicating the surface morphology of the bare Ag test sample D (near-cathode segment), tested for 3 hours. The line width is approximately 10 µm. The left portion of the line segment is the partial depletion region, which is composed of a large number of voids and hillocks. It is noted that the actual electric current flowed through the lines from the right to left [4].

The partial depletion occurring near the cathode presumably results from the long-range temperature gradient due to the non-uniform Joule heating caused by the difference in the cross section area of the test line and pads. More Joule heating and higher temperature rise are anticipated in the test line area than those on the pad area.

As a consequence, there are more atoms leaving from the near-cathode line towards the anode than those entering from the cathode-side pad driven by the electron wind. The electromigration test results of four bare Ag lines are summarized in Table 5.1.

Table 5.1. Electromigration test results of bare Ag lines [4]

Identification of test lines	Actual test time (h)	Appropriate time for observable formation of a partial depletion region (min)
A	3	90
B	1.5	25
C	1.5	40
D	3	50

For all tested Ag lines, which were encapsulated by TiN(O), no partial depletion area and no significant number of voids and hillocks were observed even after testing for much longer time than that for bare Ag lines (see Table 5.2). For instance, for encapsulated line sample B′, which was tested for 7 hours, only four to five voids are found across the entire length of the line. The voiding area of this sample is shown in Figure 5.3 [4]. These results were typical as well for other test samples.

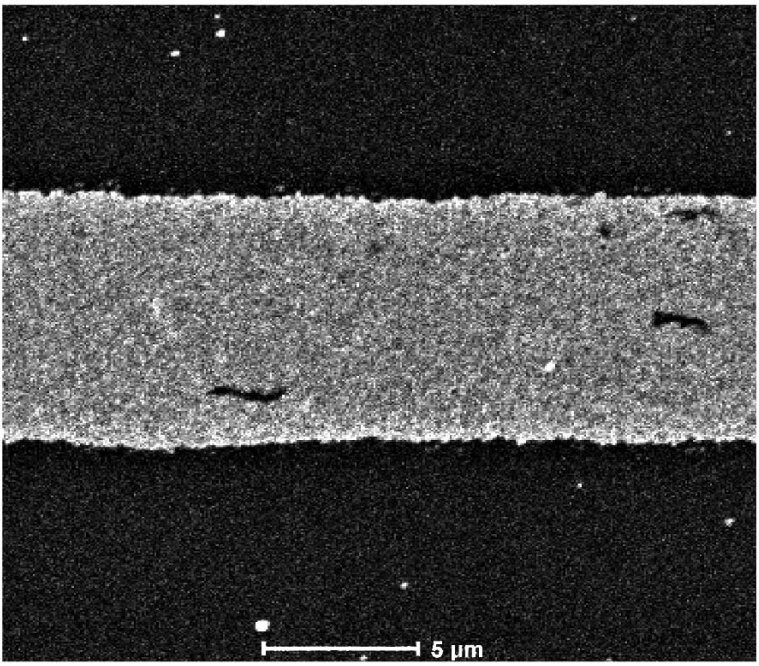

Figure 5.3. Plane-view SEM micrograph of the TiN(O) encapsulated Ag line sample B′, tested for 7 hours. The line width is approximately 10 µm. Only four to five voids were found across the entire length of the line [4].

Table 5.2 indicates the actual test time for all four test samples and also the total number of voids found across the entire line. According to the results in Tables 5.1 and 5.2, the encapsulation process improves the electromigration resistance (in terms of the time required for the formation of significant number of voids and hillocks) of Ag metallization by at least one order of magnitude for the test structures and conditions used in this study. Based on the tests conducted on four Ag lines, the average time for the formation of considerable number of voids and hillocks (partial depletion region) in bare Ag lines was approximately 50 minutes (Table 5.1). However, the corresponding time for encapsulated Ag lines was at least 9 hours.

Table 5.2. Electromigration test results of TiN(O)-encapsulated Ag lines [4]

Identification of test lines	Actual test time (h)	Surface morphology changes after testing
A′	11.0	11–13 voids
B′	7.0	4–5 voids
C′	9.0	8–9 voids
D′	10.0	8–9 voids

The cluster of hillock adjacent to the void area (shown in Figure 5.2) is consistent with the observation of Breitling and Hummel [5] that voids and hillocks are uniformly side-by-side distributed along the electromigration-tested Ag strip. It is known that the electromigration failures of interconnect lines are primarily caused by gradients which can lead to atomic flux divergences under the electrical driving force. There are two major types of gradients that may exist: local gradients due to microstructural or chemical inhomogeneities, and long-range temperature gradient due to nonuniform Joule heating and heat dissipation. Based upon our observations, it appears that in the present case the influences from both gradients are superimposed. The side-by-side distribution of voids and hillocks along the whole line length is attributed to the local inhomogenities, such as different grain sizes, and variation in film thickness. Partial depletion occurring near the cathode is assumed to result from the long-range temperature gradient due to the nonuniform Joule heating caused by the difference in the cross-section area of the test line and pads.

The round shape of the hillocks as seen in Figure 5.2 implies that surface diffusion is most likely to be the dominant mechanism of mass transport, since the agglomeration of hillocks is the result of minimizing surface energy configuration by the surface diffusion of Ag atoms. For simplification, it is assumed that all Ag grains have a hexagonal shape and transverse through the entire film thickness. If this is the case, then the ratio of the surface area to the grain boundary area can be estimated to be ~2.3 for bare Ag lines (based on the estimated average Ag grain size from the TEM analysis). As a result the larger surface area and lower activation energy for surface diffusion [6] leads to surface diffusion dominant electromigration. After the encapsulation process, the Ag surface is capped by a thin layer of TiN(O). The mobility of Ag atoms at the TiN(O)/Ag interface is substantially reduced. Therefore the electromigration resistance is improved significantly. By examination of the surface of the encapsulated Ag lines tested for a long time, almost no round hillocks are observable. This implies that the surface diffusion has been hindered substantially. The formation of voids in this case is most likely to arise from the grain-boundary diffusion. Comparison of Tables 5.1 and 5.2 suggests that the encapsulation process improves the electromigration resistance of Ag metallization by at least one order of magnitude for the test structures and conditions used [4].

The significance of this work lies in that it has demonstrated the possibility to improve the electromigration lifetime of Ag interconnects considerably by applying a novel process technique. The TiN(O) layer can also prevent Ag lines from corroding and agglomerating. The adhesion between Ag and the underlying SiO_2 can be promoted as well [4].

5.4 Conclusions

An encapsulation process has been applied to Ag line patterns on $Ti/SiO_2/Si$ substrates, which are fabricated by using conventional photolithography and RIE in an O_2 plasma. The electromigration behavior of the bare Ag lines has been investigated. Upon the encapsulation and annealing in flowing NH_3, a TiN(O) thin layer forms at the surface of the Ag lines. The electromigration tests show that this process has significantly improved the electromigration resistance of Ag lines by primarily hindering the surface diffusion of Ag atoms. The electromigration lifetime of Ag lines can be increased by at least one order of magnitude [4].

5.3 References

[1] T. L. Alford, D. Adams, T. Laursen, B. Manfred Ullrich, Appl. Phys. Lett. 68, 3251(1996).
[2] Y. L. Zou, T.L. Alford, Y. X. Zeng, A. Amali, T. Laursen, B. M. Ullrich, J. Appl. Phys. 82, 3321(1997).
[3] J. Li, G. Vizkelethy, P. Revesz, J. W. Mayer, K. N. Tu, J. Appl. Phys. 69, 1020(1991).
[4] Y. Zeng, L. Chen, Y. L. Zou, P. A. Nyugen, J. D. Hansen, T. L. Alford. Materials Letters 45, 157(2000).
[5] H .M. Breitling, R. E. Hummel, J. Phys. Chem. Solids 33, 845(1972).
[6] R. E. Hummel, H. J. Geier, Thin Solid Films 25, 335(1975).

This page intentionally blank

6

Integration Issues

6.1 Factors Influencing the Kinetics in Silver-Aluminum Bilayer Systems

6.1.1 Introduction

Kinetics studies were conducted on both Ag-refractory metal alloys and bilayers on silicon dioxide substrates during self-encapsulation in an NH_3 ambient. Adams *et al*. [1] and Zou *et al*. [2] studied the dealloying kinetics of Ag (Ti), Cu (Ti) and Cu (Cr) alloys during nitridation in NH_3 and reported that the kinetics of the encapsulating layer (TiN or CrN) formation revealed a self-limiting behavior. The rapid dealloying of Ti in Ag (Ti) alloys followed by a much slower diffusion rate is a result of microstructural changes occurring simultaneously with the out-diffusion. The studies of the kinetics of the alloys further showed that incomplete dealloying occurs resulting in a high residual refractory metal concentration. The residual refractory metal in Ag results in higher than elemental resistivities of these metals [1]. Alford *et al*. [3] studied the encapsulation of Ag by a TiN layer by annealing Ag/Ti bilayer structures in an NH_3 ambient. Compared to the alloys nitridation of the bilayers resulted in minimal Ti accumulation in Ag films.

From a previous study on self-encapsulation of Ag/Al bilayers [4,5], it was shown that Al diffuses through the Ag layers and reacts with both NH_3 and residual oxygen in the ambient to form a thin $Al_xO_yN_z$ diffusion barrier at the surface. Wang *et al*. [5] reported that the reaction kinetics in the Ag/Al bilayers system is dominated by the out-diffusion of Al through Ag. According to this study, the

characteristic diffusion length of Al in Ag is about 110 μm at 725°C for 30 minutes which is not suitable for studying Ag films with layer thickness of 100–200 nm. For this reason, the authors only considered Al layers of thickness 8 nm. The kinetics was determined by monitoring the formation of the aluminum oxide on the surface of the Ag films. This study considers thicker Al layers (8–30 nm) in the Ag/Al system in order to establish the factors governing the kinetics in this case.

6.1.2 Experimental Details

Aluminum (Al) and silver (Ag) films were sequentially deposited on thermally oxidized silicon (Si) wafers by electron-beam evaporation to form Ag/Al bilayer structures. The silver film thickness was kept constant at 200 nm while the Al thickness varied between 8 and 30 nm. The base pressure of the chamber before deposition was about 10^{-7} Torr. During deposition, the operating pressure was about 10^{-6} Torr. The Ag/Al bilayer structures were annealed in a quartz tube furnace at temperatures ranging from 400 to 600°C for times between 15 and 120 minutes in a flowing electronic grade (99.99%, with $H_2O < 33$ and $O+Ar < 10$ molar ppm) ammonia (NH_3) ambient at atmospheric pressure.

Ammonia instead of oxygen was used in order to suppress hillock and hole formation in the silver layer. A flow rate of 2 l/min was maintained during anneals. Before each anneal, the annealing chamber was evacuated to about 10 mTorr followed by a 2.5 minutes purged with NH_3. The annealed samples were also allowed to cool in the NH_3 before removal from the chamber. Rutherford backscattering spectrometry (RBS) using a 2 MeV and 3.7 MeV He^{+2} beams at 7° tilt and total accumulated charge of 10–20 μC were used to determine the composition and thickness of the samples. The 3.7 MeV beam energies correspond to nitrogen (N) resonance and were used to detect N. The RUMP computer simulation program was used to analyze the RBS spectra.

6.1.3 Results

In order to understand the kinetics of the aluminum oxide growth and the related mechanisms, the sample configurations and annealing conditions were varied. Three Ag/Al bilayer configurations: Ag(200 nm)/Al(8 nm), Ag(200nm)/Al(20 nm), and Ag(200 nm)/Al(30 nm) were considered. The annealing was carried out at three different temperatures, namely 400, 500, and 600 °C at four times ~15, 30, 60, and 120 minutes.

6.1.3.1. Formation of Aluminum Oxide Surface Layer

The RBS spectra of the as-deposited Ag(200 nm)/Al(8 nm) bilayers are compared with those annealed at two different temperatures in an NH_3 ambient for 30 minutes (Figure 6.1). When the samples are annealed at 500°C and higher temperatures, Al segregates to the free surface and reacts with residual oxygen to form a thin aluminum oxide surface layer, consisting predominantly of Al and O. A small shift in the Ag peak position to lower energies is observed for the annealed samples; this shift is indicative of the formation of the thin surface layer. The height of the Ag peak is lower for the annealed samples compared to the as-

deposited as a result of the possible inclusion of lighter elements in the silver film. The surface Al is not clearly visible when the full spectra are shown (Figure 6.1a); therefore, a blow-up of the Al at the surface is given in Figure 6.1b).

The closeness in mass between Al and Si makes it almost impossible to separate the interfacial Al peak since it overlaps with the front edge of the silicon signal. A very thin surface layer of Al-oxide ~12 nm is formed at these temperatures (400–700°C). No reaction between Al and N from NH_3 ambient to form AlN was detected in this temperature range. For the same sample configuration, a thicker oxide layer was formed at 700°C than at 500°C, which suggests that the oxidation process has a strong temperature dependence (Figure 6.1b).

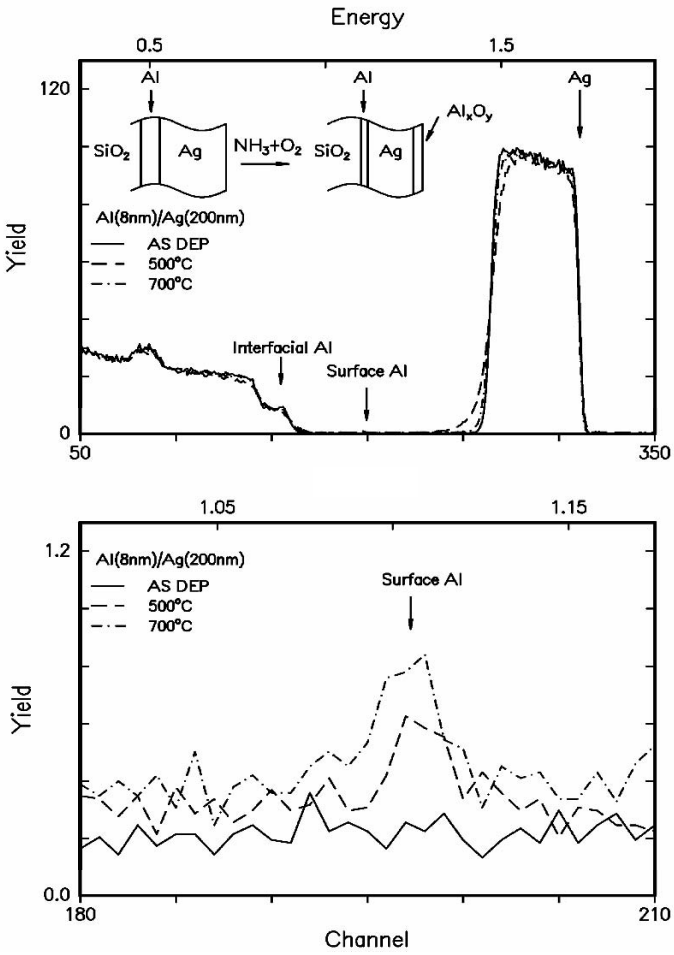

Figure 6.1. RBS spectra (2 MeV He^{+2}, 7° tilt) obtained from the Ag(200 nm)/Al(8 nm) bilayers on SiO_2 before and after annealing at two different temperatures in NH_3 ambient for 30 minutes. Only the Al surface peaks are shown in (b) [8].

At 2 MeV, the Ag peak shows no significant change when annealed at higher temperatures except for a small drop in the height. Only the Al peaks will therefore be shown. Figure 6.2 gives the RBS spectra of the surface Al peaks only for the Ag(200 nm)/Al(20 nm) bilayer structure. The amount of Al at the surface increases with annealing time with the largest amount corresponding to the 120 minute anneals. The spectra further show that the background yields for the annealed samples is higher than the backscattered yield of the as-deposited sample. This higher yield is due to the residual Al in the Ag film.

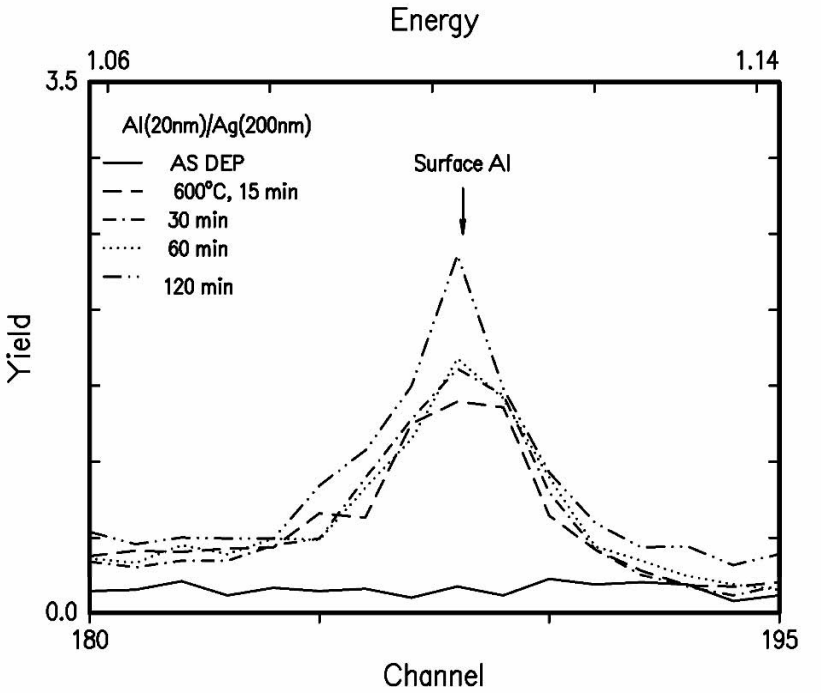

Figure 6.2. RBS spectra (2 MeV He^{+2}, 7° tilt) obtained from the Ag(200 nm)/Al(20 nm) bilayers on SiO_2 before and after annealing at 600°C in an NH_3 ambient for 15–120 minutes. Only the Al surface peaks are shown [8].

Figure 6.3 gives the RBS spectra of the surface Al peaks for the as-deposited Ag(200 nm)/Al(30 nm) bilayer and that annealed at 600°C for different times, respectively. Annealing the Ag(200 nm)/Al(30 nm) structure in an ammonia ambient at 600°C for times 15–120 minutes also resulted in the segregation of Al to the surface and the subsequent formation of a thin aluminum oxide layer at the surface. In Figure 6.3, it is evident that the surface Al peaks increases with annealing time (15–120 minutes). This suggests that the outdiffusion of Al through Ag is time-dependent.

Although most of the Al segregates to the surface, the high background signals of the trailing edges are indicative of accumulation of Al in the Ag films at all annealing times.

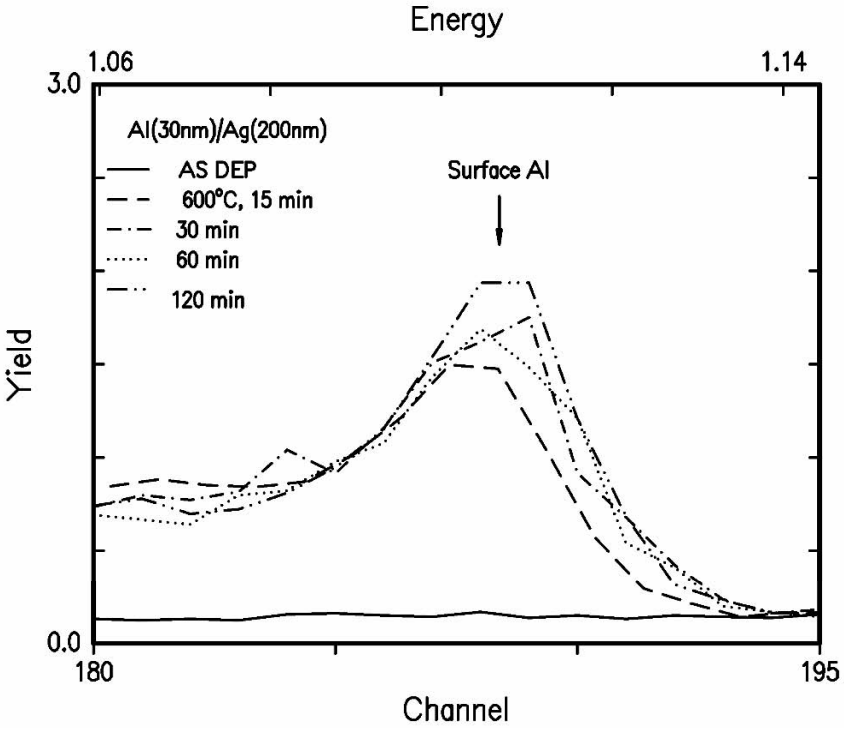

Figure 6.3. RBS spectra (2 MeV He^{+2}, 7° tilt) obtained from the Ag(200 nm)/Al(30 nm) bilayers on SiO_2 before and after annealing at 600°C in an NH_3 ambient for 15– 120 minutes. Only the Al surface peaks are shown [8].

The RBS spectra showed that in both bilayer structures: Ag(200 nm)/Al(20 nm) and Ag (200 nm)/Al (30 nm) a high residual Al concentration (~5 at.%) remains in the Ag films after the encapsulation process.

To show the presence of oxygen in the surface layer and to detect for any nitridation reaction between Al and N, RBS data were collected at 3.7 MeV (the resonance energy of N) with a tilt angle of 60°. Figure 6.4 shows the RBS spectra of the surface peaks for only the as-deposited Ag(200 nm)/Al(30 nm) bilayer and that annealed at 600°C for 120 minutes. At this high energy, the oxygen in the surface layer is more clearly visible. By stepping through the full range of N resonance energies, no nitrogen peak was present at the expected surface position for N, which suggests that the surface layer mainly consists of Al and O. Integration of the Al and O peaks in Figure 6.4 yielded an Al-to-O ratio of 0.64.

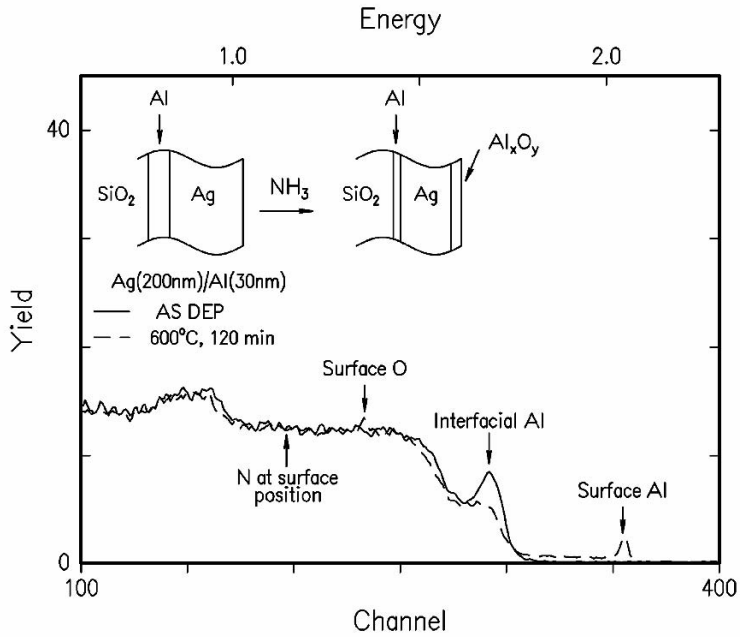

Figure 6.4. RBS spectra (3.7 MeV He^{+2}, 60° tilt) obtained from the Ag(200 nm)/Al(30 nm) bilayers on SiO_2 before and after annealing at 600°C in an NH_3 ambient for 120 minutes. Only the surface peaks and positions are shown [8].

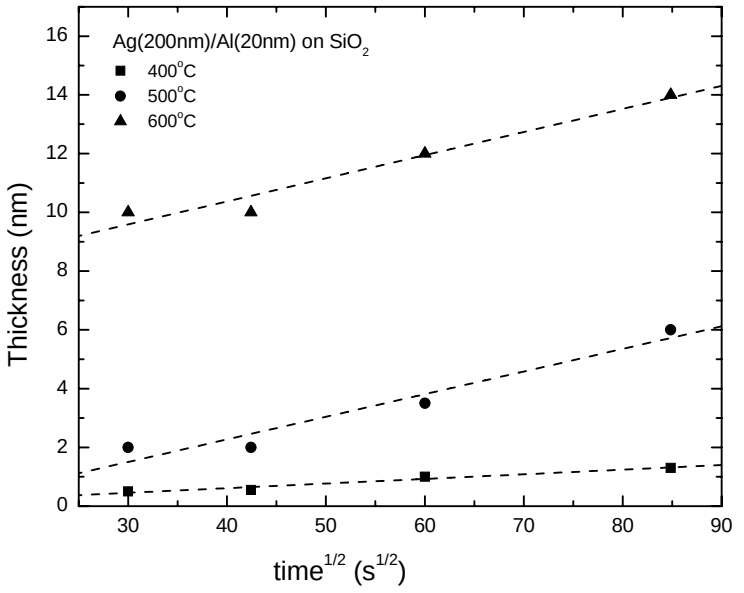

Figure 6.5. Al oxide thickness as a square root function of time for an Ag(200nm)/Al(20nm) bilayer system [8]

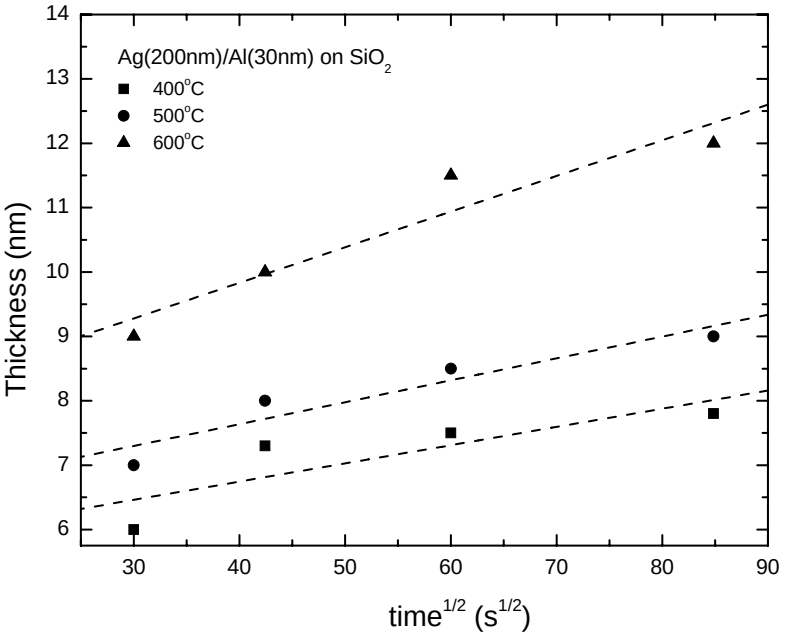

Figure 6.6. Al oxide thickness as a square root function of time for an Ag(200nm)/Al(30 nm) bilayer system [8]

6.1.3.2 Growth Kinetics of Oxide Surface Layer

In order to investigate the growth kinetics, the thickness of either aluminum or silver was changed. The influence of the initial Al thickness on the oxide growth kinetics was studied by considering the following two bilayers structures: Ag(200 nm)/Al(20 nm) and Ag(200 nm)/Al(30 nm). The Al_xO_y thickness (x) derived from the RBS data presented in the previous sections was plotted as a function of the square root of annealing time ($t^{1/2}$) for the range 15 to 120 minutes (Figures 6.5 and 6.6). Note the square root of annealing time is expressed in seconds in Figures 6.5 and 6.6. The plots of thickness (x) versus square root of time are straight lines, which imply that the oxide growth follows a parabolic growth behavior (x^2~t). In Figure 6.5, the slopes of the 500 and 600°C are almost parallel compare to the 400°C anneal.

For the thicker Al(30 nm), the lines are almost all parallel to each other (Figure 6.6). The diffusion coefficient D for the different bilayers Ag(200 nm)/Al(20 nm) and Ag(200 nm)/Al(30 nm) systems annealed at different temperatures were determined by taking the squares of the slopes of the plots in Figures 6.5 and 6.6. The results of these diffusion coefficients are given in Table 6.1 and reflect the behavior of the plots of thickness versus time$^{1/2}$. The diffusion coefficient increases as a function of temperature and is the highest for the 600°C anneal. It was found that the growth rates are much higher in Ag(200 nm)/Al(20 nm) than those in Ag(200 nm)/Al(30 nm) bilayers.

Table 6.1. Effect of temperature on the rate constants in the Ag/Al bilayer system for annealing times greater than 15 minutes [8]

Temperature (°C)	Diffusion coefficient D (10^{-21} m^2/s) of Al oxide	
	Ag(200 nm)/Al(20 nm)	Ag(200 nm)/Al(30 nm)
400	0.25	0.80
500	5.78	1.59
600	6.18	3.06

Figure 6.7 is a plot of the logarithm of the growth rate versus the reciprocal of temperature for two different Ag/Al bilayer systems. The two straight lines in Figure 6.7 are linear fits of the experimental data in Table 6.1. Based on the least square fit of the slopes in Figure 6.7, the activation energy (E_a) was determined from the Arrhenius plots. The activation energy is E_a = 0.25±0.15 eV for the Ag(200 nm)/Al(20 nm) bilayer and E_a = 0.34±0.05 eV for the Ag (200 nm)/Al(30 nm) bilayers and represents the energy barrier of the limiting step in the surface oxide formation process.

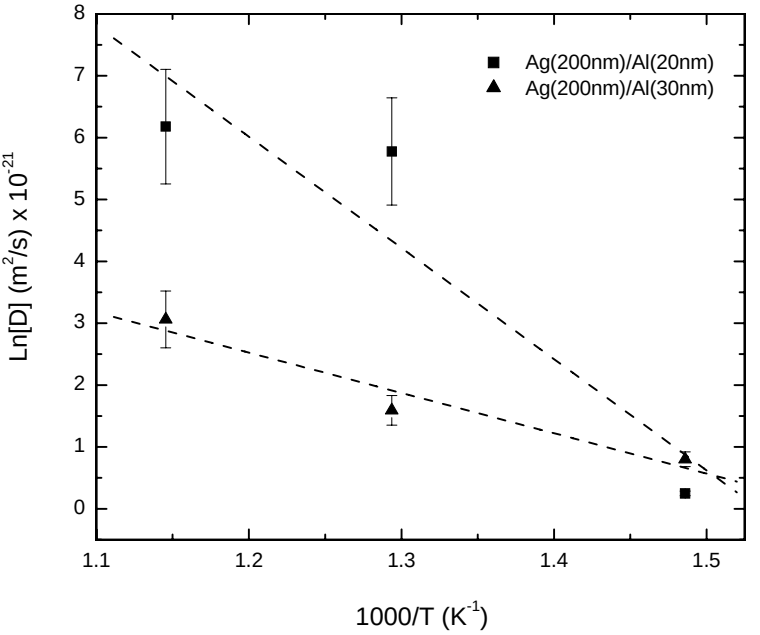

Figure 6.7. Arrhenius plots for Ag (200 nm)/Al (20 nm) and Ag (200 nm)/Al(30 nm) bilayer structures for different temperatures [8]

6.1.3.3 Factors Influencing the Transport of Aluminum Through the Silver

The focus of this section is to investigate the effect of factors such as Al thickness and trapping of Al in the silver on the transport kinetics and subsequent formation of the surface oxide. The curves in Figure 6.8a and b show the transport ratio $M(t)/M(\infty)$ of Al atoms through the Ag layer as a function of time for Ag(200 nm)/Al(20 nm) and Ag(200 nm)/Al(30 nm) bilayer structures annealed at different temperatures. The transport ratio based on RBS data was calculated using the amount of Al diffusing after time t, M(t) and the amount after infinite time, $t\rightarrow\infty$ defined as $M(\infty)$. It is observed that the transport ratio increases dramatically after

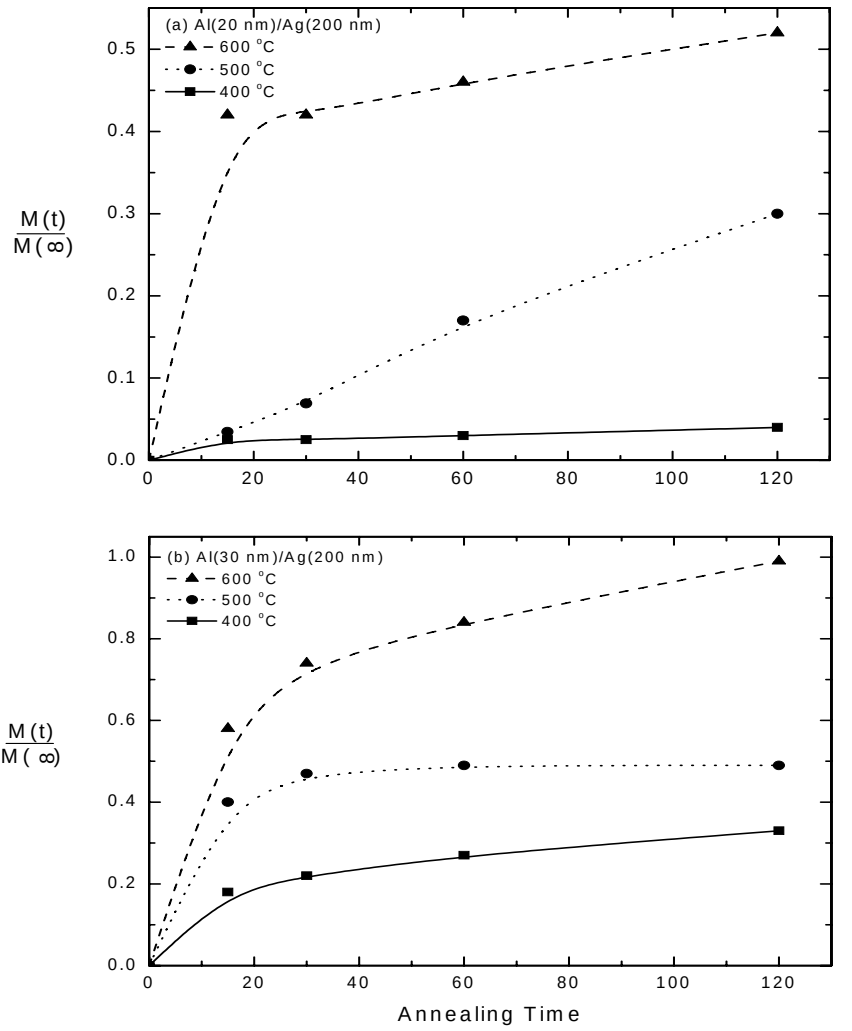

Figure 6.8. Transport ratio of Al atoms through the Ag layers annealed at different temperatures, (a) Al(20 nm)/Ag(200 nm) and (b) Al (30 nm)/Ag(200 nm) [8]

short anneals at all temperatures; but it remained almost constant after 15–120 minutes for 400°C anneals.

For the 500°C anneal, the Al transport ratio shows a linear increase to a maximum value of ~0.3 (Figure 6.8a). By increasing the Al thickness to 30 nm (Figure 6.8b), the experimental data shows that annealing in the temperature range 400–600°C for times between 15 and 120 minutes; the transport ratio of Al outdiffusion almost shows the same behavior for all temperatures; that is a rapid increase at short times followed by a plateau-like behavior.

At 600°C, the Al transport ratio takes longer to reach plateau-like behavior. For the different thicknesses, the data shows the same behavior for annealing temperatures ≥600°C.

The plot in Figure 6.9 shows the profiles for the residual Al and O concentration in Ag as a function of temperature for the Ag(200 nm)/Al(20 nm) and Ag(200 nm)/Al(30 nm) bilayers structures, respectively. From Figure 6.9, it follows that for a thin initial Al thickness (20 nm) the residual O mimics the Al; it displays a very slow increase with temperature.

For the thicker Al, the percentage of residual Al increases linearly up to about 400°C, whereafter it flattens to some constant value ~6.2 at.%. The percentage of O, however, increases almost linearly with temperature for the thicker Al(30 nm) layer.

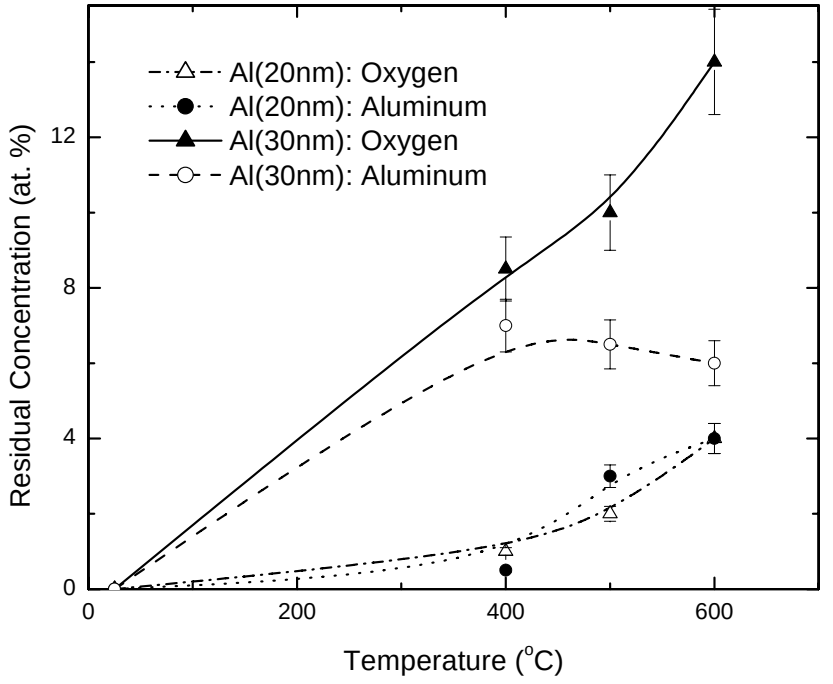

Figure 6.9. Plot of residual Al and O concentration in Ag layer as a function of annealing temperature [8]

6.1.4 Discussion

6.1.4.1 Formation of Aluminum Oxide Surface Layer

By annealing a Ag/Al bilayer structure in an ammonia ambient, the Al segregates to the surface to react with residual O in the ambient to form an Al_xO_y layer on the surface of the Ag. For the temperature range (400–600°C) considered in this investigation, no nitridation reaction between Al and N was detected. Wang *et al.* only formed an oxynitride from annealing the Ag/Al bilayers structure in NH_3 at 725°C. The thermodynamic data supported these results since the Gibbs free energy for consumption of 1 mol of O to form Al_2O_3 at 725°C is much lower, ~606.079 kJ/mol (~6.292 eV/Al atom), than that of N to form AlN, ~217.923 kJ/mol (~2.262 eV/Al atom). From the resonance data, it was shown in Figure 6.4 that the Al/O ratio is ~0.64 which points to the formation of Al_2O_3. Previous studies [6] showed that for Ag/Ti bilayers annealed in an NH_3 ambient at temperatures 300–700°C, TiN(O) encapsulation films are formed at the surface instead of Ti-oxide. The large negative heat of formation of TiO_2 (222–365 kJ/mol) compared to that of TiN (169 kJ/mol) is compensated by the partial pressure of NH_3 relative to that of O_2, leading to nitride rather than oxide formation.

The smaller thermal decomposition energy of NH_3 (432 kJ/mol) compared to N_2 (942 kJ/mol) makes it possible to form Ti-nitride at relatively lower temperatures. The data indicate that the amount of Al that segregates to the surface depends on the annealing temperature and annealing time. At higher temperatures and times, more Al moves to the free surface. A high residual Al, however, remains in the Ag(200 nm)/Al(20 nm) and Ag(200 nm)/Al(30 nm) structures after annealing at temperatures up to 600°C for times 15–120 minutes. This high level of residual Al is believed to be due to trapping of the aluminum in the Ag film.

6.1.4.2 Growth Kinetics of Oxide Surface Layer

The results obtained from the kinetics study suggest a parabolic growth behavior, which implies that the diffusion of the reaction species is the process governing the oxidation reaction. That is, the growth is governed by the diffusion of Al through the Ag layer. Due to the parabolic ($x \sim t^{1/2}$) behavior of the growth kinetics, the oxide growth is diffusion-controlled. Based on the data in Table 6.1, it follows that the diffusion coefficient is higher for the Ag(200 nm)/Al(20 nm) bilayers than that of the Ag(200 nm)/Al(30 nm) bilayer. The activation energies are 0.25 eV for Ag(200 nm)/Al(20 nm) and 0.34 eV for Ag(200 nm)/Al(30 nm) structures. These values of the activation energies are in agreement with that reported in literature (0.3–0.44 eV) [2]. Due to the fact that there is no significant difference in the activation energies for the two different thicknesses, it seems that the activation energy is approximately independent of the thickness.

6.1.4.3 Factors Influencing the Transport of Aluminum Through Silver

Wang *et al*. [5] reported that the segregation of Al in Ag/Al system annealed in an NH_3 ambient is influenced by the following factors: the chemical affinity between Al and Ag, the formation of a solid solution, intermetallic compound formation, a competition between the trapping of Al by the Ag and the diffusion of Al to the reaction surface, and the interfacial energy barrier between the newly formed Al oxide barrier and the underlying Ag layer. Based on these factors, they formulated a model to explain the transport of Al through Ag and derived an expression for the transport ratio M(t)/M(∞), given by the following equation [5]:

$$\frac{M(t)}{M(\infty)} = 1 - \sum_{n=1}^{\infty} \frac{2L^2 \exp[-\beta_n^2 Dt / l^2 (R+1)]}{\beta_n^2 (\beta_n^2 + L^2 + L)} \tag{6.1}$$

where, βtanβ = L are the positive roots of the equation, $L = (l\alpha / D)e^{-(\Delta E / k_b T)}$ is a dimensionless parameter, α is a constant of proportionality with units of velocity (cm/s), *l* is the thickness of Ag; T is the temperature and k_b is Boltman's constant. R is a constant, which accounts for the chemical effects between the trapped Al and Ag; depends on the diffusion process and was chosen to be 500 to fit the experimental data. One of the fundamental assumptions made in the derivation of the model is that the customary diffusion equation be modified as given in Equation 6.2 [5], to (a) account for the accumulation of Al at the Ag/Al-oxide interface, and (b) assume constant self-diffusivity of Al (D) instead of grain boundary diffusivity.

$$\frac{\partial C}{\partial t} = \frac{D}{R+1} \frac{\partial^2 C}{\partial x^2} \tag{6.2}$$

The constant R = S/C, where S = trapped Al concentration and C = concentration of the free diffusing Al atoms. Complete details about the assumptions and derivations of Equation 6.2 are given in [5]. The theoretical results calculated from the Equation 6.1 are depicted in Figure 6.10 for two different Ag/Al bilayers thickness.

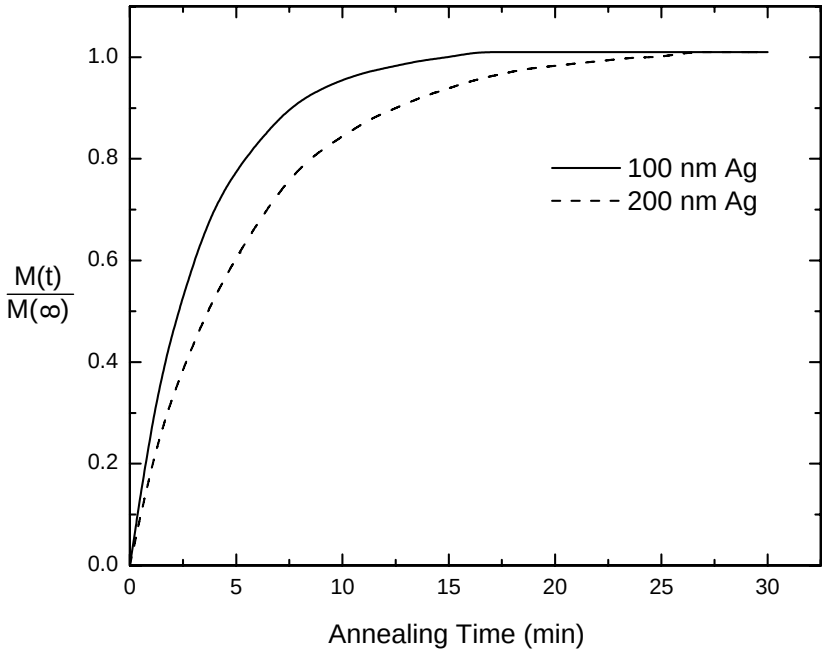

Figure 6.10. Theoretical calculated plot of the transport ratio of Al atoms through the Ag layers for different thicknesses: 100 nm (solid line) and 200 nm (dashed line) [5].

At higher temperatures, the transport ratio for different thicknesses follows the theoretical model. For the thicker Al(20–30 nm) films, a lower transport ratio was obtained than the theoretical curves. The lower transport ratio in this study compared to the calculated curves is attributed to the higher residual Al concentration in the Ag. The higher residual Al is a direct consequence of the increased trapping of Al in the Ag, which in turn is a result of the reduction of SiO_2 into free Si and O. For thin Al layers ~8 nm, the reduction of SiO_2 by Al can be neglected. The results in the present study suggest that for thicker Al (20–30 nm) films the reduction of SiO_2 has to be taken into account since it has an effect on the trapping of Al in the silver, in the sense that the Al reacts with freed O. The reduction of SiO_2 by Al is governed by the following reaction and enthalpy data:

$$4Al + 3SiO_2 \rightarrow 2Al_2O_3 + 3\ Si,\ \Delta H = -658\ kJ/mol \tag{6.3}$$

The oxygen freed by the reduction of SiO_2 confines the Al inside the Ag and hence is in direct competition with the surface reaction given by:

$$4Al + 3O_2 \rightarrow 2Al_2O_3,\ \Delta H = -1675\ kJ/mol \tag{6.4}$$

As a result of the reaction between the diffused Al and freed O, some Al are trapped inside the Ag instead of being available for the surface reaction. The presence of O in Ag layer explains the lower backscattering yields of the Ag signal of the annealed samples compared to the as-deposited ones. The larger trapping of Al in Ag suggests a greater value of R than that used in the theoretical model calculations.

According to Equation 6.1 if R increases the transport ratio, $M(t)/M(\infty)$, decreases, which explains our lower ratio. The larger trapping factor is due to the presence of O in Ag and implies an increased barrier to Al transport through the Ag. Figure 6.11 depicts the effect of the increased barrier on the Al transport through the Ag. The dotted line is the barrier height based on results obtained from the studies of the thin Al (~8 nm) interlayer and where the reduction of SiO_2 is neglected [5]. This model explains the kinetics of Al diffusion through Ag as a combination of a competitive behavior between the diffusion in Ag and the trapping of Al atoms at the Ag/Al oxide interface. The increased barrier as a result of the increased trapping of Al results in less Al diffusion to the surface and hence thinner Al oxide layers despite thicker aluminum interlayers.

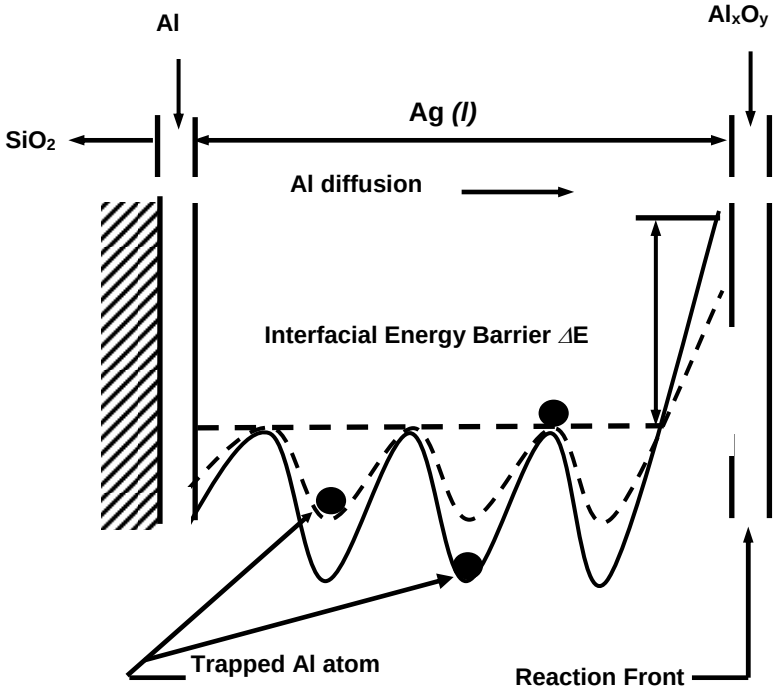

Figure 6.11. Schematic representation of the diffusion model of Al through Ag [5]

6.1.5 Conclusions

In this study Al_2O_3 encapsulation of Ag was successfully obtained by annealing a Ag(~200 nm)/Al(~20–30 nm) bilayer in a flowing NH_3 ambient at temperature between 400 and 600°C, for times 15–120 minutes. It is believed that an Al-oxynitride as a result of the nitridation of Al will only be formed when Ag/Al bilayers are annealed in NH_3 at temperatures >600°C. The kinetics of Ag/Al bilayers was studied to understand the factors influencing the transport of Al through Ag. The aluminum oxide formation follows a $t^{1/2}$ dependence implying a diffusion-controlled mechanism. To form a surface oxide for the Ag (200 nm)/Al(20 nm) and Ag(200 nm)/Al(30 nm) structures, an activation energy between 0.25 and 0.34 eV was obtained. The Al thickness has almost no significant influence on the activation energies.

A larger trapping factor was obtained for the thicker Al due to the reduction of the underlying SiO_2 substrate. The larger trapping factor results in a lower transport ratio $M(t)/M(\infty)$. The O freed during the reduction of SiO_2 ties up the Al and causes a larger barrier to the Al available for reaction at the surface to form the Al-oxide passivation layer. It is therefore evident that the thicker Al layers (20–30 nm) do not affect the kinetics in terms of the activation energy but has a significant influence on the trapping of Al as a result of the reduction of the SiO_2 substrate. The increased trapping leads to undesirable high residual Al levels, which is detrimental to the electrical properties of the Ag metallization.

Previous studies [7] have shown that the accumulated Al concentration dictates the resistivity of the silver films and that the resistivity increases with the amount of Al that remains in the Ag film after annealing. It is, therefore, desirable to use Al interlayers < 10 nm for encapsulation of Ag, because in this case the residual Al is lower and resistivities comparable with bulk values of Ag can be obtained at ~700°C [4, 8].

6.2 Effect of Metals and Oxidizing Ambient on Interfacial Reactions

6.2.1 Introduction

Thin film metallurgies have been of importance in many areas of technological significance, including semiconductor devices, surface coating, interface metallurgy, and corrosion resistance. The interactions occurring in the metal–metal or metal–silicon systems therefore dictate the stability and properties of these systems. Among the factors that affect thin film interactions, *i.e*. provide the driving forces, is the ambient in which the thin film resides during annealing or operation of the structures.

Interest in metals such as Ag, Au and Cu in metallization schemes for integrated circuit technology necessitates the investigation of the stability of these metals when in contact with silicon [1, 3, 9–10]. It has been shown that Cu reacts

with silicon at temperatures as low as 200°C to form the silicide, Cu_3Si [10]. When this structure is left at room temperature, a 1 mm-thick oxide grows at the Si–Cu_3Si interface. Therefore, in the Si/Cu_3Si system silicon oxidation occurs at room temperature compared to thermal oxidation, which requires temperatures between 1000 and 1200°C to form oxides of appreciable thickness. The Cu_3Si catalyzes the oxidation of silicon [9].

In pioneering work, Hiraki *et al*. [11], reported on the effect of Au on the low temperature oxidation of silicon. The interaction between metals (Au and Ag) and silicon in an oxidizing ambient is investigated.

6.2.2 Experimental Details

Gold and silver layers of thickness varying from 50 to 150 nm were deposited on Si(100) substrates via electron-beam evaporation. The base and operating pressure were 10^{-7} and 10^{-6} Torr, respectively. All anneals were performed in a Lindberg single-zone quartz tube furnace under a flowing O_2 ambient for times varying from 30 to 120 min at temperatures ranging from 200 to 350°C.

Rutherford backscattering spectrometry (RBS) was used to determine the composition and thickness of the different layers. Scanning electron microscopy (SEM) and transmission electron microscopy (TEM) were used to evaluate the surface morphology and microstructure of the Au/Si and Ag/Si systems, respectively. The SEM was operated at 10 kV at a working distance of 5 mm to obtain surface information at high resolution. All XTEM images were taken at 200 keV.

6.2.3 Results

Figure 6.12 compares the RBS spectrum of an as-deposited Au(50 nm)/Si(100) structure with that annealed at 350°C for 60 minutes in an O_2 ambient. During annealing in the oxidizing ambient, an intermixed ‘‘Au+Si’’ is formed and silicon is freed to diffuse to the surface. At the surface the diffused silicon reacts with the oxygen to form a silicon oxide. The presence of the oxide is confirmed by the shift of the Au signal to lower energies and the oxygen and Si surface peaks.

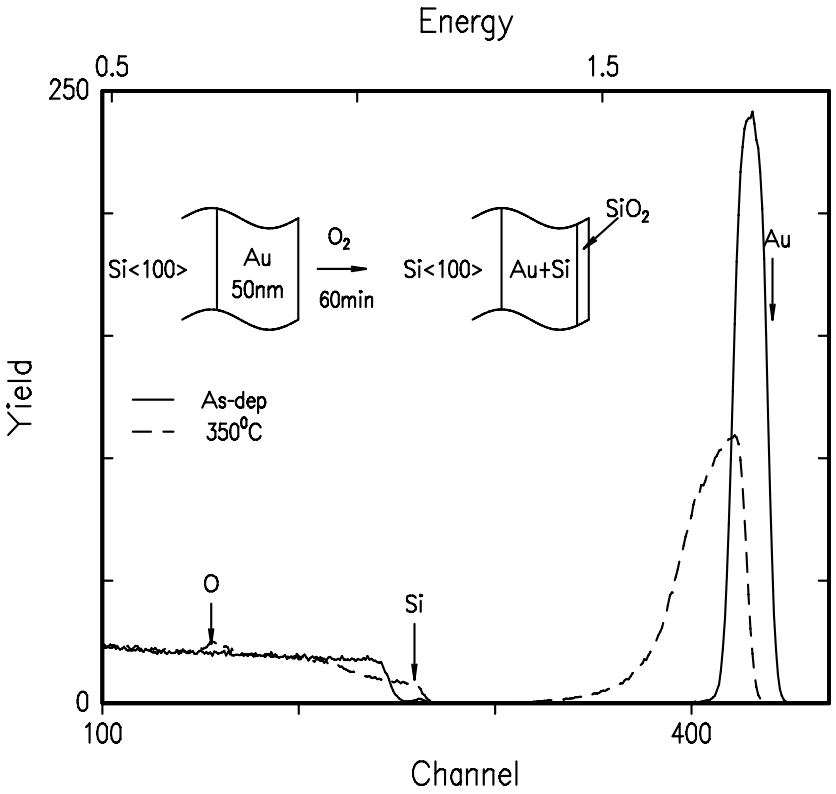

Figure 6.12. RBS spectrum of an as-deposited Au(50 nm)/Si(100) structure (solid line) with that (dashed line) of a structure annealed at 350°C for 60 minutes in an O_2 ambient [13]

RUMP simulation of the annealed spectrum suggests an oxide thickness of ~132 nm. Annealing of the Au(150 nm)/Si(100) structure at 350°C for 60 minutes resulted in the formation of a silicon oxide of 115 nm (Figure 6.13). Compared to the data presented in Figure 6.12, the RBS spectrum in Figure 6.13 indicates that the entire Au has not intermixed with the silicon. The layer immediately below the surface oxide is an Au rich layer. For the same annealing conditions, *i.e.* temperature and time, a slightly thinner oxide is formed for the thicker (150 nm) Au layer.

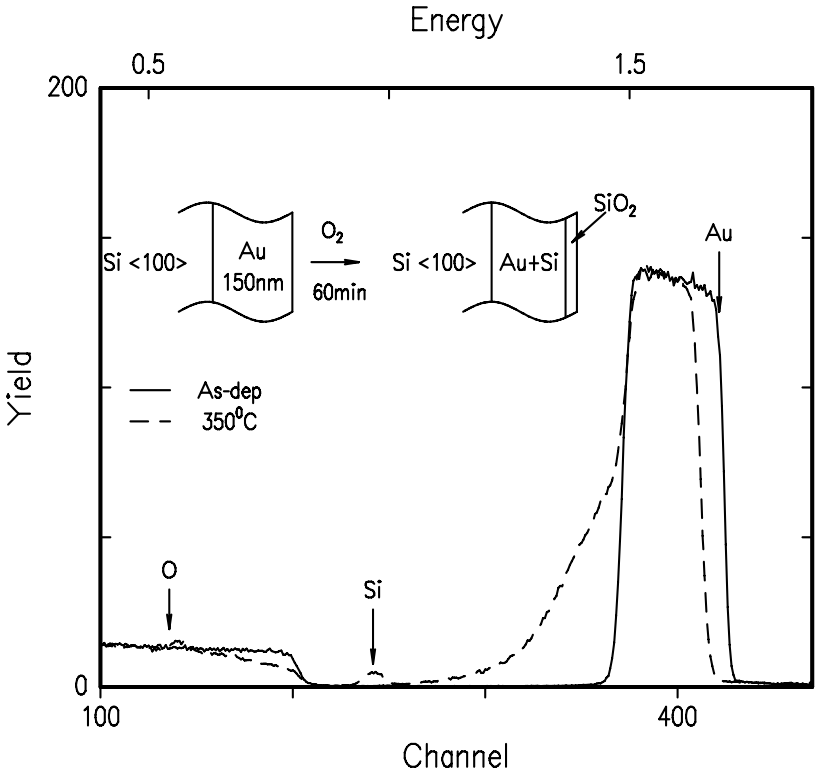

Figure 6.13. RBS spectrum of an as-deposited Au(150 nm)/Si(100) structure (solid line) with that (dashed line) of a structure annealed at 350°C for 60 minutes in an O_2 ambient [13]

Cross-sectional transmission electron microscopy (XTEM) analysis was performed to supplement the RBS analysis. The XTEM analysis indicated that the annealing resulted in a multilayered structure, namely a silicon oxide (~132 nm), an intermixed Au+Si layer and the underlying silicon substrate. It has to be pointed out that due to the porous nature of the oxide the Ti of the capping layer indiffused into it, therefore, the final thickness of the oxide extends to the surface. In agreement with the RBS results, the XTEM analysis showed that during annealing the entire Au layer is consumed to form the intermixed Au+Si layer. Scanning electron microscopy analysis revealed that the silicon oxide formed at the surface is porous and non-uniform in thickness. Figure 6.14 shows the RBS spectra of the as-deposited Ag(150 nm)/Si(100) structure and that annealed at 350°C for 60 minutes in O_2.

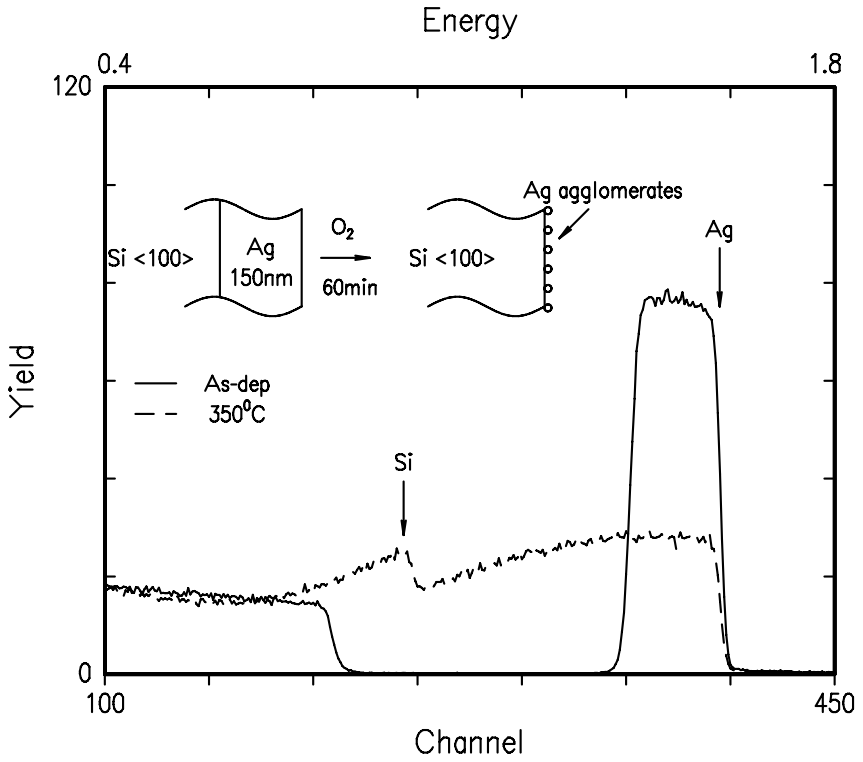

Figure 6.14. RBS spectrum of an as-deposited Ag(150 nm)/Si(100) structure (solid line) with that (dashed line) of a structure annealed at 350°C for 60 minutes in an O_2 ambient [13]

The broad tail of the annealed spectrum suggests that the Ag does not intermix with silicon, and no silicon is released to form a surface oxide as in the case of the Au/Si system, instead silver agglomerates are formed. The formation of the agglomeration is confirmed by the fact that the RBS spectrum of the annealed sample shows both silicon and silver at the surface. The RBS data was further supported by the SEM analysis, which shows the silver agglomerates, a discontinuous silver film is formed on the Si substrate after annealing the Ag/Si in an O_2 ambient.

6.2.4 Discussion

Upon annealing the Au/Si structure in an oxidizing ambient, the presence of the Au results in the relaxation of the metal–silicon interfacial energy and leads to the formation of an intermixed Au+Si layer adjacent to the silicon substrate. Silicon atoms can be ejected from the interface and migrate through the Au layer to the surface to form a silicon oxide layer. It has to be pointed out that the solid solubility of Si in gold is very low [12].

The observed enhanced outdiffusion of silicon through gold is often attributed to the formation of an oxide on the Au surface when annealed in an oxidizing

ambient. The oxide is thought to act as a sink, which becomes the driving force for the enhanced outdiffusion. Furthermore, the outdiffusion of Si and its accumulation on the surface of Au is related to the surface energy of the system.

In view of the above mentioned, the surface potential model is proposed to explain the diffusion of Si through Au and the subsequent surface oxide formation.

According to the surface potential model, the major contributing factors are the overcoating metal (Au) and the type of ambient present [1]. The overcoating metal determines the difference in electronegativity (or ionicity), which in turn is a measure of the bonding between the two materials, Au and silicon. On the other hand, the type of ambient gas, alters the surface properties of the metal upon absorption and results in an increase or decrease in the work function of the metal. Table 6.2 summarizes the effects of these factors.

In terms of the model, the Au–Si interaction can be described as:

$$Au_x + Si_y \rightarrow Au_x\text{–}Si + Si_{y-1} \tag{6.5}$$

$$Au_x\text{–}Si \rightarrow \text{outdiffusion of Si; or alloy formation; etc:} \tag{6.6}$$

Table 6.2. The effect of electronegativity difference, and ambient-induced work function on diffusion of silicon [13]

System	Electronegativity difference (ionicity)	Work function	Effect
Au/Si	2.4 (Au)–1.8(Si) = 0.6	Reduced (negative surface potential)	Enhanced outdiffusion of Si
Ag/Si	1.9(Ag)–1.8(Si) = 0.1	Little effect	Little outdiffusion of Si

According to Table 6.2, the overcoating metal, Au is more electronegative than Si, which gives a partial ionic bond in the Au_x–Si complex as $Au_x\delta^-$–Siδ^+. It has been reported that dry oxygen induces a negative surface potential on Au. The combination of the higher electronegativity of gold and ambient induced negative potential on Au brings about reduction in the work function of the gold and therefore making the Reactions 6.5 and 6.6 favourable.

Based on the surface potential model and the data given in Table 6.2, an oxide will only form on the surface of a Au overlayer and not Ag. The ionicity of the Ag/Si bond is less than 1/10 that of the Au/Si due to the smaller electronegativity of silver. Therefore, the ambient will have a much smaller effect in the case when silver is used as the overcoating metal. In support of this model, it has been shown that a hydrogen ambient induces a positive surface potential on Au resulting in an increase in its work function by 0.18 eV. This increase in work function is unfavourable to Reactions 6.5 and 6.6 and hence reduced Au–Si interactions in the presence of this ambient.

The released silicon diffuses through the Au along grain boundaries. This is consistent with the fact that after heating the Au/Si system to temperatures above

its eutectic point, further annealing in an oxidizing ambient no longer gives outdiffusion of silicon [11]. Crystallization takes place during annealing, which greatly reduces the number of grain boundaries in the annealed samples compared with the polycrystalline films in the as-deposited state.

Under the same annealing conditions (temperature and time) the 50 nm-thick Au layer compared to the 150 nm, forms a slightly thicker oxide, due to the longer diffusion path for the thicker Au overlayer [13].

6.2.5 Conclusions

In 30 years, the Hiraki *et al*. [11], conclusion has not changed: ''When a single crystal substrate of silicon is covered with evaporated gold and heated at relatively low temperatures (100–300°C) in an oxidizing atmosphere, a silicon-dioxide layer is readily formed over the gold layer''. This investigation reaffirmed the Au/Si results [13]. No oxide layer is formed on Ag/Si layers annealed under the same conditions. The Ag forms a discontinuous layer. The results obtained from the Au/Si and Ag/Si correlate well with the surface potential model.

6.3 Silver Metallization on Silicides with Nitride Barriers

6.3.1 Introduction

The attractive properties of Ag, such as its low resistivity coupled with increased resistance to electromigration, have propelled some exciting research aimed towards its use as a future interconnect material in the next generation of ULSI devices [14]. Early studies of the Ag/Si interface have shown the morphological stability to be poor since it is prone to agglomeration upon annealing of only 200 ^{o}C. The addition of a thin interposing Au layer between Ag and Si has improved the stability of the interface by forming an intermixed region, which lowers the interfacial energy of the original Ag/Si system. Several authors have investigated the behavior of Ag at the SiO_2/Si interface [15]. Results [16], suggest that diffusion of trace amounts of Ag occur in the Ag/$CoSi_2$/Si and Ag/NiSi/Si systems. To combat such problems, several barriers for Ag inter-diffusion have been proposed; titanium, titanium nitride, tantalum and tantalum nitride are typical barriers used with copper and silver [17]. Other barrier layers such as aluminum oxynitrides were studied as well [2, 4, 18–19].

Working with Ag it was quickly noticed that its diffusion into substrates and dielectrics posed challenges to be overcome. Mitan *et al*. investigated the thermal stability of Ag at the $CoSi_2$ and NiSi interfaces in conjunction with a Ti-O-N diffusion barrier [20]. The discussion is divided into two sections, $CoSi_2$ and NiSi. Each section discusses the behavior of Ag and barrier layer with respect to the silicide being examined.

6.3.2 Experimental Details

6.3.2.1 $CoSi_2$ and Ti-O-N Preparation

Test grade silicon (100) p-type wafers, 10 to 20 Ω resistance, were cleaned in a piranha bath containing sulfuric acid and hydrogen peroxide at 100°C. The native oxide was subsequently removed by dilute hydrofluoric acid. Immediately after cleaning the wafers were loaded into a Varian electron-beam deposition chamber.

A 60 nm thin film of Co metal was deposited on a clean silicon wafer at a base pressure of 1×10^{-6} Torr. A 5 nm capping layer of silicon was deposited over the Co in the same chamber without breaking vacuum. This capping layer protected the cobalt from reacting with oxygen while transferring samples from the deposition chamber to the anneal furnace. The formation of $CoSi_2$ was accomplished by annealing in a rapid thermal annealer (RTA) in two steps. The initial heat treatment step at 500°C for 40 seconds was followed by 750°C for 30 seconds. All rapid thermal anneal furnace treatments were performed under a nitrogen atmosphere. In between heat treatments excess metal was removed by dilute nitric acid. This self-aligning approach yielded very smooth polycrystalline silicide layers. The silicided silicon wafer was then coated with 20 nm of Ti-O-N using DC sputtering. The base pressure in the sputtering chamber was 1.3×10^{-7} Torr. N_2 and Ar gas flow rates were set at 6 sccm, respectively. The film was sputtered at a power of 300 W. After Ti-O-N deposition, the sample was again loaded into the Varian electron-beam deposition chamber for Ag deposition. With a base pressure of 1×10^{-6} Torr, 100 nm of Ag was deposited on top of the Ti-O-N/$CoSi_2$ layers. The silver coated sample was sectioned into small samples and then annealed at 100°C increments starting from 100°C up to 700°C for 30 minutes each. One additional sample was annealed at 650°C to give good comparison with previous work. These thermal stability tests were performed in a vacuum furnace at a pressure of 1×10^{-8} Torr.

6.3.2.2 NiSi and Ti-O-N Preparation

Using cleaned Si wafers as described in $CoSi_2$ preparation section, a 50 nm film of Ni metal was deposited at a base pressure of 1×10^{-6} Torr followed by the immediate deposition of a silicon cap of 5 nm. The Si cap layer served to protect the Ni from air during transport to the anneal furnace. The formation of NiSi was accomplished by annealing in RTA at 400°C for 30 minutes under flowing N_2 ambient. The RTA anneal procedure produced smooth single-phase polycrystalline NiSi [19]. The silicided silicon wafer was then coated with 20 nm of Ti-O-N using DC sputtering. The base pressure in the sputtering chamber was 1.3×10^{-7} Torr. N_2 and Ar gas flow rates were set at 6 sccm, respectively. The film was sputtered at a power of 300 W. After Ti-O-N deposition, the sample was again loaded into the Varian electron-beam-deposition chamber for Ag deposition. With a base pressure of 1×10^{-6} Torr 100 nm of Ag was deposited on top of the Ti-O-N/NiSi layers. Thermal stability tests were identical to the $CoSi_2$ samples.

6.3.2.3 Ag/barrier/silicide/silicon Evaluation

All samples were analyzed by Rutherford backscattering spectrometry (RBS), X-ray diffractometry (XRD), optical microscopy, atomic force microscopy (AFM), and secondary ion mass spectroscopy (SIMS). Additionally, the Ag thin film resistance was checked by in-line four-point-probe (FPP) measurements. FPP measurements were made with a Keithley 2700 Multimeter using 100 mA of current. RBS spectra were generated using 2 MeV and 3.7 MeV alpha particles. Sample and detector were in the Cornell geometry arrangement such that the backscatter detector is directly below the incident beam; the incident beam and the scattered beam are in a vertical plane. In this geometry the sample normal is not in that vertical plane. The samples were tilted 7^o off beam axis to avoid channeling, and a scattering angle of 172^o was used for spectra collection. RBS spectra were simulated using RUMP software.

Ag morphology micrographs were generated with optical microscopy. Sample surface scans were acquired on a Digital Instruments Dimension 5000 (AFM) in tapping mode to capture image using Nanoprobe TESP tips. SIMS depth profiles were generated using a Cameca IMS-6f secondary ion microanalyzer. Profiles were generated using 10 nA of beam current of Cs^+ at 10 KeV in a chamber at vacuum of 1×10^{-7} Torr. The beam was rastered over 250 μm. Sample bias was set to +5 KV giving net ion incident energy of 5 KeV. These instrument parameters are used in a technique known as, Cs attachment SIMS, which helps minimize matrix effects as well as decrease clustered molecular interference. The goal here was to discover if any Ag had migrated into the silicide films through the diffusion barrier; therefore, Ag was removed prior to SIMS profiling by immersing samples in a bath of 1:1 nitric acid and water for 30 seconds.

6.3.3 Results and Discussions

6.3.3.1 Ag/Ti-O-N/$CoSi_2$/Si

The thermal behavior of the Ag films was first analyzed by Rutherford backscattering spectrometry (RBS). Figure 6.15 shows the RBS spectra for the as-deposited Ag film on the Ti-O-N/$CoSi_2$/Si thin film structure. The simulation coincided with collected spectra, which gives a $CoSi_2$ thickness of 200 nm and a 100 nm thick Ag top layer. The Ti-O-N barrier was approximated at 50 nm using RUMP simulation and correlation of sputter deposition parameters. The discrepancy between the heights of the evaporated Ag film and that of the simulated film signals is likely due to inclusion of light elements in the Ag films, an artifact of the poor vacuum in the evaporation chamber. Figure 6.15 also compares the spectra of films annealed at 600^oC, 650^oC, and 700^oC against the as-deposited film. Spectra of the 600^oC and 650^oC profiles show a small rise in the trailing edge of the Ag peak together with drop in the overall Ag peak intensity. The Co signal reveals a slight forward shift from the as deposited spectrum. All of these changes can be attributed to morphology changes of the Ag film during the annealing process. The loss of Ag signal becomes pronounced when the films are annealed to 700^oC, which clearly shows a significant drop in the integral Ag signal.

For a pure example of Ag film agglomeration, a drop in the surface Ag peak would coincide with a trailing edge that makes up for the loss in the surface peak's initial integral counts. The trailing edge, which is not present in this RBS plot, would account for the formation of voids and an increase in the thickness of the resultant islands. The case presented here suggests the agglomeration of the Ag film may not be a possible reason of Ag film failure on Ti-O-N film. At this point, the voided film allows the Co and Si signals to move forward to their respective RBS surface peak energies.

Optical imaging analysis of the as-deposited and the annealed Ag films at 600, 650, and 700°C suggested that there is no significant increase in the surface height upon film voiding. This indicated that voids are not formed only by the process of agglomeration. Agglomeration results in the rough surface morphology due to hillock formation caused by diffusion of atoms. The voids are caused by the Ag film failure mechanism at elevated temperature since these voids are not found in as-deposited and low temperature annealed samples.

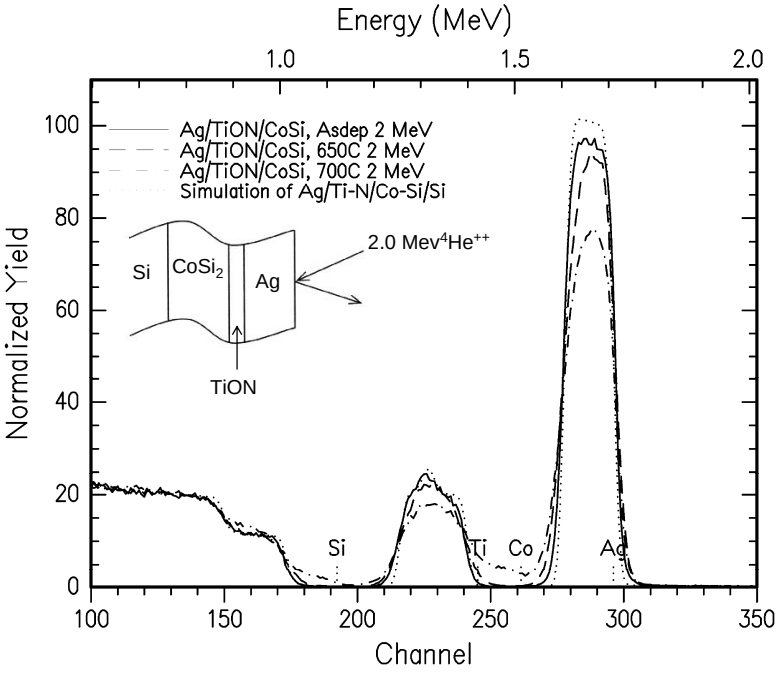

Figure 6.15. RBS 2 MeV spectra of Ag/Ti-O-N/$CoSi_2$/Si film structure of as-deposited and annealed samples at 600, 650, and 700°C [20]

To help to illuminate film roughness around a void before and after heating, AFM scans were taken to get an accurate indication of the surface roughness and step height changes. From AFM analysis it followed that the thin Ag film in its as-deposited form follows the topography of the Ti-O-N layer that it covers. The voids are most likely initiated by an agglomeration mechanism but can not account for the missing Ag.

Confirmation of crystalline phase changes was accomplished through XRD analysis. 2θ-θ scans performed of the as-deposited and 700°C anneal conditions did not reveal the presence of any unexpected compounds. Figure 6.16 shows two overlaid spectra. Figure 6.16a is the as-deposited Ag film on Ti-O-N/$CoSi_2$, followed by the 700°C anneal with film voiding (Figure 6.16b). All peaks were identified as belonging to $CoSi_2$ or Ag except substrate peaks (Si). No transformation of phases during film anneals were observed. No peaks were found corresponding to Ti-O-N due to the film's shallow thickness and lack of crystallinity.

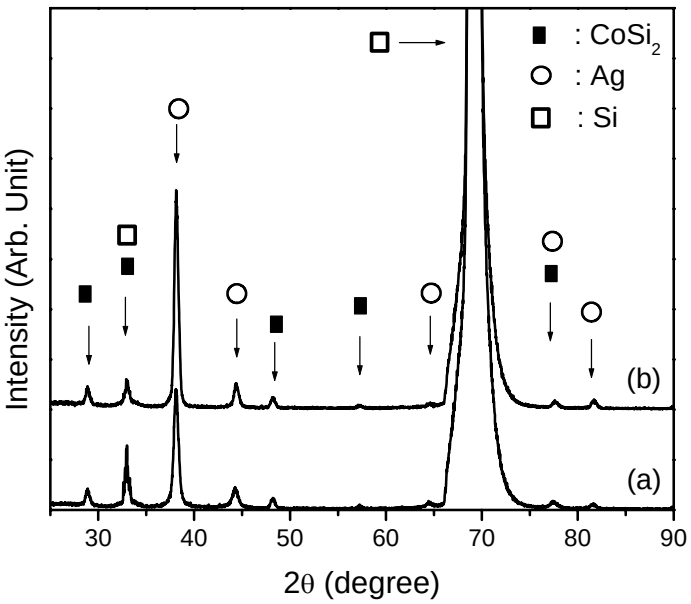

Figure 6.16. Overlaid XRD 2θ-θ scan data. (a) as-deposited Ag film on Ti-O-N/$CoSi_2$, (b) 700°C anneal of Ag on Ti-O-N/$CoSi_2$ [20].

6.3.3.2 Ag/Ti-O-N/NiSi/Si

Initial evaluation of annealed films is accomplished by RBS. The behavior of the Ag films on Ti-O-N/NiSi is similar to the Ti-O-N/$CoSi_2$ experiments. Figure 6.17 displays the RBS spectra of the as deposited condition, the simulation, and the higher temperature annealed films 600°C to 700°C. The simulation coincided with collected spectra from as-deposited sample, which gives a NiSi thickness of 270 nm and a 100 nm thick Ag top layer. The Ti-O-N barrier was approximated at 50 nm using RUMP simulation and correlation of sputter-deposition parameters. The discrepancy between the heights of the evaporated Ag film and that of the simulated film signals is likely due to inclusion of light elements in the Ag films caused by the poor vacuum in the evaporation chamber.

Upon Ag film breakup, the spectra shows that the Si and Ni signals have moved forward and the Ag peak has fallen by roughly 40%, indicating formation voids in the Ag film. Similar to the $CoSi_2$ case, the Ag does not agglomerate into islands of thicker films. Paralleling the $CoSi_2$ example, the Ni system does not show any long range trend (RBS) of surface height (ΔZ) increases leading to a similar conclusion. The voiding, most likely initiated by an agglomeration mechanism, can not account for the missing Ag.

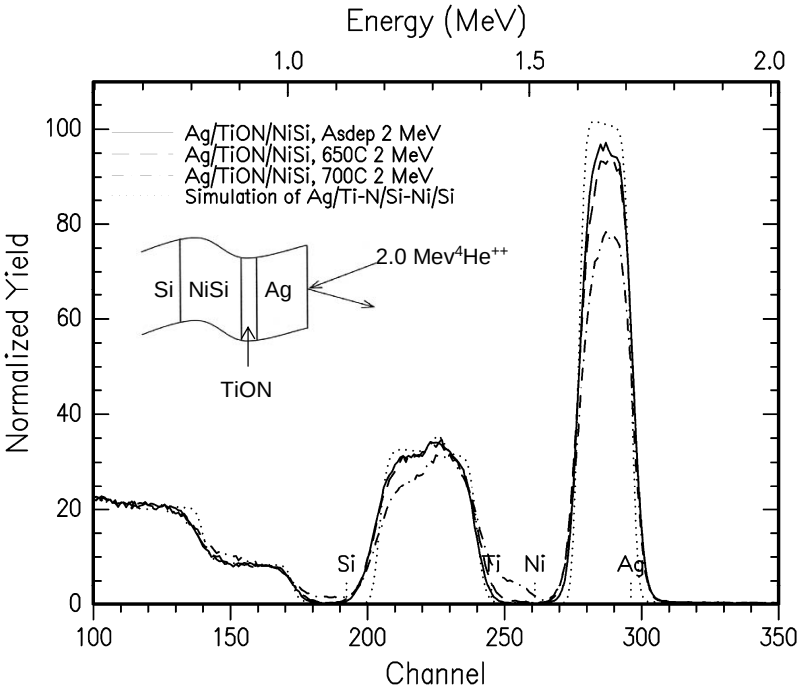

Figure 6.17. RBS 2 MeV spectra of Ag/Ti-O-N/NiSi/Si film structure of as-deposited and annealed samples at 600, 650, and 700°C [20]

Confirmation of crystalline phase changes was accomplished through XRD analysis. 2θ-θ scans performed on the as deposited and 700°C anneal conditions did not reveal the presence of any unexpected compounds. Figure 6.18 shows two overlaid spectra. Figure 6.18a is the as-deposited Ag film on Ti-O-N/NiSi, lower plot, followed by the 700°C anneal with film voiding, upper plot (Figure 6.18b). All peaks were identified as belonging to NiSi or Ag except Si substrate peaks. No transformation of phases during film anneals were observed. No peaks were found corresponding to Ti-O-N due to the film's shallow thickness and lack of crystallinity.

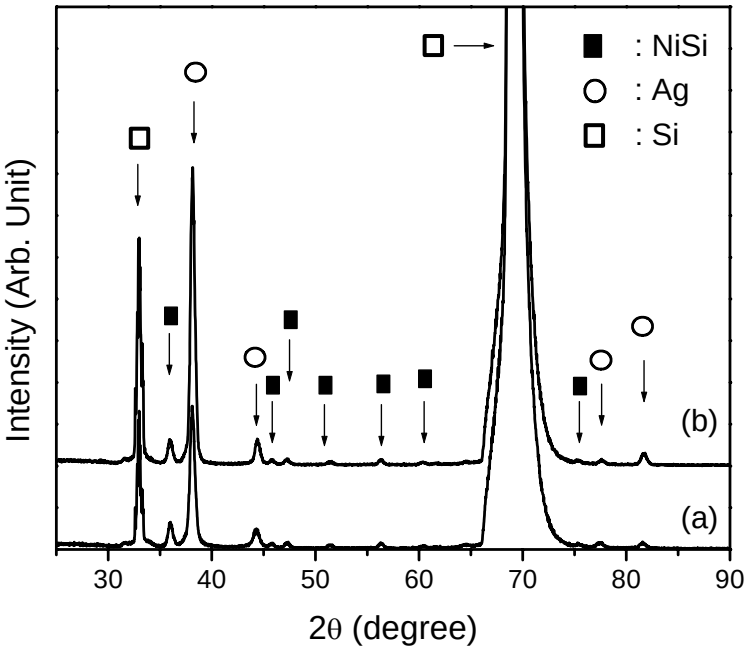

Figure 6.18. Overlaid XRD 2θ-θ scan spectra of (a) as-deposited Ag film on Ti-O-N/$CoSi_2$ and (b) the 700°C anneal of Ag on Ti-O-N/NiSi [20]

6.3.4 Conclusions

RBS results of the annealed Ag/Ti-O-N/silicide layers reveal the presence of stable silicides across the investigated temperature range. There were no phase changes observed in the films that XRD could detect throughout the temperature range. A similarity with both silicide scenarios seems to be the unusual failure mode of the Ag film. Upon film breakup, both examples show a behavior where the voids formed have smooth ridges, however, the step height increases at the edges do not account for the missing Ag. Some of the observed voids frequently have no significant ridge height increase and thus irregular vias form within the Ag film.

This effect is more pronounced with NiSi giving it almost no significant rise of the Ag trailing edge of its RBS plot. The overall success of the barrier layer below 500°C is eventually concluded via the SIMS profiles which indicate trace amounts of Ag segregating to the silicide/silicon interfaces through the Ti-O-N barrier [20].

From the experimental data shown in this study, it is thought that failures of Ag films on Ti-O-N/silicide/Si are caused by the combination of Ag film agglomeration and diffusion into underlying substrates. The mass loss of Ag film cannot only be explained by agglomeration process. From the SIMS analysis, it was revealed some amount of Ag has moved to the interface between Si and silicides. The electrical conductivity of the Ag films remained constant up to 600°C, a result that was independent of the Ag diffusion issue. Currently the use of $CoSi_2$ is widespread in the industry and NiSi is gaining ground due to its smaller consumption of Si during formation. The ability of Ag film survival up to 600°C is useful for many high temperature applications [20].

6.4 References

[1] D. Adams, T. Laursen, T. L. Alford, J. W. Mayer, Thin Solid Films, 308/309, 448(1997).

[2] Y. L. Zou, T. L. Alford, J. W. Mayer, F. Deng, S. S. Lau, T. Laursen, A. I. Amli, B. M. Ullrich, J. Appl. Phys. 82, 3321(1997).

[3] T. L. Alford, D. Adams, T. Laursen, B. Manfred Ullrich, Appl. Phys. Lett. 68, 3251(1996).

[4] Y. Wang, T. L. Alford, Appl. Phys. Lett. 74, 52(1999).

[5] Y. Wang, T. L. Alford, J. W. Mayer, J. Appl. Phys. 86, 5407(1999).

[6] D. Adams, B. A. Julies, T. L. Alford, J. W. Mayer, Thin Solid Films 332

[7] D. Adams, T. L. Alford, Mater. Sci. Eng., R. 40 (6), 224(2003).

[8] G. F. Malgas, D. Adams, T. L. Alford, and J. W. Mayer, Thin Solid Films 467, 267(2004).

[9] T. L. Alford, E. J. Jaquez, N. D. Theodore, S. W. Russell, M. Diale, D. Adams, J. Appl. Phys. 79 (4), 2074(1996).

[10] J. Li, J. W. Mayer, L. J. Matienzo, F. Emmi, Mater. Chem. Phys. 32, 390(1992).

[11] A. Hiraki, E. Lugujjo, J. W. Mayer, J. Appl. Phys. 43, 3643(1972).

[12] J. M. Poate, K. N. Tu, J. W. Mayer (Eds.), Thin Films–Interdiffusion and Reactions, Wiley/Interscience, New York, 1978.

[13] D. Adams, B. A. Julies, J. W. Mayer, T. L. Alford. Applied Surface Science 216, 163(2003).

[14] P. L. Rossiter, The Electrical Resistivity of Metals and Alloys, (Cambridge University Press, Cambridge, UK, 1987).

[15] K. Sieradzki, K. Baily, and T. L. Alford, Appl. Phys. Lett. 79, 3401 (2001).

[16] M. M. Mitan, T. L. Alford, Thin Solid Films 434, 258 (2003).

[17] T. L. Alford, P. Nyugen, Y. Zeng, J. W. Mayer, Microelectronic Eng. 55, 383(2001).

[18] Y. Zeng, Y. L. Zou, T. L. Alford, S. S. Lau, F. Deng, T. Laursen and B. M. Ullrich, J. Appl. Phys. 81, 7773(1997).
[19] B. A. Julies, D. Knoesen, R. Pretorius, D. Adams, Thin Solid Films 347, 201(1999).
[20] M. M. Mitan, H. C. Kim, T. L. Alford, J. W. Mayer, G. F. Malgas, and D. Adams. J. Vac. Sci. Technol. B 22(6), 2804(2004).

This page intentionally blank

7

Summary

7.1 Introduction

This monograph reviews bilayer and alloy techniques with Ti, Al and others to form adhesion layers and diffusion barriers. The temperature range of thermal stability is covered. During Ti and Al transport to form the encapsulating layers, the Ag films develop <111> texture. Integration with low-K dielectrics such as paralene has been demonstrated. Encapsulated Ag films have superior resistance to electromigration degradation.

7.2 Thermal Stability: Diffusion Barriers and Self-encapsulation

In view of the thermal stability issues associated with silver metallization a passivation layer and diffusion barrier are required to protect it from the fabrication environment, and an adhesion promoter is needed to enhance adhesion of Ag to the dielectrics.

Titanium–nitride is used in integrated circuit technology as a diffusion barrier and etch stop. It has low specific resistance when compared to TiW [1], which makes it particularly attractive in applications where device speed is critical. Furthermore, TiN has been found to suppress or prevent aluminum migration through $TiSi_2$ to the silicon substrate [2]. This makes TiN a viable material for thin-film diffusion or reaction barrier layer. Two common methodologies can be used to produce TiN, *i.e.* (1) reactive sputtering of titanium in a nitrogen ambient [3] and (2) titanium deposition and subsequent annealing in either nitrogen or ammonia

[2]. The reactive sputtering in the nitrogen ambient has suffered from an incomplete control of compositions since the sputter rate changes as a function of time. Therefore, we have focused on forming a TiN passivation layer in an ammonia ambient to encapsulate Ag films [4,5].

To accomplish both surface passivation and diffusion barrier/adhesion promoter functions in a single process step, it has been proposed to anneal Cu-refractory metal (Ti, Cr) alloy and bilayer structures on SiO_2 in an ammonia (NH_3) ambient to induce simultaneously a surface nitridation reaction and interfacial reactions [6]. This process has been applied to Ag-refractory metal systems and is schematically represented in Figure 7.1. The surface reaction results in the formation of a titanium–nitride encapsulation layer (labeled as "TiN_x") and a titanium-oxide/titanium-silicide ("$TiO/TiSi_y$") bilayer structure, which is a direct consequence of the interfacial reaction.

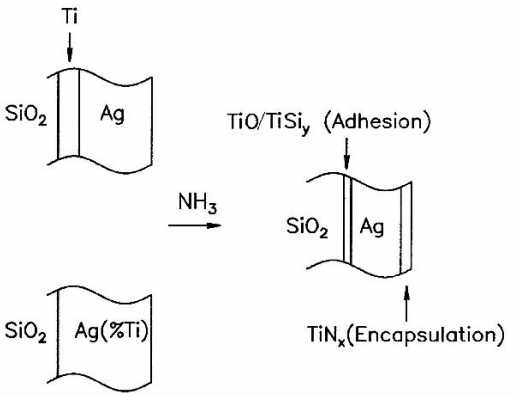

Figure 7.1. Schematic of nitride self-encapsulation of silver-bilayers and –alloys. The encapsulation process simultaneously provides a surface protection layer and an interfacial adhesion layer [17].

The RBS spectrum of an as-deposited Cu (20 at.% Ti) alloy is compared with that annealed at 500°C for 120 minutes (Figure 7.2). Upon annealing the Ti segregated to the free surface and the alloy/SiO_2 interface, with a slight preference to the surface. The Ti that diffused to the surface reacted with the ammonia and residual oxygen to form a titanium–nitride layer, indicated as TiN(O). The interfacial layers are labeled as "TiO_w" and "Ti_5Si_3", respectively. The spectrum of the annealed sample gives a residual Ti concentration of ~5.5 at.%.

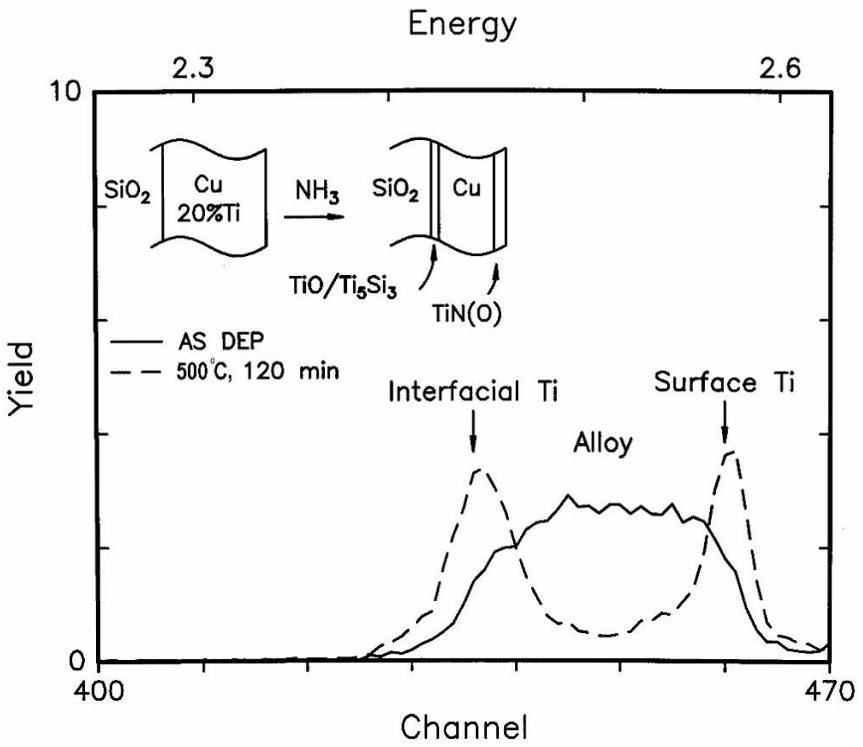

Figure 7.2. RBS spectra showing only the depth distributions of Ti for a Cu(20 at.% Ti) alloy before and after annealing for 120 minutes at 500°C in NH_3 ambient. The spectra were obtained using a 4.3 MeV He^{2+} beam and a scattering angle of 170° [17].

The encapsulation of the Ag-refractory bilayers proceeded in a similar way to that of the alloys. Alford *et al*. [4] demonstrated the encapsulation of the Ag-refractory bilayers using RBS (as show in Figure 7.3). Only the Ti and Ag backscattered signals are displayed, and the Ti signal shows clearly that the 500°C anneal causes Ti to segregate at the surface (see peak labeled "Ti surface"). Based on the RBS analysis, the TiN(O) surface layer is 10 nm thick. The interfacial bilayer is expected to consist of TiO_w (w~1:1) and Ti_5Si_3, the reaction products from the Ti–SiO_2 reaction [7].

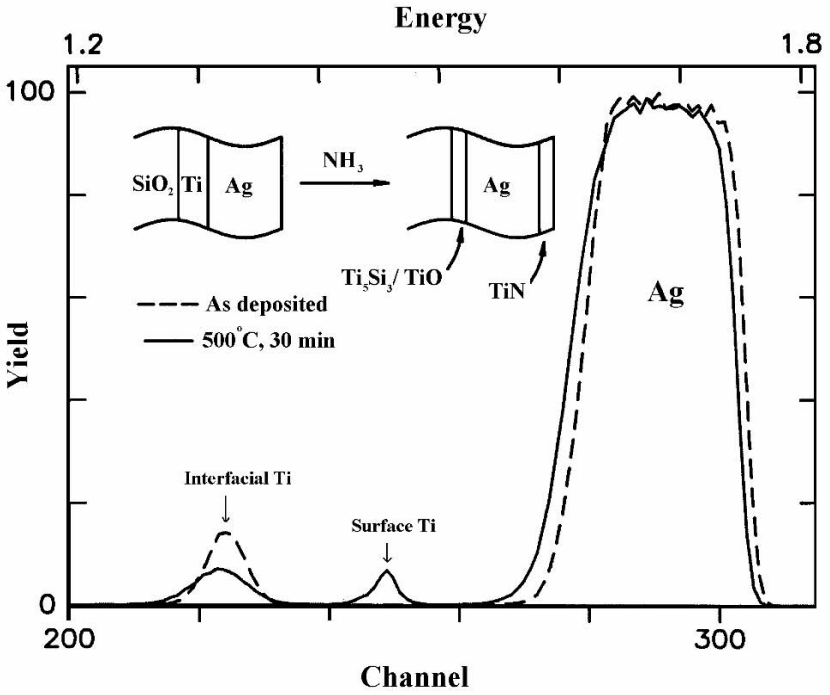

Figure 7.3. Ag encapsulation on SiO_2 prepared from Ag(120 nm)/Ti(22 nm) bilayers. RBS spectra show the depth distributions of Ag and Ti before and after annealing at 500°C in an ammonia ambient for 30 minutes. The spectra were obtained using a 2.0 MeV He^{+2} beam and a scattering angle of 170° [4].

Wang and Alford [8] evaluated the effectiveness of the $Al_xO_yN_z$ encapsulation layer as diffusion barrier. This was done by depositing a 50 nm thick Cu film on the $Al_xO_yN_z$/Ag structure followed by a high temperature anneal in both vacuum and forming gas. Figure 7.4 shows the RBS spectra of the Cu/$Al_xO_yN_z$/Ag structure before and after annealing at 620°C for 30 minutes [8]. Analysis of the data revealed that no interdiffusion occurred between the Cu and Ag. These results were the same for anneals in both vacuum and forming gas. Compared to the results obtained from the Ag/TiN system [9], the $Al_xO_yN_z$ diffusion barrier is stable up to 620°C, which is about 200°C higher than the TiN processed in a similar manner.

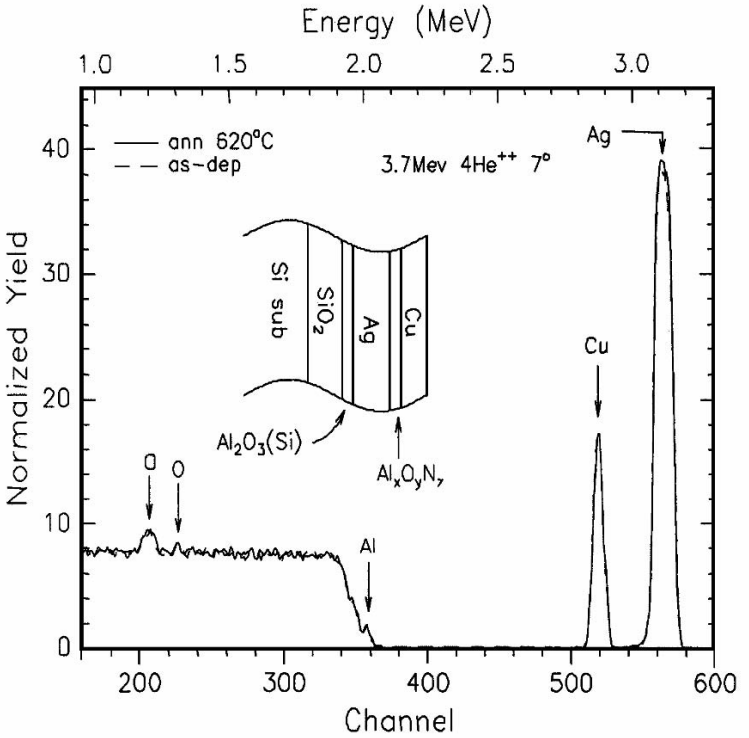

Figure 7.4. RBS spectra (3.7 MeV He^{+2}, 7° tilt) of the diffusion barriers before (broken line) and after (solid line) testing at 620°C for 30 minutes in flowing atmosphere N_2-5% H_2 ambient [8]

7.3 Electromigration Resistance

Electromigration (EM) resistance of Ag is the most critical interconnect reliability concern that would determine its suitability for integrated circuit technology. EM is the drift of metal ions as a result of either collision between the conductor electrons and/or the metal ions or high electrostatic field force when current is passed through a metal conductor. The direction of mass transport depends on the direction of the net force. When high current densities pass through the metal line, voids or hillocks are formed at a point of ion flux divergence (Figure 7.5). Voids and hillocks deform and grow until electrical failure is completed [10].

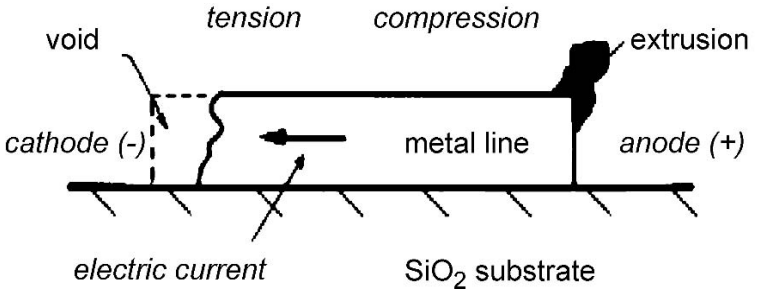

Figure 7.5. Schematic to illustrate metal conductor failure due to electromigration [17]

Ho and Huntington [11], Patil and Huntington [12] reported that Ag migrates toward the anode for the temperature range 670–877°C. Klotsman *et al*. [13] and Breitling and Hummel [14] however, found that Ag ion transport is toward the cathode, and is opposite to the direction of the electron wind. Studies conducted by Hummel *et al*. showed that the dominating movement path is grain boundaries for temperatures in the range of 225–280°C (activation energy of 0.95 eV) and surface for the temperature range 160–225°C (activation energy of 0.3 eV) [15].

In this study the influence of an encapsulation process on the electromigration resistance of Ag has been investigated. The sample configurations used consisted of bare Ag patterns and encapsulated Ag patterns. Compared to bare Ag lines, TiN(O) encapsulated Ag lines exhibited much better electromigration resistance in terms of the time required for the formation of significant number of voids and hillocks.

After the encapsulation process, the Ag surface is capped by a thin layer of TiN(O). The mobility of Ag atoms at the TiN(O)/Ag interface is substantially reduced. Therefore the electromigration resistance is improved significantly. By examination of the surface of the encapsulated Ag lines tested for a long time, almost no hillocks were observed. This implies that the surface diffusion has been hindered substantially by the presence of the TiN(O) encapsulation. Comparison of Tables 5.1 and 5.2 suggests that the encapsulation process improves the electromigration resistance of Ag metallization by at least one order of magnitude for the test structures and conditions used [16].

7.4 Future Trends

Ag metallization research has intensified significantly in recent years. Research work has been conducted mainly in the US. Increasing numbers of companies have already begun research and development (R&D) efforts in Ag-based metallization. However in this highly competitive era the industrial research has been propriety. Ag-based interconnects represents the future trend in the deep sub-micron regime.

Ag is an attractive material for interconnect-metallization in future integrated circuits technologies due to its low bulk resistivity and high reliability against

electromigration. Ag can be deposited by plating (electroless and electrolytic), sputtering (physical vapor deposition (PVD)), laser induced reflow and chemical vapor deposition (CVD) cluster tools, chemical mechanical polishing (CMP) polishers and low temperature etchers.

There are still many critical issues that remain to be resolved in the development of Ag-based metallization. For instance, to meet the throughput requirement in device manufacturing, there is a need to demonstrate a Ag deposition technique with a high deposition rate (>250 nm/min) at low substrate temperatures without simultaneously sacrificing low resistivity, good step coverage and complete via fill. The adequate use of thin diffusion barriers in Ag-based metallization will be critical for the 0.25 mm technology. Other materials science issues in Ag-based metallization need to be address: (1) microstructural control (*e.g.* grain size and texture); (2) contamination control (C, O and CI); (3) oxidation and corrosion control; (4) prevention of Ag diffusion in metals and dielectric materials; and (5) mechanical properties (*e.g.* stress migration, adhesion improvement). In addition, the development of Ag-based on-chip interconnects technology will also lead to new advancements in electronic packaging technology. The implementation of Ag-based interconnects will represent the future trend in the deep submicron regime.

7.5 References

[1] S. P. Murarka, R. J. Guttman, A. E. Kaloyeros, W. A. Lanford, Thin Solid Films 236, 257(1993).
[2] M. E. C. Willemsen, A. E. T. Kuiper, A. H. Reader, R. Hokke, J. C. Barbour, J. Vac. Sci. Technol. B 6, 53(1988).
[3] S. Q. Wang, I. Raaijmakers, B. J. Burrow, S. Suthar, K. B. Kim, J. Appl. Phys. 68, 176(1990).
[4] T. L. Alford, D. Adams, T. Laursen, B. M. Ullrich, Appl. Phys. Lett. 68, 3251(1996).
[5] Y. L. Zou, T. L. Alford, D. Adams, T. Laursen, K. N. Tu, R. Morton, S. S. Lau, MRS Proc. 427, 355(1996).
[6] J. Li, J. W. Mayer, E. G. Colgan, J. Appl. Phys. 70, 2820(1991).
[7] D. Adams, T. L. Alford, N. D. Theodore, S. W. Russell, R. L. Spreitzer, J. W. Mayer, Thin Solid Films 262, 199(1995).
[8] Y. Wang, T. L. Alford, Appl. Phys. Lett. 74(1), 32(1999).
[9] D. Adams, Ph.D. dissertation, Arizona State University, 1996.
[10] M. Mahadevan, R. M. Bradley, J. M. Bebierre, Europhys. Lett. 45, 80(1999).
[11] P. S. Ho, H. B. Huntington, J. Phys. Chem. Solids 307, 1319(1966).
[12] H. R. Patil, H. B. Huntington, J. Phys. Chem. Solids 31, 463(1970).
[13] S. M. Klotsman, A. N. Timofeyev, I. S. Trakhtenberg, Phys. Metal Metallogr. 14, 140(1962).
[14] H.M. Breitling, R. E. Hummel, J. Phys. Chem. Solids 33, 845(1972).

[15] R. E. Hummel, H. J. Geier, Thin Solid Films 25, 335(1975).
[16] Y. Zeng, L. H. Chen, Y. L. Zou, P. A. Nguyen, J. D. Hensen, T. L. Alford, Mater. Lett. 45, 157(2000).
[17] D. Adams, T. L. Alford, Materials Science and Engineering R 40, 207(2003).

Index